UNIVERSITY OF CAPE TOWN

DEPARTMENT OF HUMAN BIOLOGY:

BIOMEDICAL ENGINEERING

Development of a Tissue-Regenerative Vascular Graft: Structural and Mechanical Aspects

Mazin Salaheldin Sirry

submitted to the University of Cape Town in partial fulfilment of the requirements for rhe degree of

M.Sc (Med) in Biomedical Engineering

May 2010

Supervisor: Dr. Thomas Franz

Cardiovascular Research Unit, Chris Barnard Division of Cardiothoracic Surgery, Department of Surgery, University of Cape Town

Abstract

In attempt to prevent graft failure, the tissue-regeneration field offered the porous vascular scaffolds as promising solution for the lack of endothelialization seen in the small-calibre synthetic vascular graft. Another cause of graft failure was reported to be the mechanical mismatch between the graft and the host vessel. This study concerned the investigation and optimization of structural designs of tissue-regenerative vascular grafts, comprising ingrowth permissible porous polyurethane (PPU) foam and knitted reinforcement wire mesh, with the aim of providing vascular prostheses that mimic arterial mechanics.

A 3D geometry of a knitted eight-loop wire mesh was imported into Abaqus CAE® 6.8-2 and assembled with a PPU tube geometry such that the wire mesh acted as external reinforcement (EX) or embedded reinforcement (EM) to the PPU tube. A 45°-section assembly was meshed using 8-node linear brick elements. Nitinol (NITI) and polyurethane (PU) material models were used for the knitted mesh. Material parameters obtained in experimental tests were implemented in hyperfoam (PPU), shape memory alloy (NITI) and linear elastic (PU) constitutive models. The luminal grafts surfaces were subjected to uniformly distributed pressure load ramping from 0 to 200mmHg. Models were compared in terms of predicted maximum stress and strain, wall compression, strain energy, radial displacement and compliance.

The predicted radial compliance ranged between 1.2 and 15.6%/100mmHg in the reinforced grafts, compared to 106.4 and 65.1%/100mmHg for the non-reinforced grafts. The maximum stress in the Nitinol remained safe at 33 % of stress associated with start of austenite-martensite phase transformation (i.e. 483MPa). The maximum stress and strain values detected in the PPU tube indicated recoverable elastic deformation. The reinforcement enhanced the mechanical performance of the graft without affecting its tissue-regenerating characteristics, as the predicted maximum wall compression indicated that the reduction in size of pore windows would still allow ingrowth of capillaries and arterioles.

Declaration

I, Mazin Salaheldin Sirry, hereby declare that the work on which this dissertation is based is my original work, except where acknowledgements indicate otherwise, and that neither the whole work nor any part of it has been, is being, or is to be submitted for another degree in this or any other university.

Signature: ……

Date: ……

Acknowledgment

"No! *Worship Allah and be among the thankful*." (Surat az-Zumar; 66)

My sincere gratitude goes to "ALLAH", whom we worship, for his countless blessings.

I am heartily grateful to my supervisor, Dr. Thomas Franz, for his encouragement, and patience in guiding and helping me to understand and complete this work.

I own my gratitude to my dearest parents, Salaheldin Sirry and Entisar Elobaid, and my angel Sakna Osman, for their continuous prayers, support and love.

I would like to acknowledge Prof. Peter Zilla, the Director of the Cardiovascular Research Unit (CVRU), for giving me this great opportunity to join this internationally recognized research group. I would also like to acknowledge my colleagues in the CVRU, who assisted me and offered their light heartedness and friendship.

I would also like to thank my friends here in Cape Town for their kindness and companionship that made it easy to be far from home.

My sincere appreciation goes to the University of Medical Sciences and Technology, in Khartoum-Sudan, without whom all this would have not been possible. Thanks for the trust, encouragement and support.

This project was supported financially by the National Research Foundation (NRF) of South Africa

Table of Contents

List of Figures

List of Tables

1. Introduction

1.1.Background

Atherosclerosis and arteriosclerosis are two common arterial diseases. They refer to hardening, narrowing or loss of elasticity in major arteries. If not treated, they can lead to ischemia or infarction in the supplied organ. The treatment for these diseases usually requires intervention surgery either by using assistive devices to relieve and support the artery as in the balloon angioplasty and internal stenting, or by a complete replacement of the diseased artery using vascular grafts.

There are two main types of vascular grafts; the bioprosthetic grafts which are arteries or veins taken from the human body, and the synthetic grafts which are developed from synthetic materials. The problem of limited availability in the small-calibre bioprosthetic for patients requiring re-do procedures emphasized the synthetic grafts as a possible alternative. The weakness and over-compliance experienced by the different types of grafts was usually overcome by inclusion of reinforcing structures to enhance the mechanical properties of the grafts. The tissue regeneration field provided promising avenue in the development of medical implant, with particular reference to the cardiovascular and related fields, for processing and manufacturing methods capable of producing in-growth permitting structures. Initial attempts to replace arteries with solid tubes of synthetic material soon made it clear that porosity is a prerequisite for graft patency

Computational biomechanics is seen as a crucial part in the development of such synthetic structures for medical applications as this discipline can assist in the structural design optimization of multi-component vascular prostheses towards physiological properties and can also contribute to the theoretical understanding of the effect of biological processes such bio-degradation on mechanical properties of implants over time.

1.2.Problem Identification

The long-term success of tissue-engineered medical implants comprising synthetic materials depends largely on the host response. In synthetic implants, porosity is a key factor for mitigation

of foreign body response and inflammation. One key example for failure of synthetic implants is the poor clinical outcomes observed with small and medium-calibre synthetic grafts which are mainly attributed to ongoing thrombogenicity and anastomotic intimal hyperplasia (AIH). End-stage thrombotic occlusion of synthetic grafts is a result of an incomplete endothelial coverage, even after decades of implantation. This lack of endothelialisation is caused by the absence of transanastomotic endothelial outgrowth from the host artery into the prosthesis - a phenomenon observed in humans while pre-clinical animal models (except non-human primates) show full endothelialisation. AIH, the excessive thickening of intimal tissue in the peri-anastomotic region of vascular grafts, is caused by variations in flow and shear stresses, exacerbated by compliance mismatch, between the host artery and prosthetic implant, and often results in late graft failure.

1.3.Motivation

Therapies for cardiovascular diseases reach from purely artificial prostheses, such as mechanical heart valves and synthetic vascular grafts, to tissue engineering and regenerative medicine including stem cell approaches. The research into cardiovascular diseases, along with the improvement of prevention and treatment strategies, require increasingly multi-disciplinary approaches. While biomechanical engineering has been playing a role in some areas of cardiovascular research, such as vascular grafts, prosthetic heart valves, and cardiac assist devices, its importance is only in an emerging state in other fields amongst of which are myocardial infarction and restenosis. As yet, the ideal vascular graft has not been found. Approaches for optimisation of grafts mechanical and structural design is crucial to achieve mechanical matching with the host vessel. However, the in-vivo optimisation of graft prototypes is very expensive, or impossible to some extent. Biomechanics and biomedical engineering, comprising computational and applied mechanics, mechanical and materials engineering, have been a crucial element of such approaches along with other disciplines such as regenerative medicine, cell biology, biochemistry, chemistry and polymer sciences.

1.4.Objectives

This research forms part of a multidisciplinary research project at the Cardiovascular Research Unit on the development of tissue-regenerative small-diameter vascular grafts which provide desired in-vivo properties while minimizing the amount of foreign material introduced into the body and thereby reducing the negative host responses and

rejection of the implant. The graft comprises a knitted mesh, Figure 1-1(a), as support structure and a porous polyurethane scaffold (Bezuidenhout 2001; Bezuidenhout et al. 2002; Davies et al. 2008), as a blood-barrier material, which has interconnected pores between the external and internal surfaces allowing a transmural ingrowth of cells and tissues, Figure 1-1 (b).

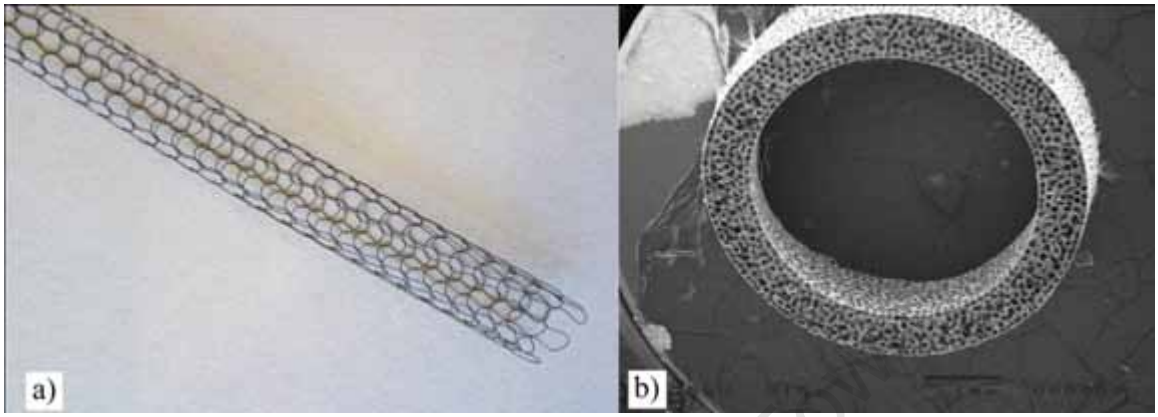

Figure 1-1: (a) Knitted wire mesh for vascular reinforcement, (b) Porous polyurethane scaffold with interconnected pores between the inner and outer surfaces

The "desired in-vivo properties" (i.e. when implanted) depend on the purpose of the implant. They may range from long-term structural integrity in the case of non-degradable scaffold materials to short-term structural integrity during initial implant phase combined with a controlled degradation process and substitution with host tissue when using biological degradable materials.

The objective of this project is the computational modelling of multi-component, small-diameter, non-degradable synthetic graft composed of porous polyurethane graft and reinforced with wire mesh structure to assist in technology and prototype development. The primary goal is to achieve the long term structural integrity of the graft by mimicking the arterial mechanics.

This project aims at:

- Selection of a suitable non-degradable material for the wire mesh structure.
- Prediction of structural properties and mechanical behaviour of the multi-component graft.
- Structural design optimization of the multi-component graft by means of computational modelling using the Finite Element Method (FEM).
- Assessment of wall compression effect on the pores size of the reinforced porous polyurethane scaffolds with respect to the ingrowth of cells and tissues.

2. Theory and Literature Review

2.1. Arteries

The circulatory system (Figure 2-1) in the human body is the system that transports the blood. It consists mechanically of a complex composite network of tubes (vascular system) that transmit the blood, and two sequential pumps (the heart) to force the blood through the tubes. The blood vessels consist of arteries, arterioles, capillaries, venules, and veins (Chung 2005; Ethier and Simmons 2007).

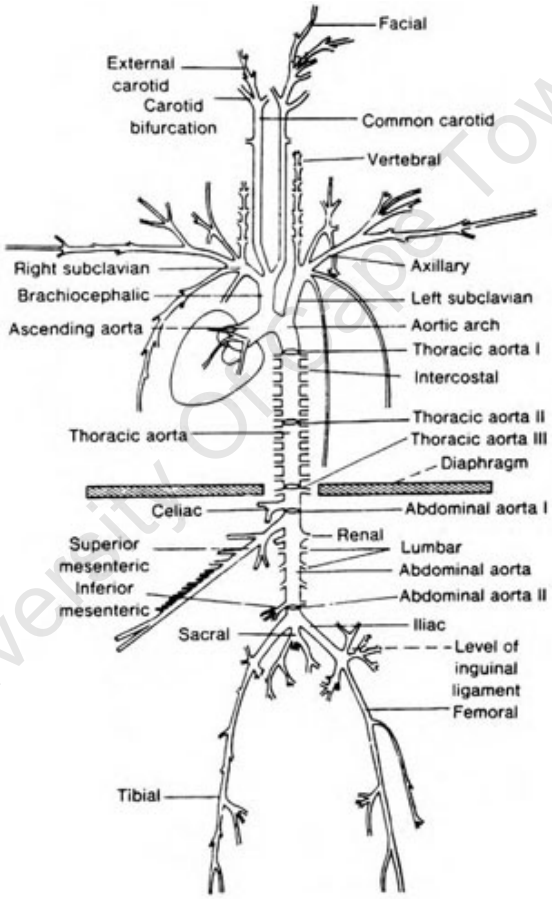

Figure 2-1:Circulatory system (Ethier and Simmons 2007).

The circulatory system is subdivided into two circulatory loops: the pulmonary circulation and the systemic circulation. In pulmonary circulation, the blood is transported from the right ventricle of the heart via the pulmonary arteries to the lungs for exchange of oxygen and carbon dioxide and returns back to the left atrium via the pulmonary veins. In systemic circulation, the blood is pumped through the aorta and

subsequent arterial network to all body parts and return back to the heart through the venae cavae (Chung 2005; Ethier and Simmons 2007).

The arteries are the blood vessels that carry the blood away from the heart and distribute it to all the tissues and organs of the body. Their thick and strong walls, relative to veins, allow them to withstand the pressure induced by the heart. The calibre of arteries decreases with increasing distance from the heart. The arteries are classified into three main categories based on the overall size and the wall thickness relative to lumen: large (elastic), medium (muscular) and small (arterioles) arteries (Moore and Agur 2007; Thiriet 2007).

2.1.1.Biology and Mechanics of Arteries

The general structure of blood vessels includes three layers, or tunicae (Figure 2-2). Tunica Intima is the inner most layer. It is mainly composed of endothelial cells which line the lumen and basal membrane of the sub-endothelial layer. The Tunica Media is separated from the Tunica Intima by the sub-endothelial layer which consists of loose connective tissues, elastic fibres and fibroblasts. The Tunica Media includes networks of smooth muscles collagen and elastin fibres arranged in helical fashion and separated from each other by Elastic Laminae (mainly elastic fibres). The Tunica media is the most important layer for determining the biomechanical properties of an artery (Ethier and Simmons 2007). The outermost layer is the Tunica Adventia which is predominantly composed of helical bundles of loose wavy collagen fibres (Holzapfel et al. 2000; Yeoman 2004).

The mechanical behaviour of arteries is governed by the mechanical properties of cells and tissues composing them and their relative proportion. Although some of the constituents do not have obvious influence on the arterial mechanical properties, such as endothelial cells, others play the major role in the overall arterial mechanical behaviour; namely the collagen, elastin and smooth muscle cells.

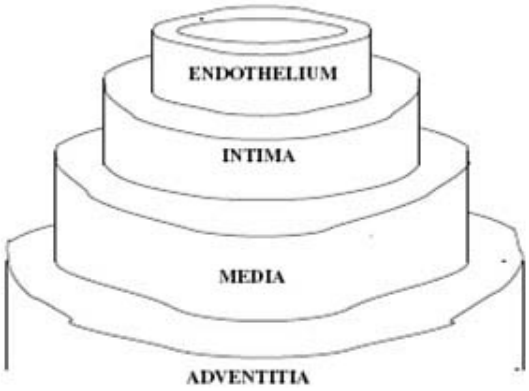

Figure 2-2: Vascular wall structure(modified from Thiriet (2007)).

The collagen is relatively stiff having a large elastic modulus (≈ 1 GPa) and limited extensibility (maximum strain of 2-4%) while the elastin has low elastic modulus (0.3-0.6 MPa) and large extensibility (130%) (Yeoman 2004). The smooth muscles cells help in prestressing the artery wall by introducing counteracting internal stresses. They are also responsible for the artery tone. As response to the strain, the proliferation of the smooth muscle cells increases. The composite elastin-collagen mechanical properties lead to the non-linear elastic behaviour of arteries (Figure 2-3). At lower pressures the extension of the artery is predominantly governed by the elasticity of elastin fibres. As the pressure increases, the elastic modulus and stiffness of the arteries increases due the recruitment of the high-stiffness wavy collagen fibres which will get tightened (Ethier and Simmons 2007; Thiriet 2007; Gundiah et al. 2009).

The large arteries have relatively large elasticity of their walls which allows them to expand and contract radially in response to change in blood pressure. The elastic fibres form the bulk of the Tunica Media in the large arteries with the smooth muscle fibres less abundant than in the muscular arteries (Eroschenko and Fiore 2008). This property allows them to behave as pressure buffers to maintain the blood pressure in the arterial system between the contractions of the heart. The aorta and its branches are examples of this type (Moore and Agur 2007).

The medium arteries are often known as the distributing arteries. Sometimes they are referred to as muscular arteries due to the smooth muscle cells that constitute most of their wall. These smooth muscle cells allow this type of arteries to contract (vasoconstrict) and decrease the lumen which helps in regulating the blood flow downstream. The femoral artery is an example of medium arteries (Moore and Agur 2007).

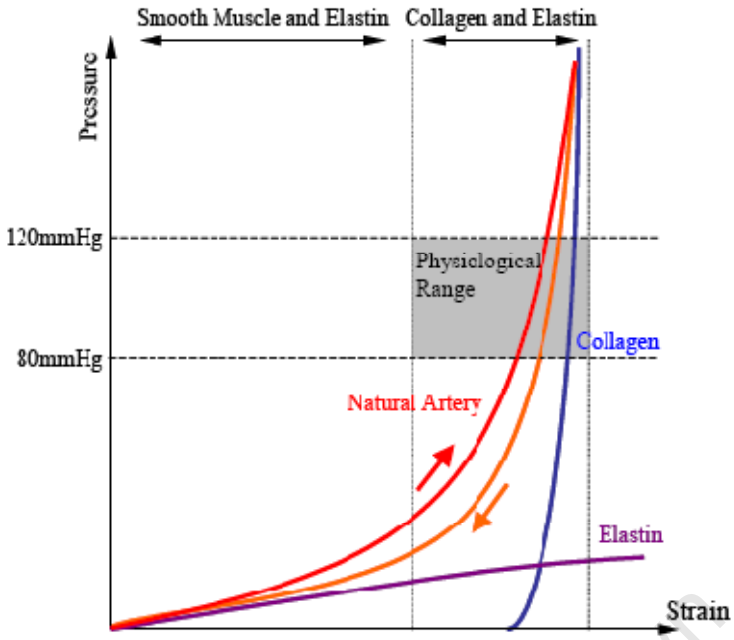

Figure 2-3: The non-linear elasticity of arteries and the influence of collagen-elastin composition (Yeoman 2004).

The arterioles have relatively narrow lumen and thick muscular wall. The degree of arterial pressure within the vascular system is mainly regulated by the degree of firmness (often known as tone) in the smooth muscle of the arteriolar walls. Hypertension (high blood pressure) results from the increase in arteriolar tone (Ham and Cormack 1979; Moore and Agur 2007).

The vascular compliance (Belz 1995; Tiwari et al. 2003) is a common parameter that used to describe the ability of the blood vessel to flexibly change its diameter in response to the applied pressure. It is defined by the equations:

$$C_D = \frac{D_2 - D_1}{(P_2 - P_1)D_1} \times 100 \times 100 \qquad (2.1)$$

$$C_V \approx 2\, C_D \qquad (2.2)$$

where C_D is the diametric (or radial) compliance, D_1 is the diameter of the vessel at luminal pressure P_1, and D_2 is the diameter of the vessel at luminal pressure P_2. The compliance is expressed in %/100mmHg. Sometimes it is described in terms of change in the volume of the vessels instead of change in the diameter. C_V represents the volumetric compliance in Eq. (2.2).

2.1.2.Arterial Diseases

Arteriosclerosis describes any hardening, and loss of elasticity, of medium or large arteries (Dorland 2000). Aging, degradation of the media and hypertension are the main causes of arteriosclerosis. Although it does not affect the conduit role of the arteries, the stiffening caused by arteriosclerosis has a direct impact on the pressure profile of the heart and arterial system (O'Rourke 1995; O'Rourke and Hashimoto 2006).

Atherosclerosis is the luminal narrowing of arteries due to injuries in the artery wall which will subsequently lead to arterial thrombosis. It is caused by the formation of plaques within the arteries (Maton 1997). Atherosclerosis causes ulceration and roughening of the endothelial lining of the artery, and the thrombi form on the roughened area. The generated thrombi can obstruct the artery. The obstruction in an artery causes infarction of the area being supplied by that artery. Myocardial infarction, brain stroke and ischemic gangrene of extremities are common clinical events of importance potentially caused by arterial occlusions (White 1989; Crowley 2009).

Arterial diseases can be treated by either pharmaceutical treatment, in which drugs are administered, or by interventional surgery. The intervention aspect of arterial treatment comprises balloon angioplasty, internal (endovascular) stenting and vascular grafting. Balloon angioplasty incorporates insertion of a guiding catheter into the narrowed artery and inflation of a balloon causing dilation of the artery. To avoid reoccurring of arterial narrowing, internal stents might be used to support the artery and maintain its patency for longer time. Literature showed that the endovascular stenting is a considerable means for treating the Abdominal Aortic Aneurysms (AAA), a blood-filled dilation of the abdominal aorta caused by disease or weakening of the vessel wall (Bos et al. 2008; Siegenthaler et al. 2008). Also it was found that endovascular stenting is essential after percutaneous transluminal coronary angioplasty for the treatment of coronary restenosis (Schmitz et al. 1996).

In vascular grafting, the diseased artery is used to be replaced, or bypassed, by autologous or heterologous native vascular grafts (bioprosthetics) or synthetic grafts. Long-term success of small and medium calibre bioprostheses is challenged due to the frequently encountered thrombosis, occlusion and aneurism (Fuchs et al. 1978; Dobrin et al. 1988; Crowley 2009). In addition, other factors such as age, disease or prior usage

limited the availability of bioprostheses grafts for patients requiring redo procedures (Min et al. 2009).

Synthetic vascular grafts are utilized as an alternative solution to bioprosthetic grafts. They are developed from materials such as polyethylene terephthalate (Dacron), polytetrafluoroethylene (Teflon) and polyurethane (PU), and are now frequently utilized for treatment of peripheral vascular disease (King et al. 1981; Klinkert et al. 2004; Kannan et al. 2005; Xu et al. 2010). Although these synthetic grafts have a great outcome in the replacement of large arteries, a very poor outcome is exhibited by the small and medium calibre grafts. The lack of endothelialization, due to the frequently induced anastomotic intimal hyperplasia (IH) and ongoing surface thrombogenicity, limits the long-term patency of the small diameter grafts (Zilla et al. 2007). Consequently, the lack of healing in synthetic vascular grafts has promoted a great deal of interest in tissue-engineering the ideal artificial arterial substitute.

2.2.Vascular Tissue Engineering

The tissue engineering concept involves application of engineering approaches in repairing or replacing damaged organs or tissues by introducing cells, scaffolds, growth factors or signal molecules to the damaged areas (Nerem and Sambanis 1995). The common strategy in tissue engineering is to separate the cells of interest from the patient, allow them to grow in an in-vitro three-dimensional scaffold with controlled environmental conditions, introduce the new structure into the body, and allow tissue formation to substitute the biodegrading scaffold (Vacanti and Langer 1999).

The earliest application of tissue engineering in the vascular grafting area examined the feasibility of providing cultured endothelial cells lining for grafts made of polypropylene and polyester (Mansfield et al. 1975). The subsequent attempts soon made it clear that porosity is a prerequisite for the patency of the graft and ranked it above the properties of the graft material (Voorhees et al. 1952; Wesolowski 1978; Haimovici 1984).

It has been suggested that in-vivo approaches of tissue regeneration are more promising than the ex-vivo construction of organs (Campbell and Campbell 2007). Much of the current research in polymer grafts utilises biological coatings to reduce this thrombogenetic reaction of the grafts' luminal wall. Inducing endothelium growth on the luminal surface was the major goal to allow for cellular ingrowth through the graft wall,

leading to musculogenesis (re-growth of muscular cells), angiogenesis (arterioles development) and the eventual endothelialisation (Sauvage et al. 1974; Hess et al. 1983; Hayashi et al. 1989; How et al. 1992). One method of encouraging this was by utilising a porous graft structure, which had defined channels and micro-pores to the luminal surface. The complete healing of the vascular graft implies a transmural tissue ingrowth rather than the initially applied transanastomotic ingrowth (Lyman et al. 1978; Hayashi et al. 1989; Mooney et al. 1996; Zilla and Greisler 1999). In addition to tissue ingrowth permeability, the size of pores was found to have a significant impact on the inflammatory response of the graft (Bezuidenhout et al. 2002). However, the reduction of pores size was a crucial issue (Yeoman 2004; Yeoman et al. 2009) when considering the compression exerted on the wall of the pressurized graft. Therefore, at the maximum blood pressure the porous grafts should secure a minimum pores diameter required for tissue ingrowth.

Although the failure of grafts is not fully understood, it is generally agreed that compliance mismatch between artery and graft plays a major role in failure (Sauvage et al. 1974; Lyman et al. 1978; How et al. 1992). The physical discontinuity between the artery and graft alters the blood flow, contributing to thrombosis and eventual failure. Therefore much emphasis has been placed on the mechanics of natural arteries in the hope of finding a patent graft which would mimic the properties of the host vessel (Baird et al. 1977; Ballyk et al. 1998). One way to achieve physical continuity of the blood conduit is through compliance matching between the graft and the host vessel. This helps blood flow, reduces thrombotic build up, allows for a steady transfer of the pressure pulse and reduces the elastic stress-strain difference between the graft and artery (Lyman et al. 1978; Uchida et al. 1993). The adjustment of the graft compliance sometimes is achieved by means of mechanical reinforcement of the graft, which might be necessary for compliance matching (Tanabe et al. 1980; Nagahama et al. 2005; Yeoman et al. 2009).

The concept of reinforcement of vascular grafts began with the bioprosthetic grafts. External supportive structures were commonly used to adjust the over-compliant vein grafts (Tanabe et al. 1980; Moritz et al. 1990; Moritz et al. 1992; Nagahama et al. 2005). With the researches heading towards the synthetic grafts, including the tissue engineered grafts, reinforcement also became an issue to enhance the mechanical properties of the over-compliant grafts (Magee et al. 1992; Xu et al. 2010). Optimisation of structural designs provides a great deal in controlling the overall mechanics of the synthetic grafts (Chandran et al. 1992; Byrne et al. 2007; El Zahab et al. 2009; Yeoman et al. 2009).

2.3.Mechanics of Materials

This study includes two types of materials, a Shape Memory Alloy (SMA) and a polymer. A brief description of the mechanics of the Ni-Ti alloy, commonly known as Nitinol, and polyurethane materials will be presented in this section.

2.3.1.Nitinol Material

In the medical field, the Nitinol is the most commonly used among the other SMAs due to its high biocompatibility, light weight, strength and non-magnetic nature (Ryhanen 1999; Gong and Pelton 2002; Gall et al. 2005). The SMAs differ from the other metal alloys in the fact that they can exist in two solid phases; the austenite and martensite phases. The two different solid phases have different crystal structures depending on the temperature and the state of stress. The austenite phase has a “body-centred cubic” crystal structure, while the martensite phase has a “monoclinic” crystal structure. The Nitinol is a member of the SMA family which includes other metal alloys such as Ag-Cd, Au-Cd, Cu-Zn-Al, Cu-Al-Ni, Ni-Al, Fe-Pt and Mn-Cu (Shaw and Kyriakides 1995; Brinson et al. 2004; Meissner 2004). The two unique responses that characterise the SMAs are the shape memory effect and superelasticity.

The shape memory effect is a temperature dependant response. At low temperatures the SMA exists in the martensite phase, and as the temperature raises it undergoes a phase transformation from the martensite to the austenite phase. When the Nitinol is cooled below the martensite start temperature (Ms) (see Figure 2-4(a)) to the martensite phase and inelastically deformed to a certain shape, its crystals undergo a reorientation. When martensite is reverted to austenite by heating it above the austenite start temperature (As), the original austenitic shape is restored, regardless of whether the martensite phase was deformed. Thus the name "shape memory" refers to the fact that the shape of the high temperature austenite phase is "remembered," even though the alloy is severely deformed at a lower temperature. The difference between the characteristic transition temperatures for heating and cooling is called the hysteresis. For the Nitinol this is usually around 20-50^{o}C (Auricchio and Taylor 1997; Auricchio et al. 1997; Ryhanen 1999).

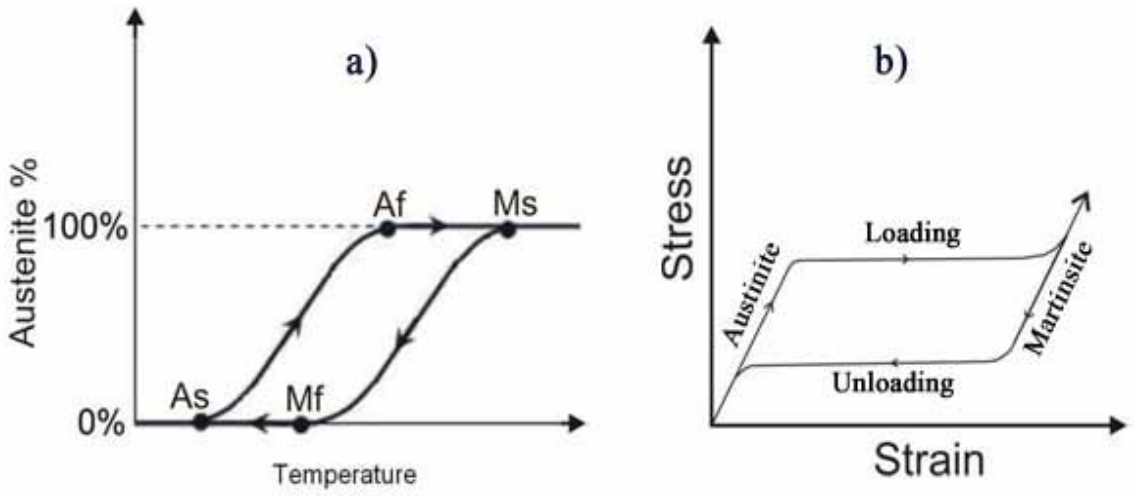

Figure 2-4: (a) the percentage of austenite phase depending on the temperature change in the Nitinol. (b) the superelastic stress-strain relationship of the Nitinol(modified from van der Merwe (2007)).

The superelasticity implies that the transformation between solid phases of the SMA is induced by the stress. The superelasticity property involves using the Nitinol during the high temperature (austenitic) phase, particularly above Af. The martensite phase is generated by stressing the metal in the austenitic state and this martensite phase is capable of large strains. The superelastic stress-strain relationship is illustrates in Figure 2-4(b). With the removal of the load, the martensite transforms back into the austenite phase and resumes its original shape (Ryhanen 1999).

2.3.2.Polyurethane Material

The enthusiasm with which the polyurethane was initially adopted as vascular graft materials was based on two main advantages over polyester and Teflon: elasticity and ease of handling (Zilla et al. 2007). Polyurethane is a type of polymers widely used in the implantable devices. It is classified as thermoplastic elastomers combining the properties of thermoplastics and elastomers. Mechanically, the polyurethane, as many polymeric materials, can be described as an isotropic elastic material which exhibits viscoelastic (creep) behaviour. When a polymer is cooled, it changes from a viscous rubber-like material to a hard brittle material upon passing through a certain temperature, known as the glass transition temperature (T_g). The elastic and viscoelastic behaviour varies depending on the glass transition temperature, the operation temperature, the load rate and time scale. Figure 2-5 illustrates the stress-strain curves of polyurethane samples tested at various temperatures. A given curve is concave to the strain axis until fracture without showing evidence of yielding. The increase in the operation temperature leads to

decrease in stress at a given strain level and exhibiting a nonlinear elasticity. The range of operation temperatures shown in Figure 2-5 is bellow the glass transition temperature of the polyurethane ($T_g \approx 130^oC$), however, the behaviour above this temperature is expected to be highly nonlinear (Cheremisinoff 1991; Yeoman 2004).

The viscoelastic behaviour of polymers is a function of the chemical composition and the difference between the glass transition temperature and the test or operation temperature. At a given temperature, a polymer with a low T_g exhibits a faster viscoelastic response than a polymer of a higher T_g (Lamba et al. 1998). Figure 2-6 illustrates the relationship between the viscoelastic behaviour and the operation temperature. Varying the operation temperature extremely change the viscoelastic property of a polymer.

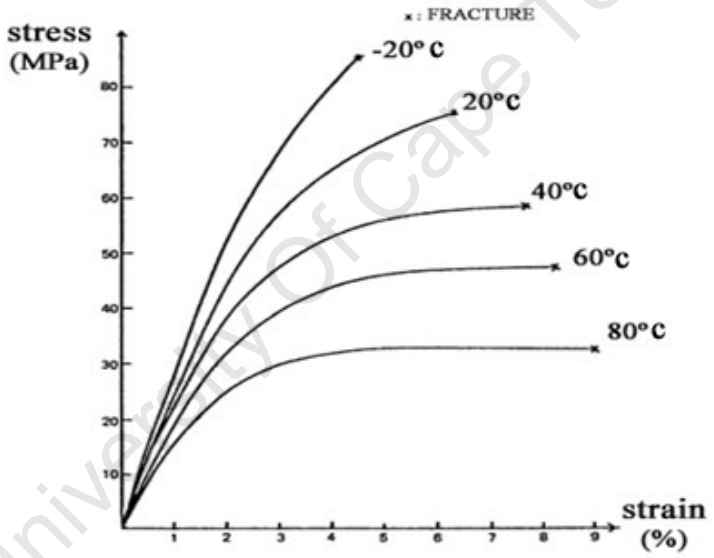

Figure 2-5: Stress-strain curves of a particular polyurethane at different operation temperatures (modified from Cheremisinoff (1991)).

In case of dynamic loading, the final state of the polymer is highly dependent on the rate by which the load is applied. At low temperatures and high load rates a polymer may display glass-like characteristics (low breaking strains and high elastic modulus), and at higher temperatures and low load rates it displays rubber-like qualities (large strains and low elastic modulus), while at normal, i.e. room, temperature it acts like a viscous fluid (Nielsen and Landel 1994).

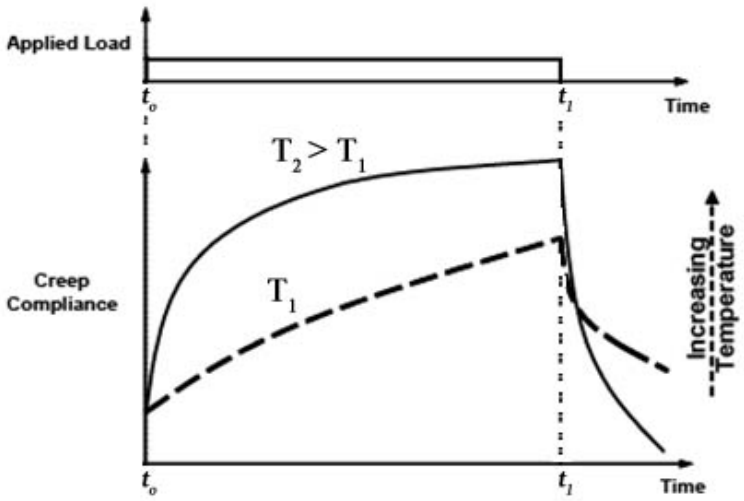

Figure 2-6: Viscoelastic (creep) behaviour of a polymer at different operation temperatures (modified from MacKellar (1998)).

2.4.Numerical Modelling

The pure analytical approaches have encountered difficulties in describing the mechanics of structures with complex designs and materials. The computer aided approaches provided a great advantage in this issue by providing numerical solution techniques.

The numerical modelling involves a mathematical representation of a process, device, or concept by means of a number of variables which are defined to represent the inputs, outputs, and internal states of the device or process, and a set of equations and inequalities describing the interaction of these variables. The finite element method (FEM) is one of the most common numerical solution techniques (Wayne 2004).

In the following sections, some of the theoretical concepts of the FEM will be highlighted. These were summarized from Usyk and McCulloch (2003), Yeoman (2004), Wayne (2004), and Prendergast and McHugh (2004). After that, a review of literature on the numerical modelling of the vascular grafts will be presented.

2.4.1.Finite Element Method

Problems in solid mechanics generally take the form of systems of partial differential equations defined in terms of the spatial coordinates and time. The FEM is useful for solving such partial differential equations in cases involving complex geometry, boundary conditions, nonlinear material behaviour, and contact. The solution approach is

based either on eliminating the differential equation completely (steady state problems), or rendering the partial differential equations into an approximating system of ordinary differential equations, which are then numerically integrated using standard techniques such as Euler's method.

2.4.1.1.Discretization and Approximation

The key feature of the FEM is the discretization of continuum problems (Figure 2-7). The discretization involves the generation of the finite element (FE) mesh. It is the process of partitioning the domain into a finite number of smaller regions of simple shapes, known as finite elements. The designated points in the elements are called nodes.

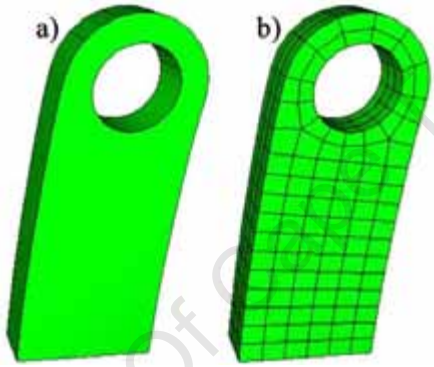

Figure 2-7: Discretization of a solid structure (a) into elements and nodes (b).

The second feature of FEM is that the governing equations are represented in integral form rather than differential form. Since the integral over the whole domain is the sum of integrals over each subdomain (element), the FEM provides a mechanism not only for solving the numerical problem but for assembling it. In the general case, an unknown function **u** satisfies a certain set of partial differential equations:

$$A\,(u) = \begin{Bmatrix} A_1\,(u) \\ A_2\,(u) \\ . \\ . \\ . \end{Bmatrix} = 0 \qquad (2.3)$$

over a domain Ω, subject to appropriate boundary conditions:

$$B\,(u) = \begin{Bmatrix} B_1\,(u) \\ B_2\,(u) \\ . \\ . \\ . \end{Bmatrix} = 0 \qquad (2.4)$$

on the boundaries Γ. The FEM seeks the approximate solution û in the form:

$$u \simeq \hat{u} = \sum_{1}^{r} \Psi_i a_i \tag{2.5}$$

where Ψ_i are basis functions prescribed in terms of independent variables(such as spatial coordinates x,y,z), and some or all of the parameters a_i are unknown.

To approximate a set of points $\{x_k; u_k(x_k)\}$ by a continuous function, a convenient and popular method is to use a polynomial expression such as: $u\,(x) = a + bx + cx^2 + dx^3$ ... and then to estimate the monomial coefficients a, b, c, d ... to obtain a best approximation to the field variable $u\,(x)$. The FE solution is approximated inside the elements by interpolation functions or shape functions which are normally polynomial in form. Figure 2-8 illustrates the way a piecewise linear interpolation over three elements can approximate the exact continuous solution. Usually continuity of the field variables is enforced across neighbouring elements. Interpolation or shape functions are used to represent the field variables such as displacement and stress. The order of the interpolation functions is linked to the number of nodes in the element. Accuracy of the solution normally increases with an increase in the order of the interpolation function.

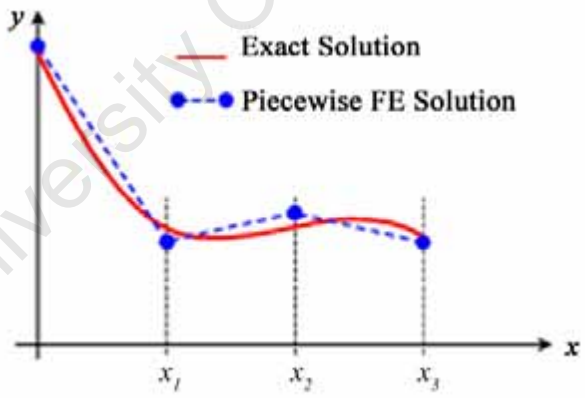

Figure 2-8: The FE piecewise approximation of the exact solution (Yeoman 2004).

The Lagrangian and Eulerian meshes are the most common types of the FE discretization. The Lagrangian meshes, where the elements and nodes move with the material, are classified as updated and total Lagrangian formulations. Eulerian meshes on the other hand do not deform with the material; thus, Eulerian elements retain their shape.

2.4.1.2.Finite Elements

The discretization process eventually ends up with a patchwork of finite elements that interconnected to form the geometry. There is a variety of elements that differ in the shape and the number of nodes, two of which are illustrated as examples in Figure 2-9. Selection of the element type and the total number of elements is subject to the nature and complexity of the geometry. If the space is one-dimensional, the elements may be bar elements to form trusses or beam elements to form frames, for example. If the space is two-dimensional, triangles or quadrilateral elements are most commonly used to discretize the space. If the space is three-dimensional, tetrahedral and hexahedral elements, respectively, may be implemented. Numerous types of elements (shell elements, plate elements, planar elements, 3D solid elements, etc) often exist within various FEM software packages to lend versatility. It is also conceivable to discretize a geometry by combining two or more element types in one, two, or three dimensions.

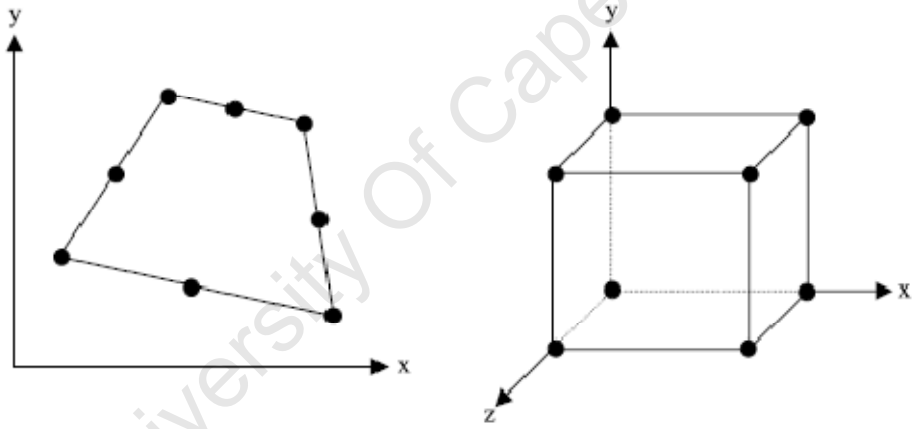

Figure 2-9: Two types of elements: 2D (quadrilateral) and 3D (brick) finite elements, with the black circles denoting nodes (modified from Wayne (2004)).

The number of elements in the mesh and their size are dependent on the degree of spatial variation of the field variable that is expected for the given problem. If large variations are expected in some regions of the geometry, smaller and more elements would be used in those regions to better approximate the field variable. A mesh can also be refined (more and smaller elements) after an analysis if the results are not deemed accurate enough. As the number of elements (and thus nodes) in a given mesh increases, the FE analysis results typically converge to the true solution of the problem. An infinite number of elements is not computationally efficient or feasible, however, and thus mesh refinement is completed until the level of convergence and accuracy is acceptable.

Choosing the optimal mesh density for a FE model is a critical issue. The accuracy of the numerical solutions is greatly dependant on the density of the FE mesh. A mesh convergence study is performed on a FE model by generating different mesh densities and evaluating the convergence of the predicted numerical solution. The approach for the test requires at least three levels of mesh densities in order to obtain a curve similar to the one shown in Figure 2-10, in which measures of mesh density is plotted against predicted values of a certain output variable. As the mesh density is increased, the predicted output values converge. This test is run until two subsequent mesh densities yield output values of a negligible difference, with the optimum mesh density being the lower one. Increasing the mesh density also increases the computational expense. Therefore, the mesh convergence assessment is a compromise between the numerical accuracy and computational expense.

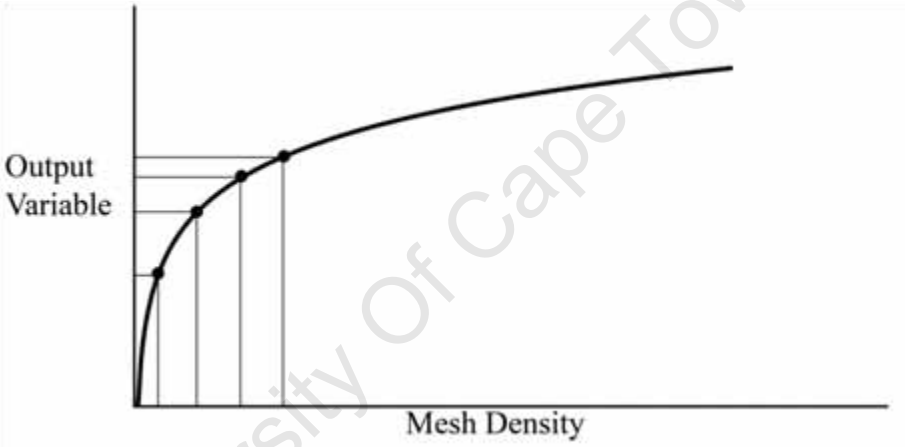

Figure 2-10: Mesh convergence study: output measures converge as the mesh density increase.

2.4.2.Finite Element Modelling of Vascular Grafts

The computational modelling of vascular graft in literature, including the bioprosthetics and synthetic grafts, can be separated into three distinct categories: finite element method (FEM), computational fluid dynamics (CFD), and fluid structure interaction (FSI). FEM is utilized to examine and evaluate the structural mechanics of the grafts. CFD employs the finite volume method (FVM) to investigate the patterns of blood flow (hemodynamics) in the grafts and its mechanical effects on the graft wall (Taylor et al. 1998; Taylor et al. 1998; Berthier et al. 2002; Dollie 2007). The FSI combines FEM and CFD and is used to investigate the mutual mechanical effects between the graft and the blood (Papaharilaou et al. 2007; Pitman 2007; Kim et al. 2008; Sun et al. 2009).

Other structures were found to be modelled with FEM include native blood vessels, balloon catheter and endovascular stents. Blood vessels were modelled either to examine their mechanical response to loads (Holzapfel et al. 1996), or to examine the stent behaviour considering the vessel mechanics (David Chua et al. 2004; Walke et al. 2005). Balloon catheter models were employed to simulate the endovascular stent-balloon system in balloon angioplasty (Holzapfel et al. 1996; Wang et al. 2006). Additionally, these structures along with blood flow were modelled with CFD and FSI to investigate the shear stresses exerted on the vessel wall by blood, and the blood-vessel and the vessel-stent interactions (Oshima et al. 2001; Gay et al. 2006; Valencia and Solis 2006).

Numerical modelling of vascular grafts usually includes several steps; a determination of the structure geometry, preparation of a model for the desired material, determination of the element type and mesh density, simulation of loadings and surrounding environment, and finally monitoring and analysis of the structure response. The covered literature showed that main differences between different studies were based on the details of these steps. Since FEM is the intended numerical modelling tool of this study, it will be only considered in the following review whereas CFD and FSI will not be reviewed in detail.

Whitcher (1997) utilized a single cell geometry along with the symmetry to design the geometrical shape of a Nitinol stent in a study aimed at simulation of its in-vivo behaviour. The Material model was validated by comparison with tensile elongation and fatigue tests.

However, van der Merwe et al. (2008) utilized single loop geometry as a Nitinol mesh structural unit to model two different (i.e. even and uneven) mesh geometries with different wire thicknesses in an attempt to evaluate the effect of design variation in the mechanical behaviour of knitted Nitinol mesh. The models were validated by comparison their predicted compliance to experimental compliance values, and verified using parameter variations such as element type, mesh density, and contact and boundary conditions. Characterization of the Nitinol material was implemented by cyclic uniaxial tensile tests performed on 12 samples of Nitinol wires .The Nitinol material model was validated using single-cycle uniaxial tensile models. The stress-strain curves obtained from the uniaxial tensile models were compared to those obtained from the characterization tests. The model of 0.05mm wire thickness predicted compliance value of 2.5%/100mmHg. Other experiments were performed at the Cardiovascular Research Unit (CVRU), Dynatek Delta and Medtronic MBC (Franz 2009) to obtain experimental

compliance data from prototypes of NITI wire mesh. The obtained experimental compliance values were very close to each other with minimum and maximum values of 4.15 to 5.12%/100mmHg, respectively. These experimental compliance values were greater than the numerical compliance values obtained by van der Merwe et al. (2008) in spite of the consistency of inner diameter and wire thickness of the prototypes and the FE model.

Etave et al. (2001) created two models of tubular (Palmaz-Schatz®) and coil (Freedom®) stents to investigate some properties including the stent deployment pressure, the intrinsic elastic recoil of the applied material, the stent resistance to compressive force, the stress maps, the flexibility, and the foreshortening. The material model in this study incorporated the 316L stainless steel. Another stent model was carried out by Welch et al. (2008) in an investigation of polymeric stents (poly l-lactic acid). The regional and cross-sectional differences in fibre deformation and stress development along the stent fibre axis were examined at incremental pressure loads. Elastic-plastic yielding uniaxial tensile test was applied to gather the mechanical information, however, von Mises criterion was applied for the material model.

Zidi and Cheref (2003) performed FE simulation to compare the compliance of different fibre reinforcement silicone grafts and predict the degree of the compliance mismatch in an anastomosis. They proposed the silicon structures for the design of small diameter vascular graft due to their closer compliance to the natural arteries compared to other vascular prosthesis. In another study done by Kleinstreuer et al. (2008), FE models of Nitinol diamond-shaped stents were investigated barely and in combinations with Teflon and Dacron grafts for the treatment of the AAA. The effects of crimping, deployment, and cyclic pressure loading on stent-graft fatigue life, radial force and wall compliances were simulated and analysed.

Ballyk et al. (1997) performed a large strain FE analysis of vascular wall mechanics to compare the influence of compliance mismatch on intramural stresses in end-to-end versus end-to-side anastomoses. Similar study utilized 2D axisymmetric models to investigate the effects of the suturing and material difference on the compliance mismatch of two different vessels, however, it incorporated simulation of blood flow and FSI.

Computational modelling has become a very effective tool in the design and development of tissue engineering scaffolds (Butler et al. 2000; Sun and Lal 2002; Stylianopoulos et al. 2008). Kirk et al. (2002) utilized the FVM to model and simulate the bioreactor and tissue culture performance. Jaecques et al. (2004) employed a FE modelling on the microscopic level to investigate the mechanical behaviour of bone scaffolds. Yeoman et al. (2009) built FE models of porous polyurethane grafts of different porosity. Genetic algorithms were utilized in designing of an elastic knit fabric which was used as external reinforcement structure in an attempt to compensate for the low mechanical strength of the polyurethane graft. Eight-node brick elements without twist were chosen to model the polymeric layer and 4-node linear membrane elements without twist were used to model the external layer of fabric reinforcing. The polyurethane material model was validated by comparing the stress-strain curves obtained from a set of validation models to the physical data of previously conducted tensile, compression and shear tests.

In conclusion, different computational tools have been utilised in the investigation of vascular grafts. From the presented review, FEM is considered feasible for the structural and mechanical optimization of the under-examination vascular graft. In addition, the FEM is assumed to sufficiently serve the objectives of this study and highlight the paths for further investigations. However, FEM is not capable of providing information on the blood flow characteristics and might have some limitations in simulating realistic in-vivo conditions.

2.4.3.Constitutive Models

2.4.3.1.Porous Polymer

Mathematically the material behaviour of polymers is commonly referred to as hyperelastic behaviour. Hyperelastic materials describe generally incompressible materials, while hyperfoam models describe compressible polymers. Substantial work has been done in the development of constitutive relations for rubber-like elastic polymers. Various relations have been proposed in the form of strain energy potential (U) and formulated in terms of strain invariants, I_1, I_2 and I_3. Treloar (1958) proposed the Neo-Hookean model, the simplest relation amongst the others, which was defined in terms of a single parameter. Mooney (1940) and Rivlin (1949) provided strain energy functions in terms of two parameters and showed that results compared well with

experimental data for uniaxial deformation modes. Ogden (1984) proposed the strain energy function:

$$U = \psi(\bar{\lambda}_1, \bar{\lambda}_2, \bar{\lambda}_3) = \sum_{i=1}^{N} \frac{2\mu_i}{\alpha_i^2}\left(\bar{\lambda}_1^{\alpha_i} + \bar{\lambda}_2^{\alpha_i} + \bar{\lambda}_3^{\alpha_i} - 3\right) + \sum_{i=1}^{N} \frac{1}{D_i}(J_{el} - 1)^{2i} \qquad (2.6)$$

where J_{el} is the elastic volume strain energy and D_i, μ_i and α_i are temperature dependant material parameters. This function is defined in terms of principal stretch λ_i ratios rather than strain invariants I_i, and a number of coefficients dependent on the order of the function. In special cases this function can be reduced to form the Neo-Hookean and Mooney-Rivlin models.

2.4.3.2.Nitinol

A Nitinol stent model was created by Gong and Pelton (2002). They demonstrated the analysis difficulties associated with the highly non-linear behaviour of the Nitinol material which implied the implementation of efficient constitutive model since numerical iteration would be necessary during the analysis. A single diamond shaped unit cell of the stent was modelled to represent the stent design. They utilized a user-material to describe the define the Nitinol material behaviour in Abaqus, a commercial FEM software, based on a general plasticity description (Auricchio and Taylor 1997; Auricchio et al. 1997). A good agreement was observed when they compared the load and displacement results to the experimental data. Stent stiffness was also accurately predicted. The FEM modelling of Nitinol stents with the developed Abaqus Nitinol user-material proved appropriateness in fatigue analysis and optimization of the functionality of the device (Rebelo et al. 2001).

3. Materials & Methods

3.1. Finite Element Models

Models of small-diameter vascular grafts were developed by utilizing a 3D model of tubular knitted wire mesh as mechanical reinforcement for a porous polyurethane (PPU) tube. Two graft assemblies comprising different reinforcement systems were created, as illustrated in Figure 3-1; external reinforced graft (EX) and embedded reinforced graft (EM). Nitinol (NITI) and solid polyurethane (PU) materials were assigned separately to the wire mesh in the EX and EM assemblies. Different graft models underwent finite element (FE) analysis to assess their behaviour when subjected to luminal load covering the physiological range of blood pressure.

This section highlights the steps undertaken in creating the different FE models, implementing the FE analysis and verifying the numerical outcomes obtained from those models.

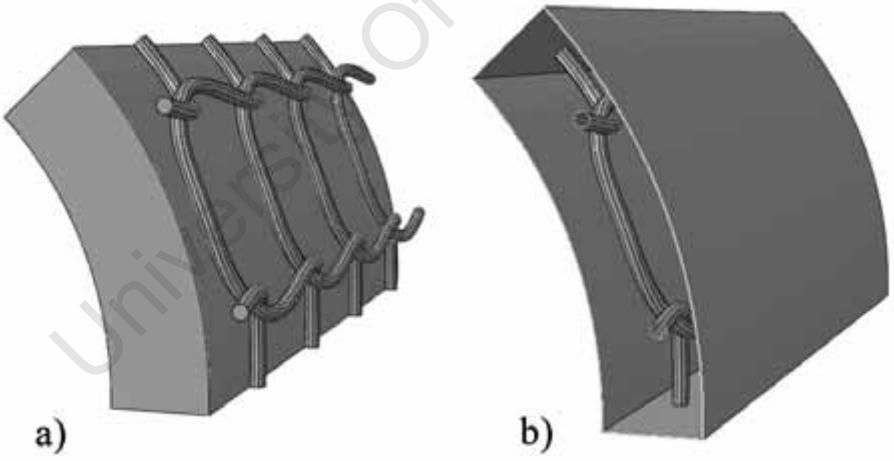

Figure 3-1: One-eighth models of vascular grafts: a) EX assembly, (b) EM assembly.

3.1.1. Geometry

3.1.1.1. Wire Mesh Geometry

The geometry of the wire mesh was defined in previous studies (van der Merwe 2007; van der Merwe et al. 2008). A solid single loop part, Figure 3-2(b), of a 3.0mm inner

diameter and 0.05mm thickness was created from a three dimensional eight-loops knitted tubular centreline geometry (provided by Pro-Consulting, Minneapolis, MN, USA), Figure 3-2(a), using Pro-Engineering Wildfire 2.0 (Parametric Technology Corporation, Needham, MA, USA). The solid single loop geometry , which formed 45° sector, was imported into Abaqus CAE 6.8-2 (Dassault Systemes, Providence, RI, USA) and used to create assembly of loops arranged longitudinally in a similar knitted pattern of the tubular centreline geometry, Figure 3-2(c). The tubular centreline geometry was not symmetrical due to the helical trend of the knitted loops. However, due to the repetitive pattern of the structure, one eighth (i.e. 45º) model of the structure was assumed sufficient to simulate its behaviour with the aid of boundary conditions (BC).

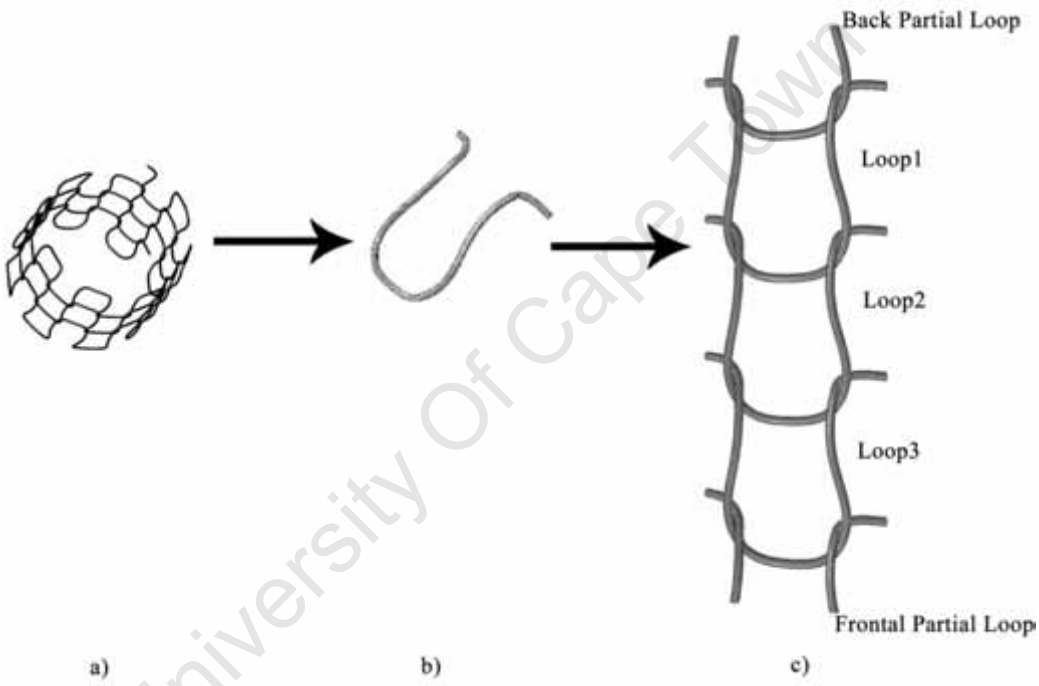

Figure 3-2: Wire mesh geometry: a) eight-loop knitted tubular structure, b) the separated single loop part, c) the generated knitted pattern assembly.

Utilizing the concurrent arrangement of the wire loops in the main tubular structure along its length, two partial loops (two halves of the single loop) were attached to the assembly; one half to each end. These partial loops were used to define boundary conditions and restrain the movement of the other three loops in attempt to simplify the longitudinal geometry.

3.1.1.2.PPU Tube Geometry

The geometry of the PPU tube was developed in Abaqus CAE 6.8-2 by extrusion of a 45° sector of 0.3mm thick cylinder, as shown in Figure 3-3. Two versions of PPU tube were generated by adjusting the inner diameters to 2.4 and 2.84mm, respectively. These two inner diameters were essential for the different graft assemblies, as will be described in Section 3.1.1.3.

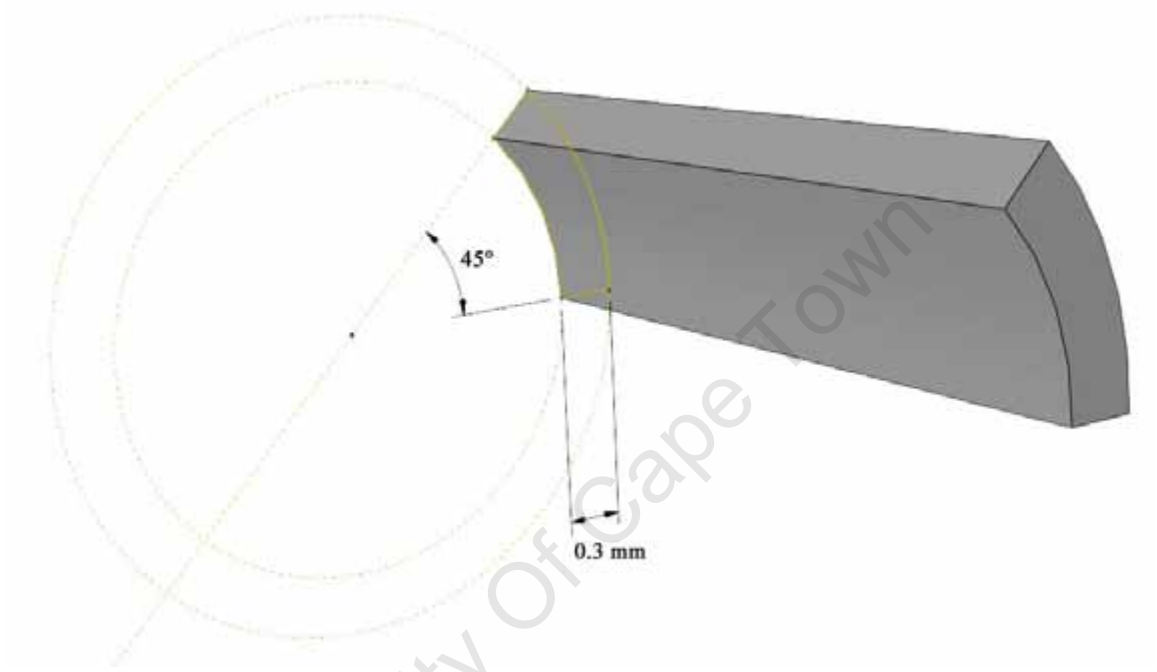

Figure 3-3: Extruded PPU tube geometry.

3.1.1.3.Graft Assembly

The two graft assemblies; EX and EM, were constructed as two different reinforcement systems. The inner diameter of the wire mesh was preserved at 3.0mm and the outer diameter of the PPU tube was adjusted such that the wire mesh was placed around and embedded in the PPU tube, forming EX and EM respectively. However, in both assemblies the thickness of the PPU tube was kept unchanged.

In the EX assembly the outer diameter of the PPU tube was matched with the inner diameter of the wire mesh to have the wire mesh exactly at the external surface of the PPU tube. This resulted in a PPU tube inner diameter of 2.4mm.

For the EM assembly, the inner diameter of the PPU tube (and its outer diameter to preserve the thickness) was increased in order to completely contain the wire mesh. The

PPU tube was optimised in such way that the wire mesh was centred in the tube volume, as shown in Figure 3-4. This resulted in a PPU tube with inner diameter of 2.8mm.

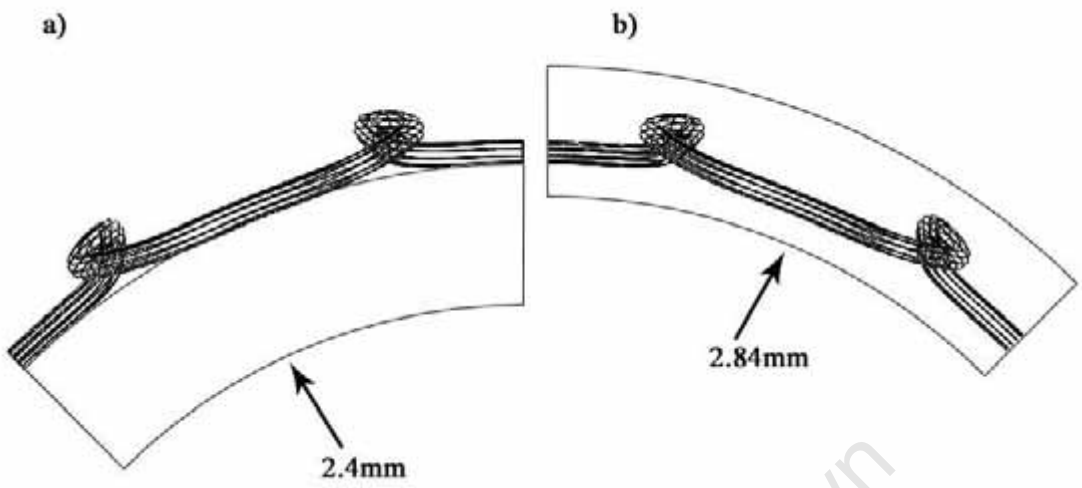

Figure 3-4: Cross-sectional view showing different positions of PPU tube in the EX (a), and EM (b) assemblies.

3.1.2.Material Models

Three materials were involved in this study; PPU, NITI and solid PU wire mesh. Their mechanical properties had to be gathered to build up material models for the FE analysis. The PPU tube and NITI wire mesh were characterized in previous studies (Yeoman 2004; van der Merwe 2007; van der Merwe et al. 2008; Yeoman et al. 2009) conducted at the Cardiovascular Research Unit (CVRU). For the solid PU wire material, data from generic material was used.

3.1.2.1.Porous Polyurethane

The PPU material was characterised, modelled and validated in previous studies (Yeoman 2004; Yeoman et al. 2009). Samples of PPU tubes (pores size= 125-150μm, internal diameter 4.0mm) underwent tensile, compressive and shear tests (Instron 5544; Instron, Norwood, MA; water, 37°). Tensile and compressive specimens were 30 and 5mm in length, and the dimensions of the shear specimen was 5×5×10mm. Data was obtained from three samples for each test.

The PPU material was modelled using Abaqus intrinsic hyperfoam material model. This forth-order isotropic material model was defined by specifying the coefficients of the

hyperfoam strain energy potentials based on Ogden's strain energy function (Eq. (2.6)). The least squares method was used to fit the material coefficients to the data obtained from the tensile, compression and shear tests. The final parameters used to define the hyperfoam material model are shown in Table 3-1.

Table 3-1: The coefficients used in the hyperfoam material model (Yeoman 2004).

Description	Unit	Value
Poisson's Ratio (υ)	-	0.035
μ_1	MPa	0.19262
μ_2	MPa	-0.03373
μ_3	MPa	-0.08682
μ_4	MPa	0.02566
α_1	-	1.2571
α_2	-	1.2655
α_3	-	-2.6509
α_4	-	-4.6589

Validation tests for the PPU material model were conducted by Yeoman et al. (2009) using three single element patch models. These models incorporated uniaxial tensile, compression and simple shear tests using a single eight-noded plane stress cubic element. BC and loading were applied in such a way to represent different test conditions. Stress vs. strain curves were obtained from these models and compared to the physical data of previously conducted experiments. It was shown that the numerical models were valid to strains of 55% for uniaxial tension, 30% for compression and 35% for shear.

3.1.2.2.Nitinol

Characterization, modelling and validation of the NITI material were carried out in previous studies (van der Merwe 2007; van der Merwe et al. 2008). Characterization tests were implemented using 12 samples of NITI wires of 0.05, 0.0635 and 0.075mm diameters and 100mm length. The wires underwent cyclic uniaxial tensile test (Instron 5544; Instron, Norwood, MA; water, 37°) up to 4.5% of strain. The stress vs. strain curves of the first 3 and the last 2 cycles, of the 99 cycles performed on each wire sample, were used to obtain data. This was based on 4 nominated regions, illustrated in Figure 3-5, by averaging the linear trend equations obtained at each region.

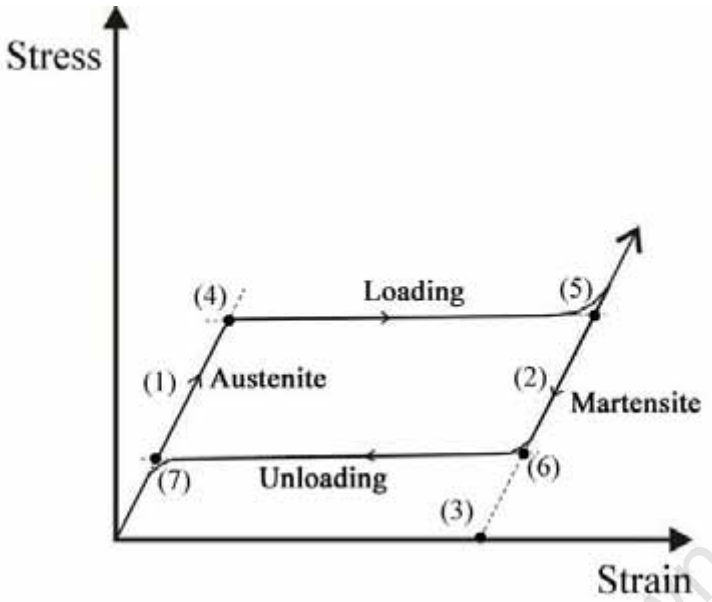

Figure 3-5: Cyclic stress vs. strain curve of NITI showing the four nominated regions and positions of extracted data (modified from van der Merwe (2007)).

The values which were extracted from the final average equations included:

- Austenite young's modulus (Figure 3-5 (1)).
- Martensite young's modulus (Figure 3-5 (2)).
- Transformation strain (Figure 3-5 (3)).
- Start-of-transformation loading stress (Figure 3-5 (4)).
- End-of-transformation loading stress (Figure 3-5 (5)).
- Start-of-transformation unloading stress (Figure 3-5 (6)).
- End-of-transformation unloading stress (Figure 3-5 (7)).

The NITI material model was defined as Abaqus user-material for superelasticity of shape memory alloy. Table 3-2 shows the predefined input parameters and their values which were obtained from the experiments and from Medtronic Vascular, Galway, Ireland.

Table 3-2: Parameters and values of the NITI material model (van der Merwe 2007).

Parameter	Unit	Value
Austenite Young's Modulus	MPa	38992
Austenite Poisson's Ratio	-	0.46
Martensite young's Modulus	MPa	21910
Martensite Poisson's Ratio	-	0.46
Transformation Strain	-	0.042
Loading Temperature Derivative of Stress	MPa/°C	0
Loading Start of Transformation Stress	MPa	483
Loading End of Transformation Stress	MPa	610
Reference Temperature	MPa	37
Unloading Temperature Derivative of Stress	MPa/°C	0
Unloading Start of Transformation Stress	MPa	388
Unloading End of Transformation Stress	MPa	256
Loading Start of Transformation Stress (Compression)	MPa	610
Volumetric Transformation Strain	-	0.04
Number of Annealings to be Performed During Analysis	-	0

The validation of the NITI material model was performed by van der Merwe et al. (2008) by developing a single-cycle uniaxial tensile model of a cylindrical geometry and cross-sectional diameter of 0.0625mm. Due to memory limitations, applying the actual length of the wire specimens (i.e. 100mm) was inapplicable. Alternatively, two models were developed with lengths of 10 and 50mm, respectively. Displacement BC were applied to both wire ends, so that one was fully constrained while the other moved longitudinally up to 13% of strain during loading, and dropping back to 0% during unloading. Models were meshed using eight-node brick elements, with the wire cross section having 6×4 elements fashion along the two perpendicular directions. Since the final input values of the NITI material model were obtained as an average of a number of curves, the stress vs. strain curve obtained from the uniaxial tensile models was compared against the expected stress vs. strain curve based on the final input values used in material model definition.

Both models (i.e. 10 and 50mm long) exhibited identical stress vs. strain curves and the stress values at points (4), (5), (6) and (7) in Figure 3-5 were found to be similar to the input values of the material model.

3.1.2.3.Solid Polyurethane

An isotropic linear elastic material was introduced to describe a generic PU material for the wire mesh, utilizing an elasticity modulus of 570MPa and a material density of 1025kg/m^3 (Franz 2009). The usage of linear elastic model for the solid PU material in this study was assumed satisfactory for assessing the graft mechanics under a reinforcing mesh of less stiffness, compared to the NITI mesh. In another study investigating the deployment of a balloon-expandable stent, Mortier (2010) utilized a linear elastic constitutive model to describe a cylindrical PU balloon, applying material data of PU ureteral stents (Gorman et al. 1997).

3.1.3.Finite Element Mesh

The same method used in generating the FE mesh was applied on both the wire mesh and PPU tube structures. A specified number of elements were assigned along a particular edge by means of local seeding technique. The mesh then was generated automatically dependently on the predefined element type. Both geometries were meshed using 8-node linear brick elements.

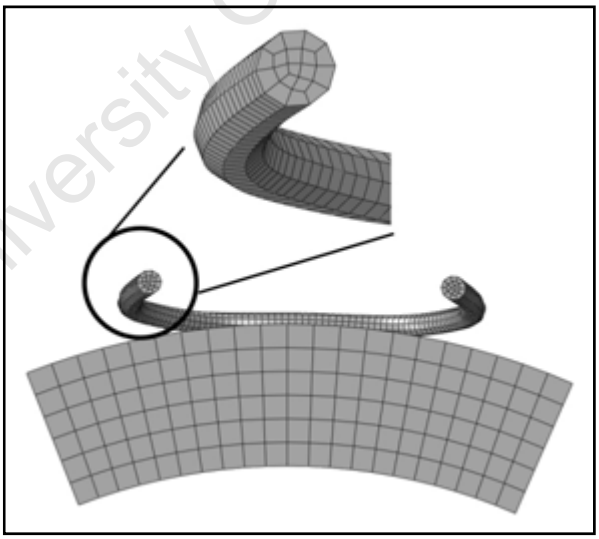

Figure 3-6: The 8-node brick elements across the PPU graft (6 elements along the thickness) and wire loops structures (10 elements along the edge).

Figure 3-6 illustrates the generated FE mesh. In the wire loops, 10 elements were assigned along the circumference of the wire cross-section. The thickness of the PPU tube was assigned 6 elements by seeding its radial edge.

3.1.4.Boundary Conditions

In order to simulate the physical situation of the structures and to compensate for the partial modelling, two sets of BC were introduced into the models. The first set was applied on the longitudinal cross sections of the wires and the PPU tube, denoted by letter L in Figure 3-7. This set of BC governed the movement in the longitudinal direction. The second set was applied on the circumferential cross sections of the wires and the PPU tube, denoted by letter C in Figure 3-7. This set of BC governed the movement on the circumferential direction. Due to the tubular shape of the structure, a cylindrical co-ordinate system (i.e. r, θ, and z) was introduced so as to facilitate the definition of the BC, in which r, θ and z represented the radial, circumferential and longitudinal axes, respectively.

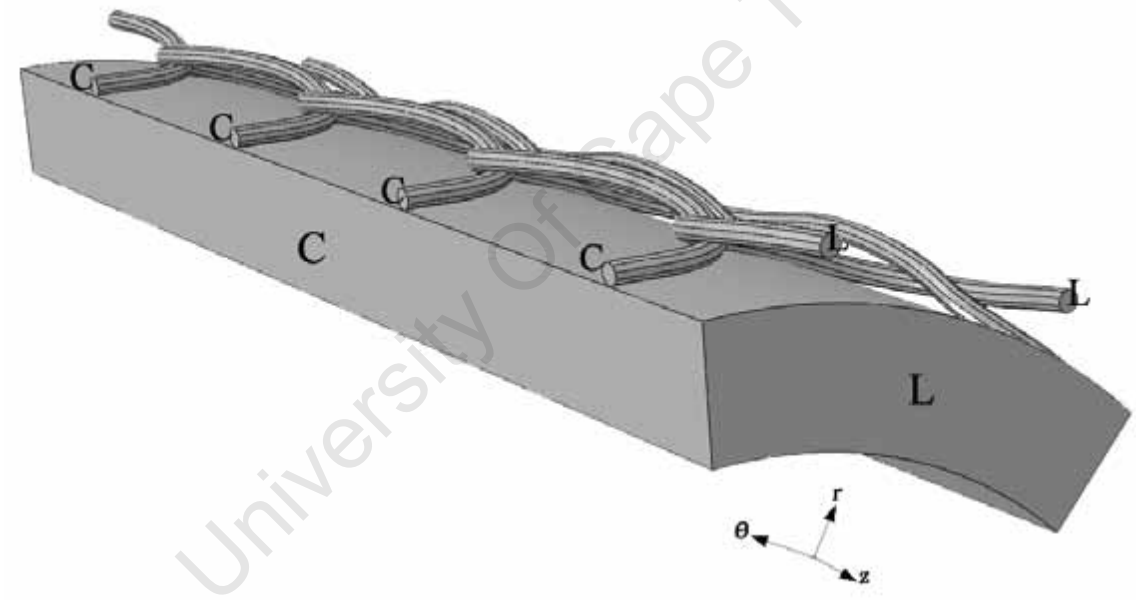

Figure 3-7: The predefined circumferential and longitudinal BC on the EX model.

The longitudinal BC was defined by preventing the movement in the longitudinal direction (z) and rotation around the radial (r) and circumferential (θ) directions. The circumferential BC was defined by preventing the movement in the circumferential direction and rotation around radial and longitudinal directions. As a result, the constrained cross sections were only allowed to move in the radial direction, as shown in Figure 3-8. Similar BC was utilized for the EM assembly.

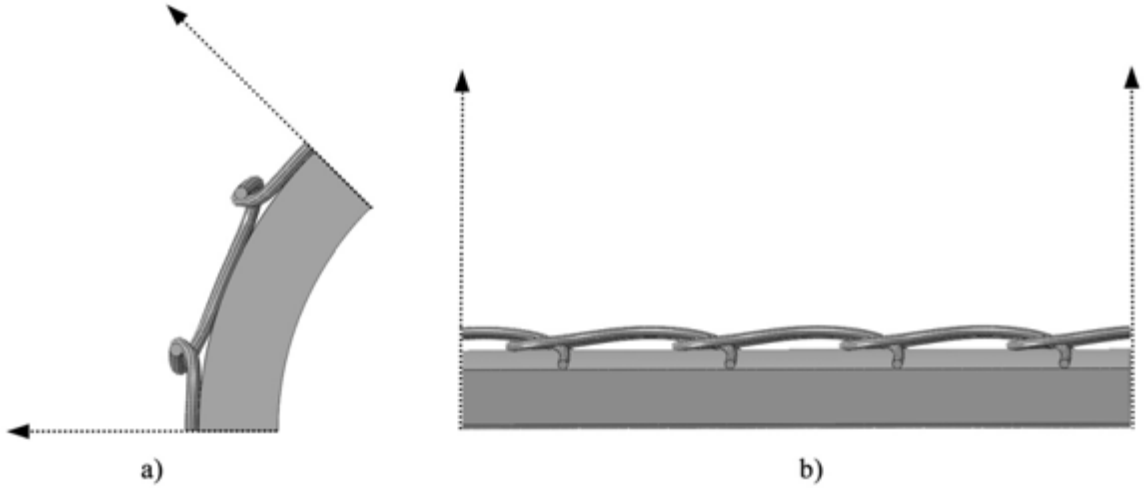

Figure 3-8: The movement directions of the circumferential (a), and longitudinal (b) ends of the EX model.

3.1.5.Contact Definition

The contacts between the PPU tube and the wire mesh and between the individual wire loops were modelled. A surface-to-surface contact with finite sliding was defined between all contact pairs by application of exponential pressure-overclosure relationship. Referring to Figure 3-2(c), master-slave contact pairs were defined between surfaces of individual single loop parts in a sequential order starting from the back partial loop towards the front partial loop, in such a way that loop *n* acted as a master to loop *n+1*. Additionally, the entire surfaces of the wire mesh loops were set as slave surfaces to the external surface of the PPU tube which was set as a master surface.

In the EM models, the contact between the wires loops was defined similar to the EX models, however, the contact between the surfaces of the PPU tube and the wire mesh was not applicable since the wire mesh was embedded inside the tube. The embedded region constraint (Abaqus 2008) was applied in which the elements of the wire mesh were defined as embedded elements surrounded by host elements of the PPU tube.

The initial pressure-clearance values were always set to (0.5MPa, 0mm)/(0MPa, 0.005mm). The pressure value in this relationship was adjusted frequently in order to achieve numerical stability among different models, as will be discussed later.

3.1.6.Friction Modelling

The relative movement between the individual wire loops and between the wire loops and the PPU tube was not restrained. The friction between the graft components played a role in limiting such movement which in turn would have an impact on the mechanical behaviour of the graft. Therefore including the friction in the models was necessary to attempt a realistic simulation. This can was implemented by considering of static and kinetic friction.

A frictional tangential behaviour was incorporated in the models. This was implemented through friction formulation based on static-kinetic friction exponential decays. The friction was introduced between individual NITI wire loops, between individual PU wire loops, and between PPU tube and both NITI and PU wire meshes. The values of the static and kinetic friction coefficients along with the decay coefficients are shown in Table 3-3.

Table 3-3: Friction coefficients used in friction definition.

Contact Area	Static Coefficients	Kinetic Coefficients	Decay Coefficients
Individual NITI wire loops	0.3	0.25	1x10-5
Individual PU wire loops	0.5	0.45	1x10-5
PPU tube and NITI wire mesh	0.2	0.18	1x10-5
PPU tube and PU wire mesh	0.5	0.45	1x10-5

3.1.7.Loading

Loading was defined in the models as a uniformly distributed pressure applied to the luminal surface of the PPU tube as shown in Figure 3-9. The pressure was increased linearly with time from 0 to 200mmHg to cover the physiological blood pressure range (see Figure 3-10).

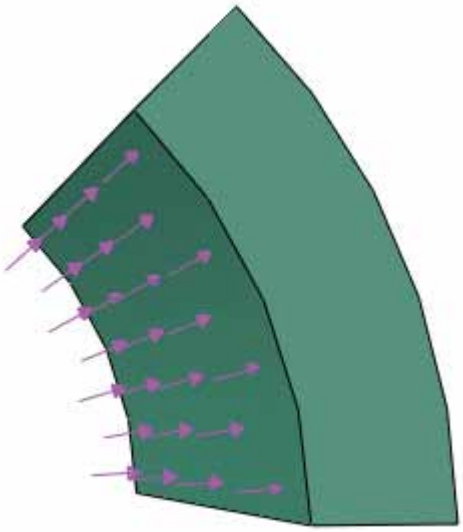

Figure 3-9: Uniform distribution of pressure on the inner surface of the PPU tube.

3.1.8.Analysis Predefinitions

The simulation was carried out in two steps, as illustrated in Figure 3-10. The first step was a contact initialization step. It involved contact establishment between the contact pairs described previously. The pressure application was executed in the second step.

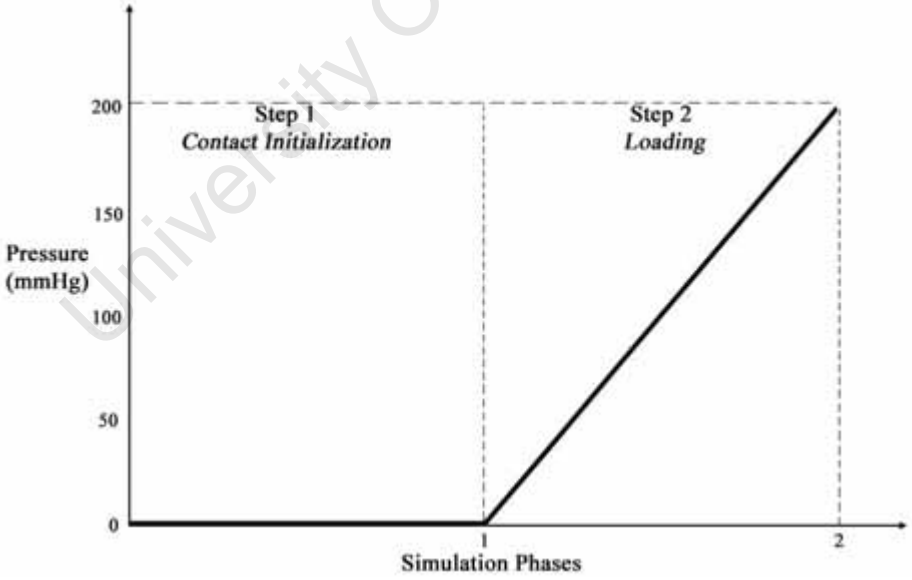

Figure 3-10: Pressure status during simulation phases: linear increase during loading.

An automatic time incrementation approach was used to control the time increments during each step. The basic time period of the step was set to 1.0. The values of the initial increment and the allowable maximum and minimum increments were adjusted to 0.1, 1×10^{-12} and 0.025 respectively. Since the pressure loading was increased with time,

particularly the time increments, predefined time points were introduced to adjust the increments size to be precisely equivalent to 80 and 120 mmHg. This allowed capturing of the output data at these particular pressure values.

Due to instability experienced in the models, an automatic stabilization was defined to allow an adaptive calculation of damping factor based on a predefined dissipated energy fraction and a maximum ratio of stabilization energy to strain energy. The damping factor was calculated based on the solution of the first increment of a step and determined in such a way that the dissipated energy for a given increment with characteristics similar to the first increment was a small fraction (i.e. the dissipated energy fraction) of the extrapolated strain energy (Abaqus 2008). The initial values used were 2×10^{-4} and 0.2 for the dissipated energy fraction and the maximum ration of stabilisation to strain energy, respectively. These values were adjusted when required, along with the contact definition parameters, depending on individual models behaviour in order to establish stability and solution convergence.

The numerical stability is an important issue which might influence the model behaviour leading to an incorrect physical interpretation. The numerical stability of a model was monitored through its strain energy response when plotted against the applied pressure, Figure 3-11, in conjunction with the radial deformation curve of the model. The discontinuity in the strain energy curve (curve a in Figure 3-11) was always indicated by reduction in the strain energy level. This was treated as a numerical instability and confirmed by ensuring that the radial expansion did not show an associated discontinuity. By adjusting the stabilisation and contact settings the shape of the curve was improved (curves b and c) until a smooth strain energy curve (curve d) was achieved. Such smooth trends of strain energy curves were assumed as indication of model stability.

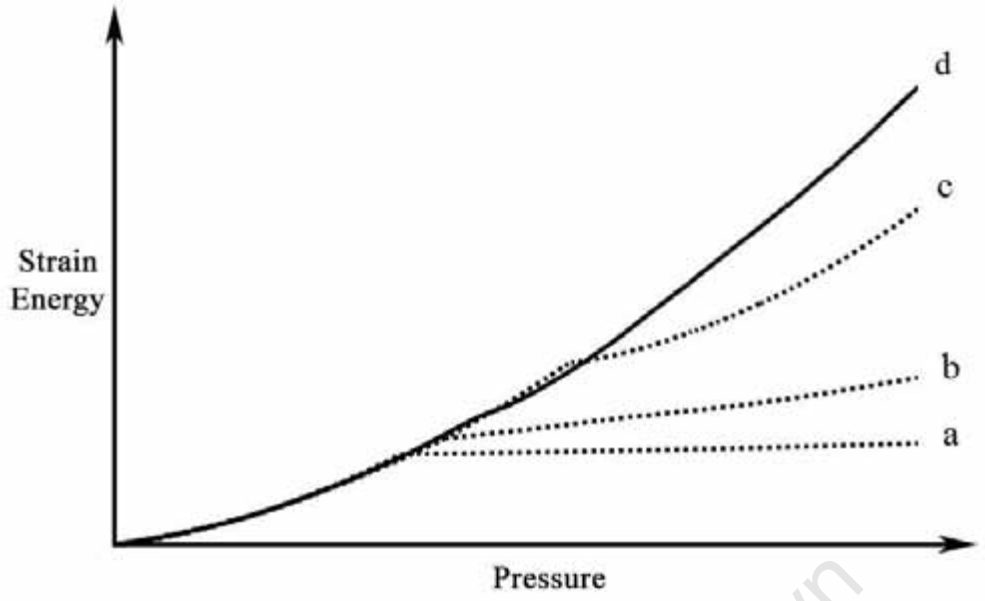

Figure 3-11: Strain energy curve as model stability criteria.

3.1.9.Postprocessing

In a postprocessing stage, the pressure-diameter relationship, the radial compliance and wall compression were determined for different models. This was based on the radial displacement predicted for the models.

The inner and outer surfaces of the PPU tube in the EX and EM models exhibited non-uniform radial displacements. This was attributed to the presence of the wire mesh structure which cased tube bulges. However, when the radial displacement of each individual node on the inner surface, for example, of the PPU tube was plotted, as shown in Figure 3-12, an overall sinusoidal trend was exhibited. The sinusoidal trend was predicted at all pressure values with changes in displacement peaks. These outcomes supported the approach of determining the pressure-diameter relationship, the radial compliance and wall compression based on the averaged nodal radial displacement value on the inner and outer surfaces of the PPU tube.

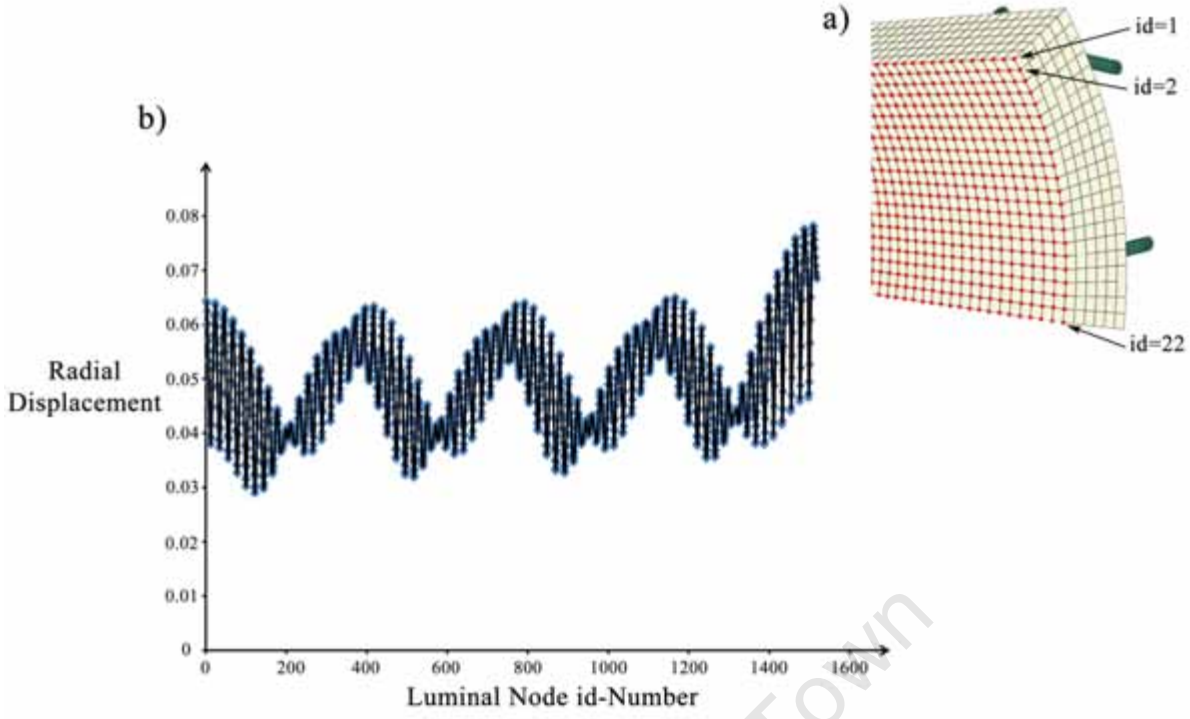

Figure 3-12: The PPU tube luminal nodes (a), and their sinusoidal trend of displacement at a particular luminal pressure (b).

3.1.10.Models Attributes

The EX and EM assemblies were used to develop four models by varying the material of the wire mesh. Two additional models were introduced to investigate the two versions of the PPU tubes (i.e. 2.4 and 2.8mm inner diameter) without reinforcement. This subsection describes these models and highlights their specific conditions and parameters. The presented models include:

a) NITI external reinforcement graft (NIEX).
b) NITI embedded reinforcement graft (NIEM).
c) PU external reinforcement graft (PUEX).
d) PU embedded reinforcement graft (PUEM).
e) Bare graft, of the EX assembly (BG2.4).
f) Bare graft, of the EM assembly (BG2.8).

3.1.10.1.External Reinforcement Models

The NIEX and PUEX models were developed by assigning NITI and PU material models to the wire mesh of the EX assembly, respectively. Based on the stability evaluation

approach described in section 3.1.8, both models experienced numerical stability problems when run under initial stabilisation and contact parameters mentioned earlier. The updated settings are shown in Table 3-4. Although initial stabilisation for NIEX was sufficient, dissipated energy fraction had to be increased for PUEX. Solution convergence and smooth strain energy trend were achieved for both models by adjusting the pressure value associated with zero clearance.

Table 3-4: Summary of the EX models.

Model	Contact	Dissipated Energy Fraction	Number of Elements	Number of Nodes
NIEX	(12MPa, 0 mm)/(0Mpa, 0.005 mm)	2×10^{-4}	20,055	27,250
PUEX	(2MPa, 0 mm)/(0Mpa, 0.005 mm)	2×10^{-3}	20,055	27,250

3.1.10.2.Embedded Reinforcement Models

The NIEM and PUEM models were created with the material model for the wire mesh being set to NITI and PU, respectively. Unlike the EX models, the EM models did not show numerical stability problems when run with initial contact and stabilisation settings. Therefore those initial settings were kept unchanged for both NIEM and PUEM models, as summarized illustrated in Table 3-5.

Table 3-5: Summary of the EM models.

Model	Contact	Dissipated Energy Fraction	Number of Elements	Number of Nodes
NIEM	(0.5MPa, 0 mm)/(0Mpa, 0.005 mm)	2×10^{-4}	28,579	28,687
PUEM	(0.5MPa, 0 mm)/(0Mpa, 0.005 mm)	2×10^{-4}	28,579	28,687

3.1.10.3.Bare Graft Models

The 2.4 mm and 2.8 mm inner diameter PPU tubes, which were used in the EX and EM assemblies, were set free from reinforcement in two models; BG2.4 and BG2.8. These bare graft (BG) models were examined under the same conditions of applied luminal pressure and BC to evaluate the possible impact of the different reinforcement on their mechanical and physical behaviour. The two models experienced convergence difficulties. The final models had their dissipated energy fraction increased as shown in Table 3-6.

Table 3-6: Summary of BG models.

Model	Dissipated Energy Fraction	Number of Elements	Number of Nodes
BG2.4	2×10^{-2}	8,568	10,626
BG2.8	2×10^{-2}	9,792	12,075

3.2.Finite Element Verification

The following section introduces the procedure undertaken to verify the applied mesh density, element type, BC, contact, and friction of the FE models used in the study.

3.2.1.Mesh Refinement Verification

The NIEX and PUEX models underwent mesh refinement test to examine the sensitivity of the models to the change in mesh density. Three versions of each of these models were considered by having three different mesh densities, as shown in Figure 3-13. Coarser and finer mesh densities were generated from the original models mentioned in Section 3.1.10.1. The coarser models (suffixed with *-coarse*) were generated by reducing the number of elements across the PPU tube thickness to 4. The finer models (suffixed with *-fine*) were generated by raising the number of elements along the edge of the wire loops to 14. Table 3-7 compares the different mesh densities.

Table 3-7: Mesh densities of the refined models.

Models	Number of Elements	Number of Nodes
NIEX-*coarse* PUEX-*coarse*	13,827	19,832
NIEX PUEX	20,055	27,250
NIEX-*fine* PUEX-*fine*	37,260	48,920

To achieve numerical stabilisation and convergence in the new refined models, slight adjustment to the contact and energy dissipation parameters of the original models was performed, as shown in Table 3-8.

Table 3-8: Contact and stabilisation settings for coarser and finer models.

Model	Contact	Dissipated Energy Fraction
NIEX-*coarse*	(10MPa, 0mm)/(0Mpa, 0.005mm)	2×10^{-4}
NIEX-*fine*	(12MPa, 0mm)/(0Mpa, 0.005mm)	2×10^{-3}
PUEX-*coarse*	(3MPa, 0mm)/(0Mpa, 0.005mm)	2×10^{-4}
PUEX-*fine*	(3MPa, 0mm)/(0Mpa, 0.005mm)	2×10^{-3}

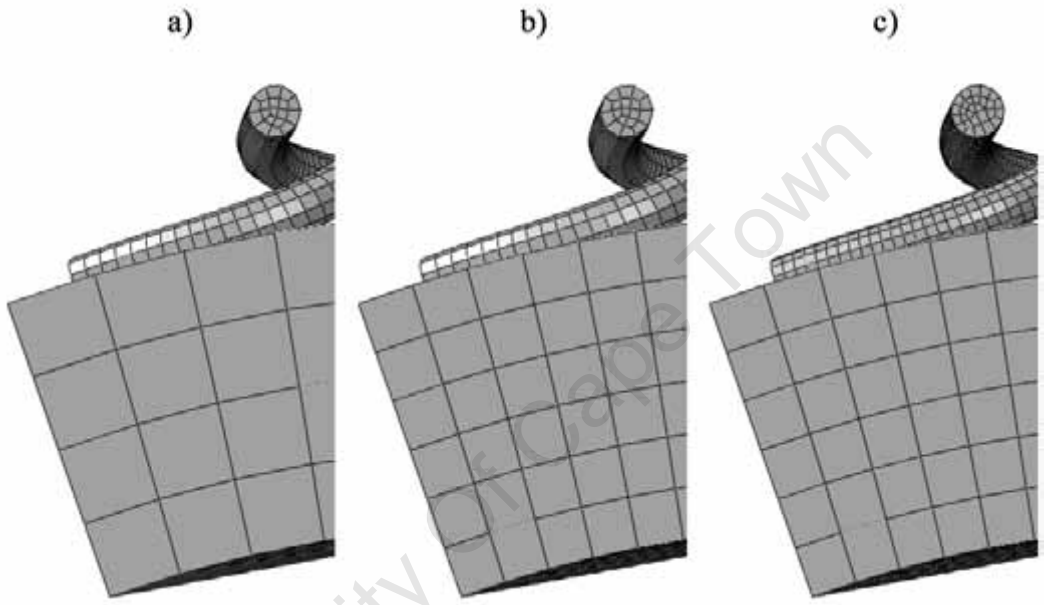

Figure 3-13: Mesh refined models: a) The coarse model, b) The original model, c) The Fine model.

3.2.2.Element Type Verification

The behaviour of the models with a different type of element had to be evaluated to verify the usage of the brick element. Although the brick element was verified for the PPU tube (Yeoman 2004) and wire mesh (van der Merwe 2007) geometries, an attempt was made in this study to verify this element type for the combined assembly of the two structures. The FE mesh of models NIEX and PUEX were regenerated using 10-node quadratic tetrahedral element providing two new models NIEX-TET and PUEX-TET. The mesh density of the newly developed models was chosen to have the same number of nodes the brick element models had, as shown in Table 3-9. The intended strategy was to run NIEX-TET and PUEX-TET models, generate models with less mesh density and then compare the result.

Table 3-9: Mesh density of models with brick vs. tetrahedral elements.

Models	Number of Elements	Number of Nodes
NIEX PUEX	20,055	27,250
PUEX-TET PUEX-TET	14,642	27,112

3.2.3.Boundary Condition Verification

A modified version of NIEX model, namely NIEX-BCV, was created for BC verification. The circumferential BC assigned to the PPU tube was removed and alternatively a cyclic symmetry interaction (Abaqus 2008) was introduced by assigning the circumferential surfaces of the PPU tube as master and slave surfaces, respectively, and the *z*-axis as the axis of symmetry. The total number of repetitive sectors was set to 8 sectors. The BC on the wire mesh along with other parameters were kept unchanged. Solution convergence was managed by only setting the contact to (13MPa, 0 mm)/(0MPa, 0.005 mm).

The procedure used previously to obtain displacement information, as mentioned in section 3.1.9, was technically not applicable when using cyclic symmetry definition (Abaqus 2008). This was rectified using another approach by predefining a set of nodes on both the luminal and external surfaces of the PPU tube and then using this set as a source of displacement information. These nodes were chosen from different displacement contour spots, as illustrated in Figure 3-14, to get a reasonable approximation. For the purpose of accuracy in comparison, the displacement information was taken from NIEX model again based on the same set of nodes.

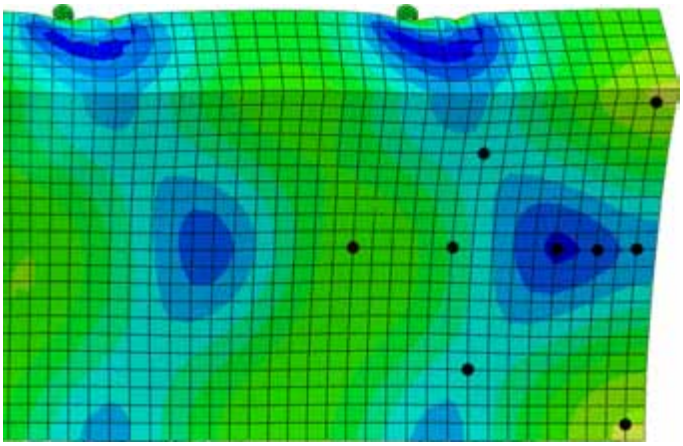

Figure 3-14: The predefined nodes for approximation of luminal surface displacement.

3.2.4.Contact Definition Verification

As stated in earlier, the contact definition, particularly the pressure value associated with the zero clearance on the pressure-clearance relationship, was altered frequently to achieve numerical stability of models. To evaluate the influence of changing the contact definition on the model response, two versions of model NIEX were compared to the final model. The first presented version, namely NIEX-CV1, had the initial pressure-clearance values i.e. (0.5MPa, 0mm)/(0MPa, 0.005mm), and the second version had (9MPa, 0mm)/(0MPa, 0.005mm) and named NIEX-CV2. The dissipated energy fractions in these models were not changed (i.e. kept at 2×10^{-4}).

3.2.5.Friction Verification

In order to evaluate the sensitivity of models to the frictional tangential contact between different parts, models NIEX and NIEM were examined under frictionless contact defined between the wire mesh and the PPU tube and between the individual wire loops. The new frictionless models were assigned the names NIEX-FL and NIEM-FL, respectively. In model NIEX-FL, the contact parameters were set to (10MPa, 0mm)/(0MPa, 0.005mm) and dissipated energy fraction was set to 7×10^{-3}. However, model NIEM-FL ran smoothly without the need to change the initial parameters settings. The results of these models were compared to the original frictional models.

4. Results

4.1.Finite Element Analysis

The developed models underwent FE analysis to evaluate their response when subjected to increasing luminal pressure load up to 200mmHg, as described in section 3.1. The analysis was run using automatically controlled increments of time and load controlling the load application. This section introduces seven output variables used to assess and compare the models. Some of these variables were obtained automatically as Abaqus output variables, such as strain energy, maximum principal stress and strain, and martensite fraction, while postprocessing was required to obtain the other variables; such as pressure-diameter relationship, compliance and wall compression.

4.1.1.Strain Energy

The graphs in Figure 4-1 to Figure 4-3 show plots of strain energy versus the applied luminal pressure of the EX, EM and BG models, respectively. The strain energy plots of the BG models were separated from the other models for better presentation.

Both the EX and EM models showed a similar increase of strain energy up to 40mmHg. As the pressure increased beyond this value, the strain energy of the EX models started to increase with the NIEX and PUEX models having more than approximately double the strain energies of the NIEM and PUEM models, respectively, at 200mmHg. In both EX and EM models, the NITI-reinforced graft showed lower ranges of strain energies than the PU-reinforced graft.

The strain energy curves of the BG models showed an exponential trend with a linear part up to an approximate pressure value of 120mmHg, after which an extreme increase in the slope of both curves was seen. The curves of the BG models correlated with each other until the pressure value of 100mmHg. At a given pressure, BG2.8 had larger values than BG2.4. The FE analyses of these models did not complete due to numerical instability. Model BG2.8 terminated when the pressure approached 150mmHg, while model BG2.4 terminated as approaching a pressure of 170mmHg. The slopes of the strain energy curves tended to have an infinite value as approaching these pressure values.

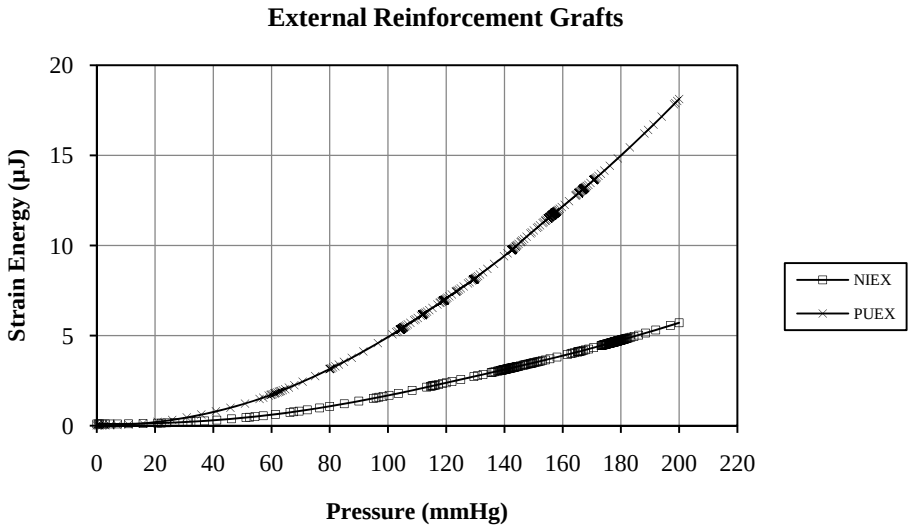

Figure 4-1: Strain energy versus luminal pressure for the EX models.

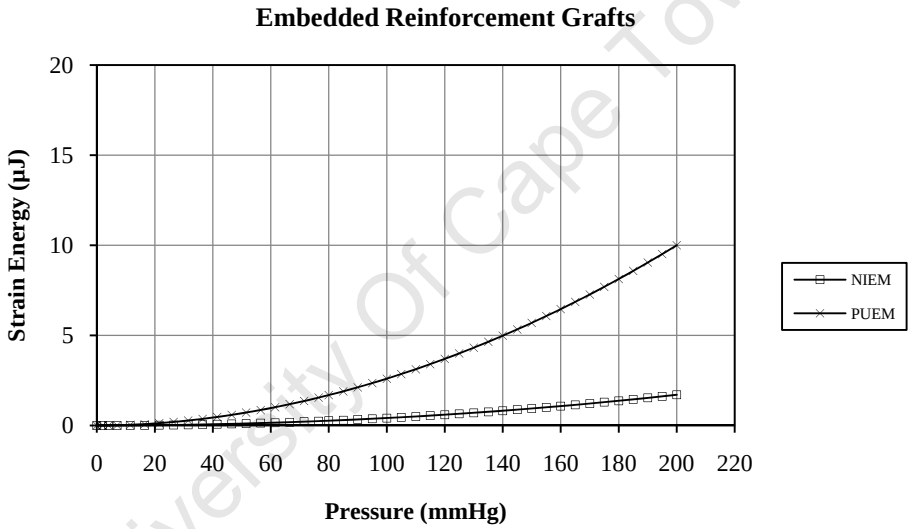

Figure 4-2: Strain energy versus luminal pressure for the EM models.

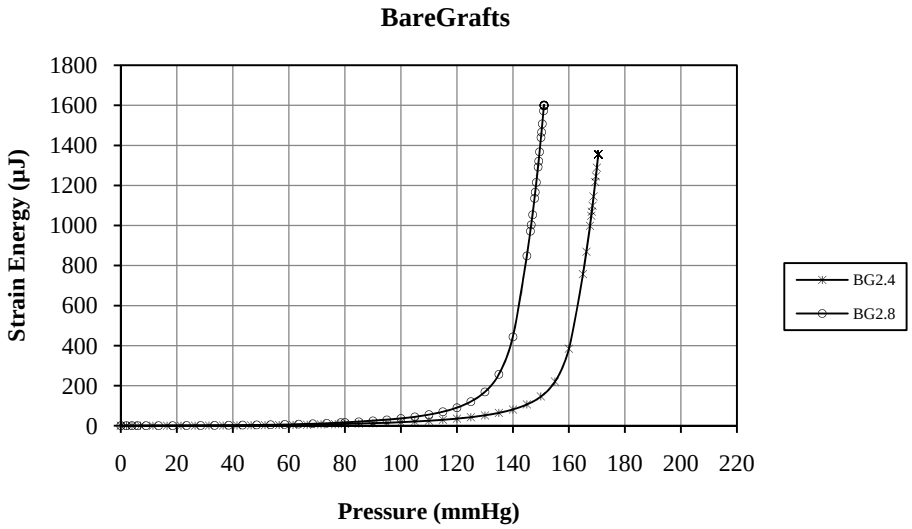

Figure 4-3: Strain energy versus luminal pressure for the BG models.

4.1.2.Pressure-Diameter Relationship and Compliance

In Figure 4-4 to Figure 4-6, the luminal pressure was plotted versus the increase in the inner diameter expressed as relative change to initial inner diameter of the EX, EM and BG models. The pressure was plotted on the vertical axis to match the graphs usually used in medical field (for compliance calculation). The pressure-diameter curves of the BG models were plotted in a separate graph for better presentation.

The NIEX and PUEX models experienced a steady increase in the inner diameter. The inner diameter of both models at 0mmHg was less than 2.4mm. This reduction occurred during the contact initialization step in order to bring the PPU tube and the wire mesh into a contact based on the predefined settings. At a given pressure, the PUEX model always showed greater change in the inner diameter than the NIEX and this difference increased as the pressure increased.

The NIEM and PUEM models dilated linearly with increasing pressure. Similar to the EX models, the maximum dilation of 2.5% at 200mmHg of the NIEM model was less than that of the PUEM model (i.e. 14%).

Similar to the strain energy plots, the pressure-diameter curves, in Figure 4-6 , showed a considerable increase in the inner diameter of the BG2.8 and BG2.4 models as the load approached 150mmHg and 170mmHg, respectively.

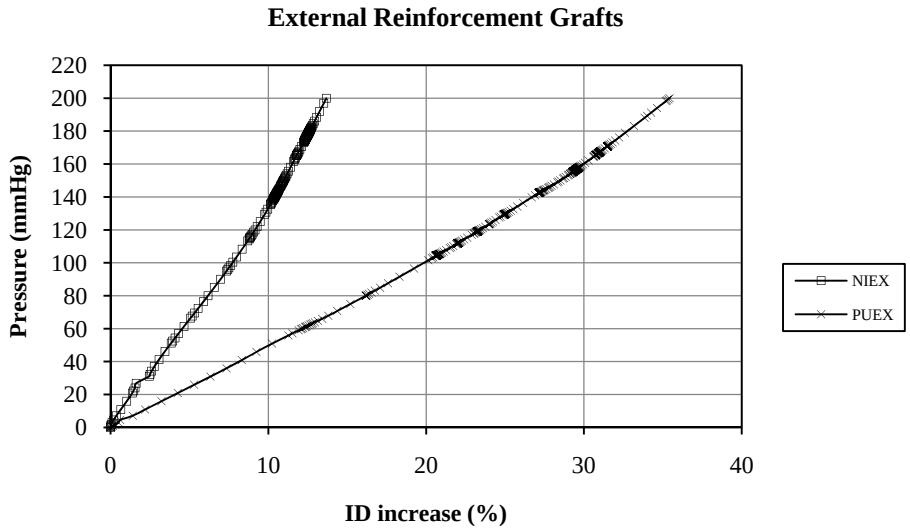

Figure 4-4: Radial deformation of the EX models expressed as luminal pressure versus inner diameter increase.

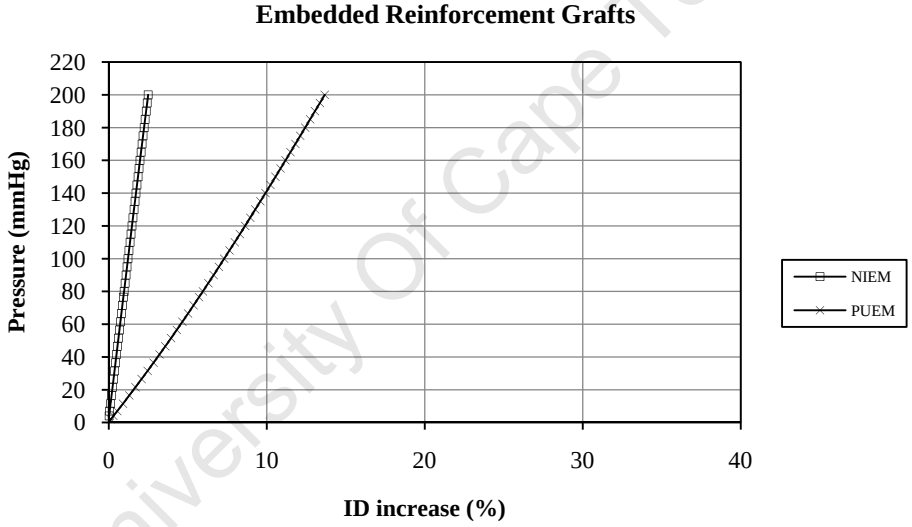

Figure 4-5: Radial deformation of the EM models expressed as luminal pressure versus inner diameter increase.

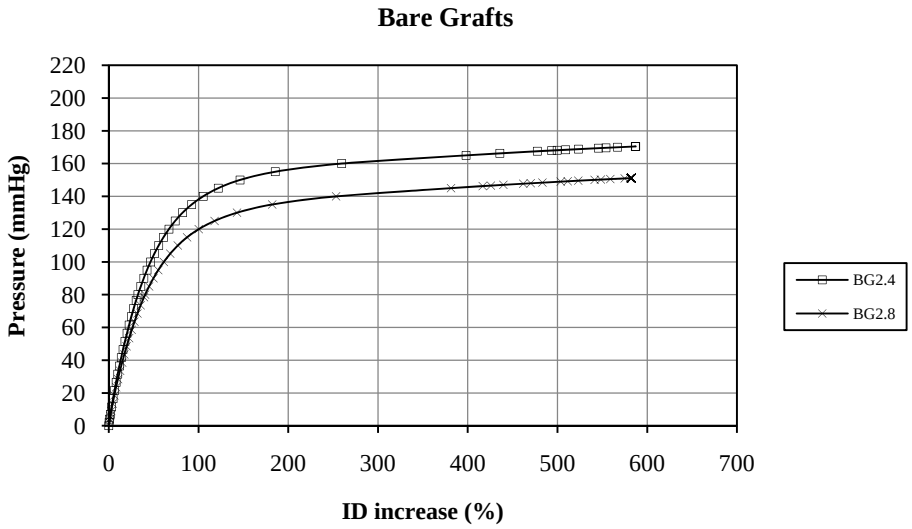

Figure 4-6: Radial deformation of the BG models expressed as luminal pressure versus inner diameter increase.

The radial compliance of the different models was calculated, in a postprocessing stage as described in section 3.1.9, using the information of the radial displacement at diastolic and systolic pressure of 80 and 120mmHg, respectively. Table 4-1 shows the calculated values for radial compliance of the different graft models. The compliance of the grafts was considerably reduced by the influence of the reinforcement.

Table 4-1: Radial compliance for the FE models, calculated between 80 and 120mmHg.

Model	Compliance (%/100mmHg)
NIEX	7.02
PUEX	15.57
BG2.4	65.05
NIEM	1.24
PUEM	6.31
BG2.8	106.41

4.1.3.Wall Compression

The compression of the PPU tube was determined in the postprocessing phase, by utilizing the information of the displacements of the internal and external surfaces. Table 4-2 summarizes the maximum and minimum wall compression values predicted by the FE models at different pressure levels.

Table 4-2: Wall compression in the PPU tube of the FE models at 80, 120 and 200mmHg.

Model	Wall Compression (%)					
	80 mmHg		120 mmHg		200 mmHg	
	Maximum	Minimum	Maximum	Minimum	Maximum	Minimum
NIEX	13.90	0.93	24.21	3.15	37.24	6.12
PUEX	14.92	3.01	23.44	4.81	36.32	8.74
BG2.4	4.06	4.06	7.79	7.79	-	-
NIEM	3.65	0.03	5.60	0.13	9.86	0.50
PUEM	3.95	0.97	6.07	1.46	11.0	2.46
BG2.8	4.54	4.54	9.96	9.96	-	-

Compared to the BG models, the external reinforcement increased the wall compression and the embedded reinforcement reduced the wall compression. The EX models predicted higher compression values than the EM models. Within each reinforcement system, both the NITI-reinforced and PU-reinforced models recorded nearly equal values of maximum wall compression.

The wall compression data of the BG models at 200mmHg was not available since the simulation was terminated prior to this pressure.

4.1.4.Maximum Principal Stress

Stresses were induced in the FE models due to the deformation caused by the pressure load. These were recorded at each time increment of the analysis as stated previously.

Table 4-3 shows the maximum principal stress predicted in the individual components of the FE models (i.e. the PPU tube and the wire mesh) at three pressure levels; the diastolic and systolic pressures, and 200mmHg. In both reinforcement systems the NITI wire mesh exhibited higher stress compared to the PU wire mesh. The stress predicted by the BG models at 200mmHg was not available as the simulation terminated before reaching this pressure. Both external and embedded reinforcement systems caused a reduction in the stress levels in the PPU tube at diastolic and systolic pressures compared to the BG models. Regardless of the reinforcement type, higher stress was predicted in the PPU tube under the PU reinforcement compared to the NITI reinforcement.

Table 4-3: Maximum principal stress in components of the FE models, at 80,120 and 200mmHg.

Model	Maximum Principal Stress (MPa)					
	80 mmHg		120 mmHg		200 mmHg	
	PPU tube	Wire mesh	PPU tube	Wire mesh	PPU tube	Wire mesh
NIEX	0.020	73.68	0.031	97.0	0.046	157.90
PUEX	0.036	18.98	0.055	28.08	0.093	45.12
BG2.4	0.066	-	0.132	-	-	-
NIEM	0.012	57.59	0.019	86.72	0.034	145.60
PUEM	0.037	16.76	0.055	24.67	0.091	39.45
BG2.8	0.081	-	0.186	-	-	-

The deformed shapes of the FE models were used for contour plotting of the stress distribution. The stress was indicated by the contour lines. The regions of stress concentrations in each individual graft component were marked by black circles. Figure 4-7, Figure 4-8, Figure 4-10 and Figure 4-11show the contour plots of stress in the reinforced models at 200mmHg. Due to the large difference in the stress values among the components of the FE models, the components were seperated in these figures to provide each structure with its own contour legend. For the BG models the stress distrubution is shown at 120mmHg (Figure 4-9 and Figure 4-12).

The maximum stress in the wire mesh of model NIEX was predicted at the transverse portion of the individual wire loops and at the crossovers. The maximum stress in the PPU tube was predicted on its external surface.

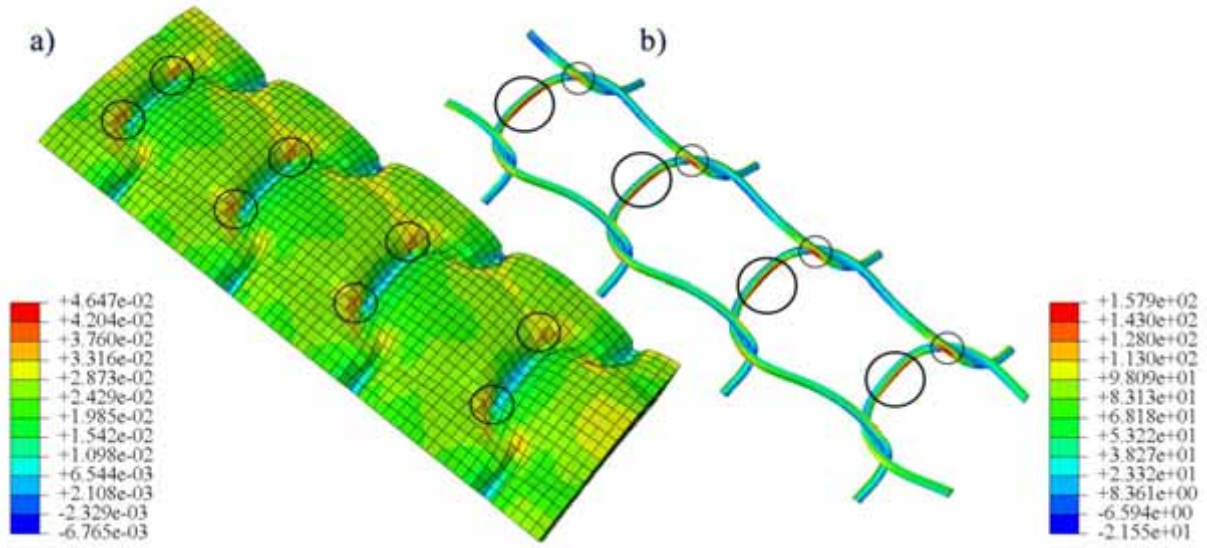

Figure 4-7: Contour plot of stress distribution in components of the NIEX model, at 200mmHg, indicating regions of maximum stress (black circles).

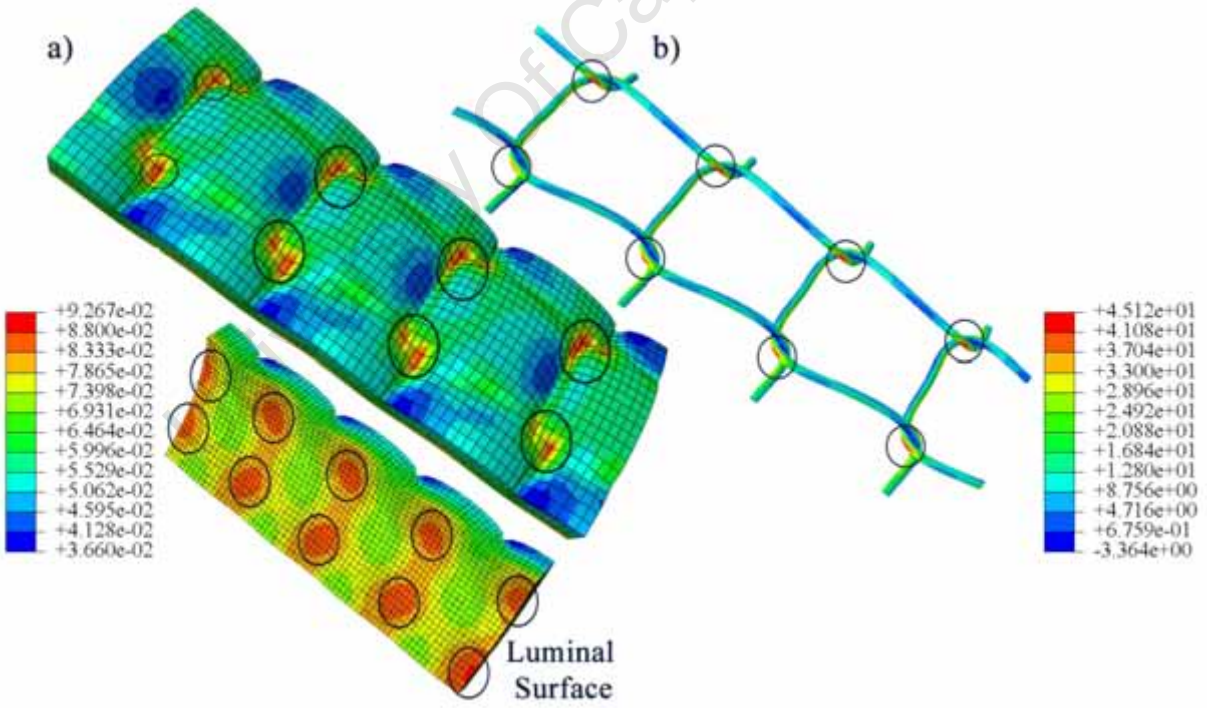

Figure 4-8: Contour plot of stress distribution in components of the PUEX model, at 200mmHg, indicating regions of maximum stress (black circles).

The PUEX model exhibited a different stress distribution. Concentrations of maximum stress were predicted on both the external and luminal surfaces of the PPU tube, and on the crossovers of the wire loops only.

On the BG2.4 model the stress increase was continuous through the wall of the PPU tube from the external to the internal surfaces.

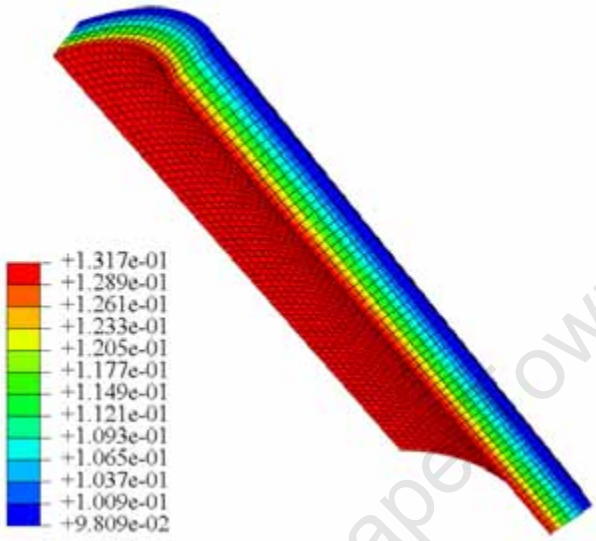

Figure 4-9: Contour plot of stress distribution in the BG2.4 model, at 120mmHg.

Although the two EM models exhibited similar locations of stress concentrations on the wire mesh, in Figure 4-10 (a) and Figure 4-11 (a), different stress distributions were noticed in the PPU tube. The maximum stress in the PPU tube of the EM models was predicted internally in the regions that surround the loops of the wire mesh. Three sections were created for the NIEM model (Figure 4-10 (b)) to reveal the areas of maximum stress. However, in the PUEM model (Figure 4-11 (b)) the maximum stress was predicted only in one section (i.e. section 1-1). The BG2.8 model showed similar stress distributions to the BG2.4 model.

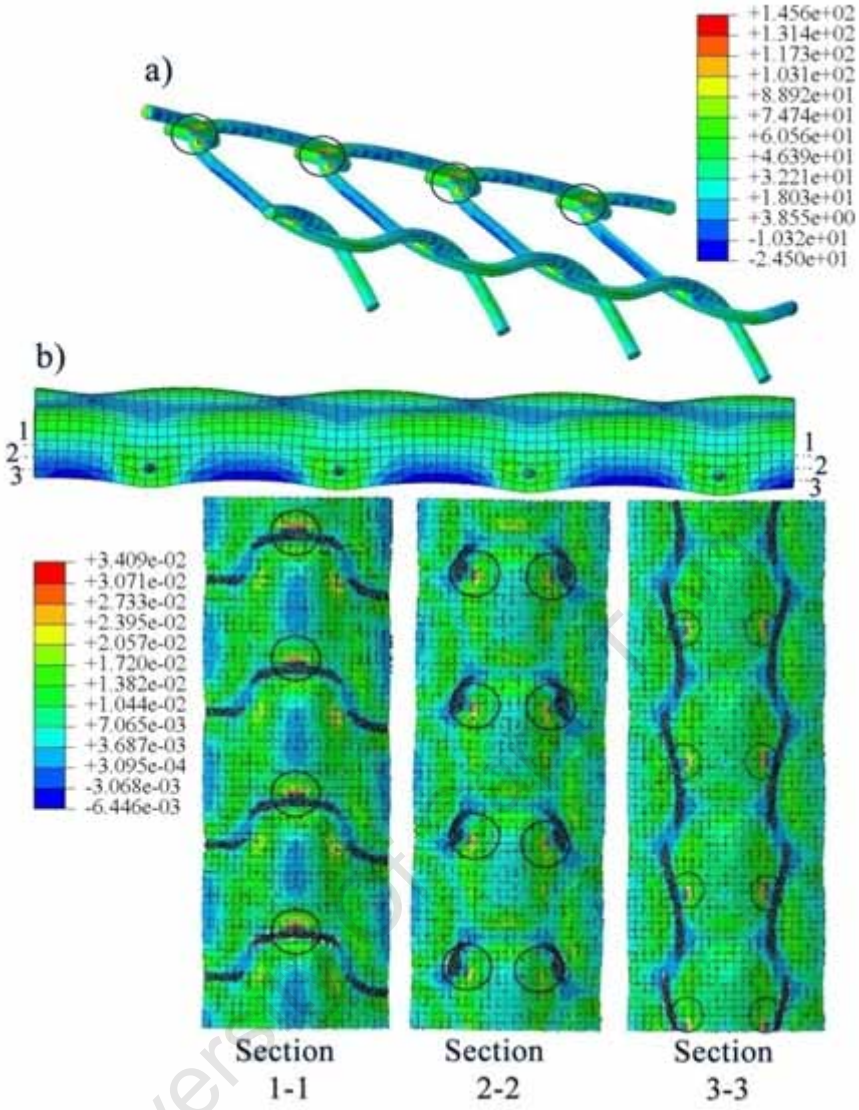

Figure 4-10: Contour plot of stress distribution in components of the NIEM model, at 200mmHg, indicating regions of maximum stress (black circles).

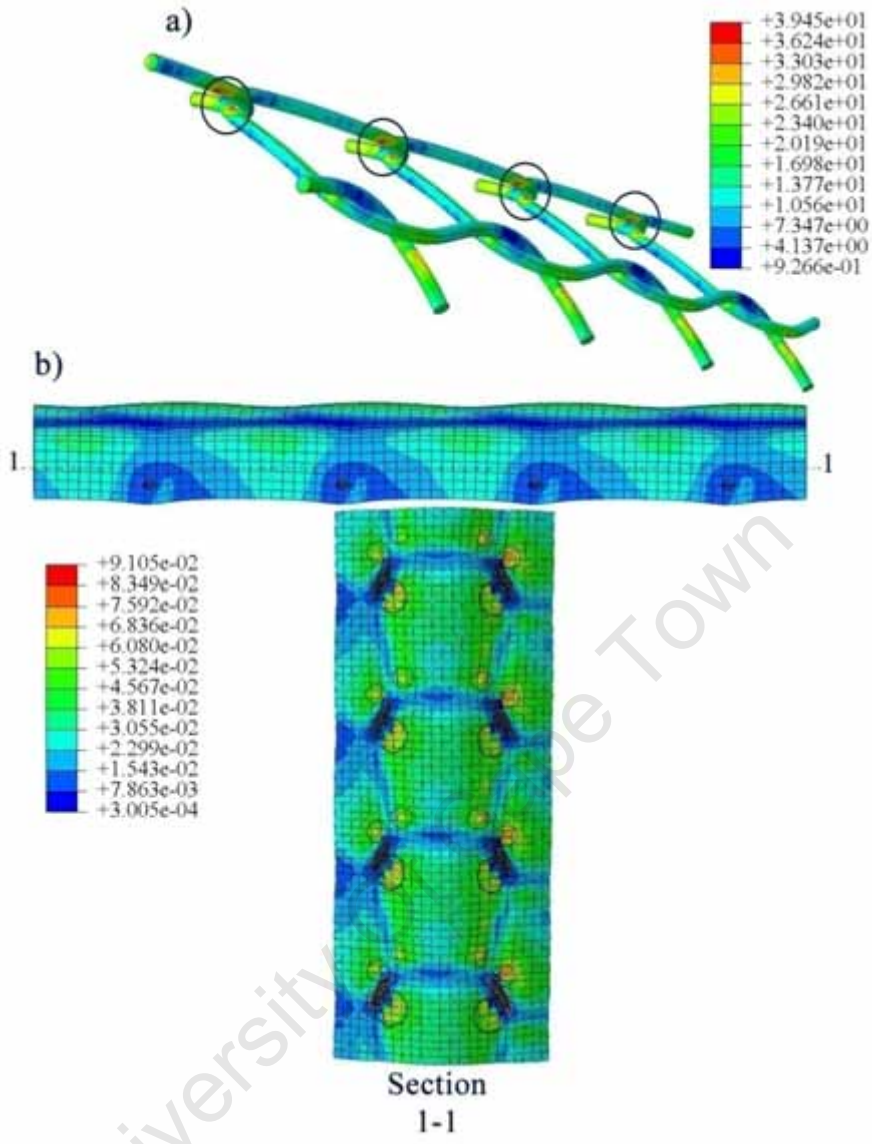

Figure 4-11: Contour plot of stress distribution in components of the PUEM model, at 200mmHg, indicating regions of maximum stress (black circles).

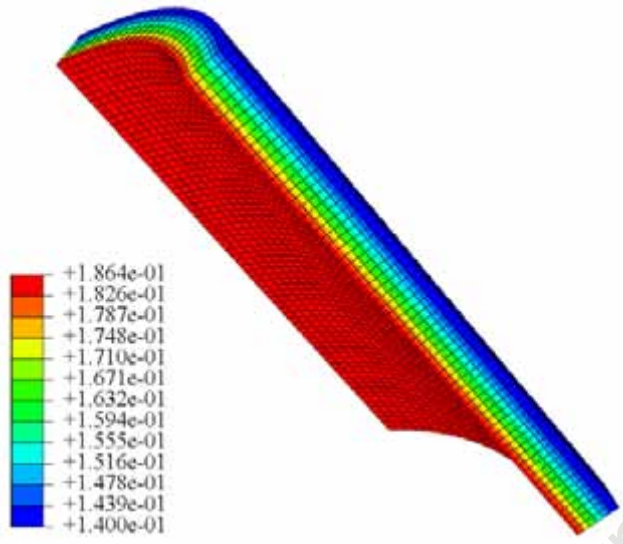

Figure 4-12: Contour plot of stress distribution in the BG2.8 model, at 120mmHg.

4.1.5.Maximum Principal Strain

The strain induced in the FE models due to pressure loads was recorded at each time increment of the analysis.

Table 4-4 illustrates the maximum principal strain predicted by individual components of the FE models at three pressure levels; the diastolic and systolic pressures, and 200mmHg. Less strain was predicted in the NITI wires than in the PU wires. The strain predicted by the BG models at 200mmHg was not available as the simulation terminated before reaching this pressure level. Both external and embedded reinforcement systems caused a reduction in the strain levels in the PPU tube at diastolic and systolic pressures compared to the BG models. Regardless of the reinforcement type, higher strain was predicted in the PPU tube when combined with PU wire mesh compared with the combination with the NITI wire mesh.

Table 4-4: Maximum principal strain in components of the FE models, at 80,120 and 200mmHg.

Model	Maximum Principal Strain (%)					
	80 mmHg		120 mmHg		200 mmHg	
	PPU tube	Wire mesh	PPU tube	Wire mesh	PPU tube	Wire mesh
NIEX	8.94	0.20	12.77	0.27	17.25	0.43
PUEX	15.63	3.33	21.87	4.93	31.17	7.92
BG2.4	27.53	-	50.28	-	-	-
NIEM	5.72	0.09	7.46	0.14	13.83	0.24
PUEM	16.15	2.94	22.40	4.33	32.54	6.92
BG2.8	33.41	-	68.47	-	-	-

Contour plots with black circles were used to illustrate the strain distribution and highlight the maximum strain in the FE models. Figure 4-13, Figure 4-14, Figure 4-16 and Figure 4-17 show the contour plots of strain for the reinforced models at 200mmHg. Due to the large difference in the strain values among the components of the FE models, the components were seperated in these figures to provide each structure with its own contour legend. For the BG models,in Figure 4-15 and Figure 4-18, the strain distrubution is shown at 120mmHg.

The maximum strain in the wire mesh of model NIEX was predicted at the transverse portion of the individual wire loops and at the crossovers. Regions of the maximum strain were predicted on the upper surface of the PPU tube in the NIEX model. The predicted regions of the strain concentration in the wire mesh and the PPU tube correlated with those of the stress concentration of model NIEX except for the strain concentration observed near the end of the tube (arrow).

The PUEX model exhibited concentrations of maximum strain on both the external and luminal surfaces of the PPU tube, and on the crossovers of the wire loops correlating with the stress concentration distribution of model PUEX.

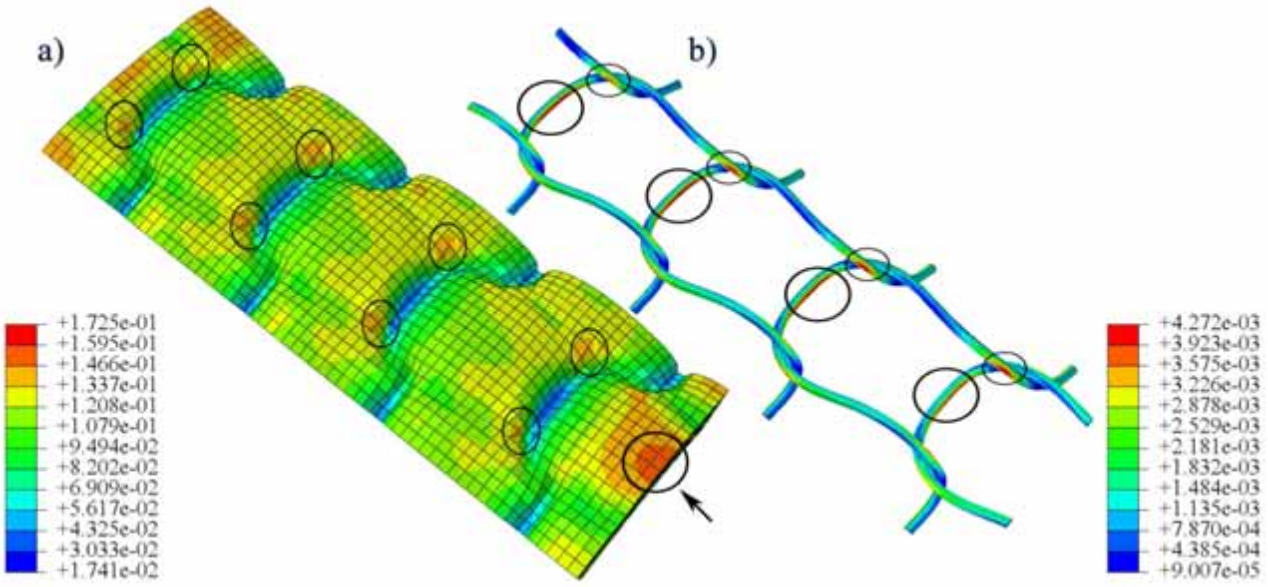

Figure 4-13: Contour plot of strain distribution in components of the NIEX model, at 200mmHg, indicating regions of maximum strain (black circles).

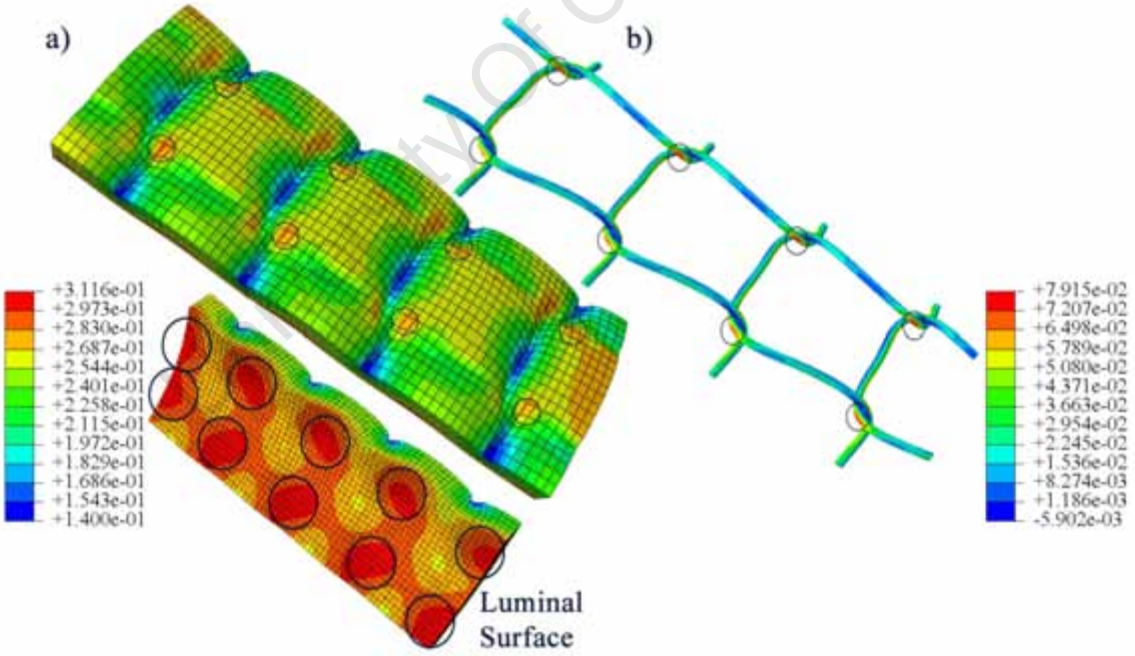

Figure 4-14: Contour plot of strain distribution in components of the PUEX model, at 200mmHg, indicating regions of maximum strain (black circles).

In the BG2.4 model a continuous increase in strain from the external to the internal surfaces was observed through the wall of the PPU tube correlating with the stress distribution of model BG2.4.

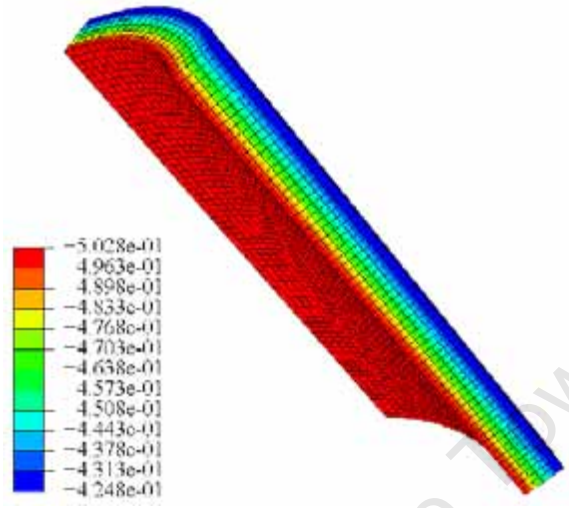

Figure 4-15: Contour plot of strain distribution in the BG2.4 model, at 120mmHg.

The maximum strain in the PPU tube of the EM models was predicted internally in the regions that surrounded the loops of the wire mesh. Three sections were made in the PPU tube of model NIEM, Figure 4-16 (a), to reveal these regions while one section was sufficient for the PPU tube of model PUEM (Figure 4-17 (a)). The wire meshes in both models, in Figure 4-16 (b) and Figure 4-17 (b), showed similar locations of strain concentrations. Similar to the stress distribution in the model, a continuous increase in strain from the internal to the external surfaces of the PPU tube was exhibited by the BG2.8 model (Figure 4-18).

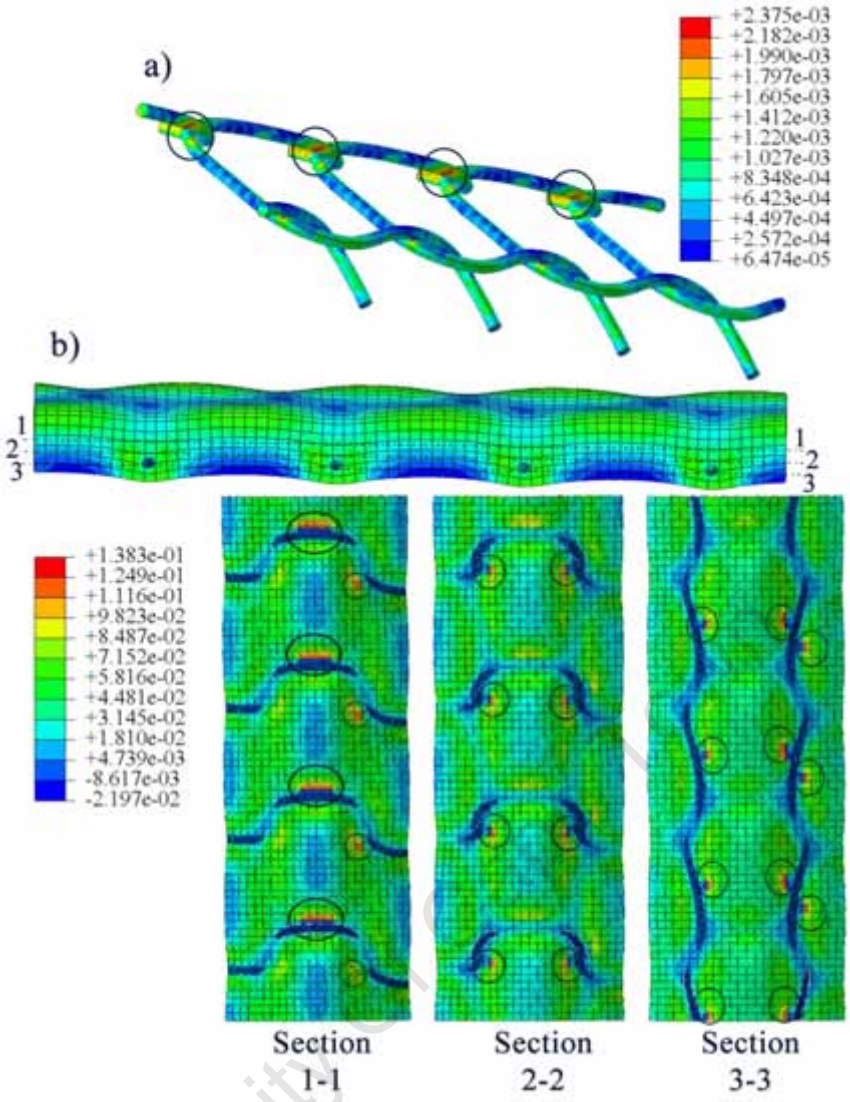

Figure 4-16: Contour plot of strain distribution in components of the NIEM model, at 200mmHg, indicating regions of maximum strain (black circles).

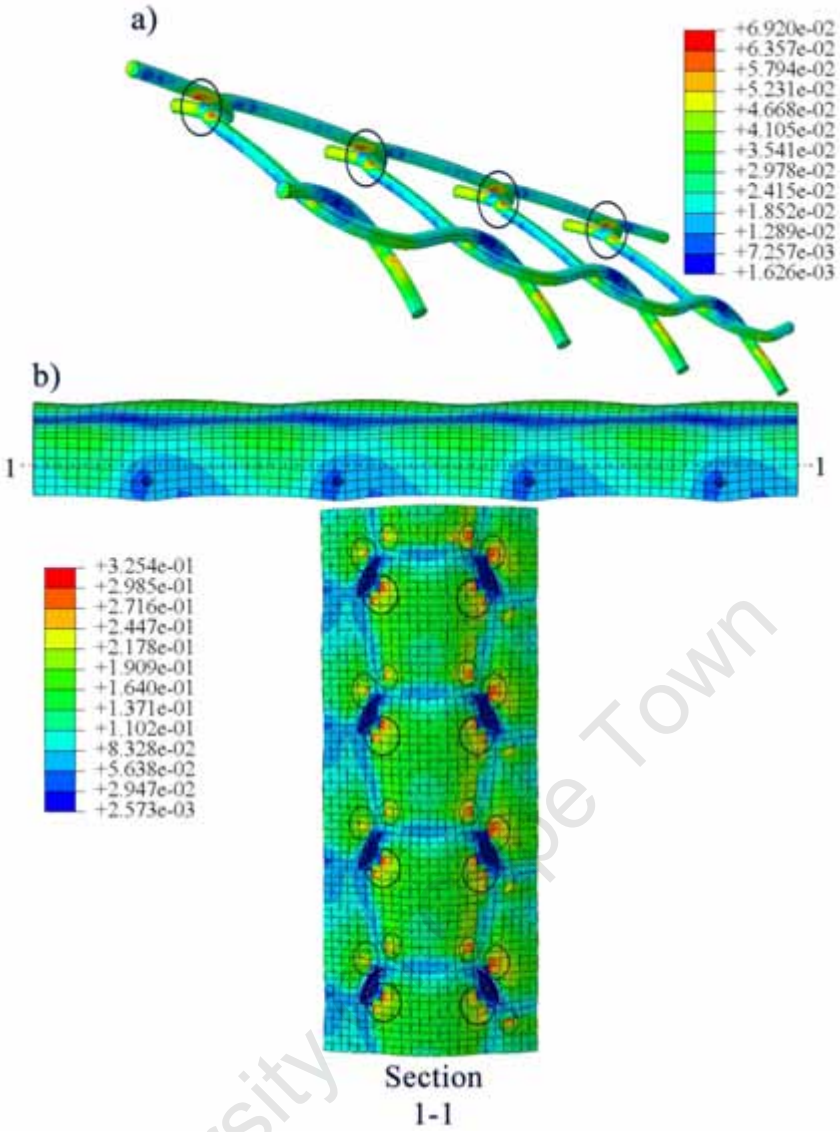

Figure 4-17: Contour plot of strain distribution in components of the PUEM model, at 200mmHg, indicating regions of maximum strain (black circles).

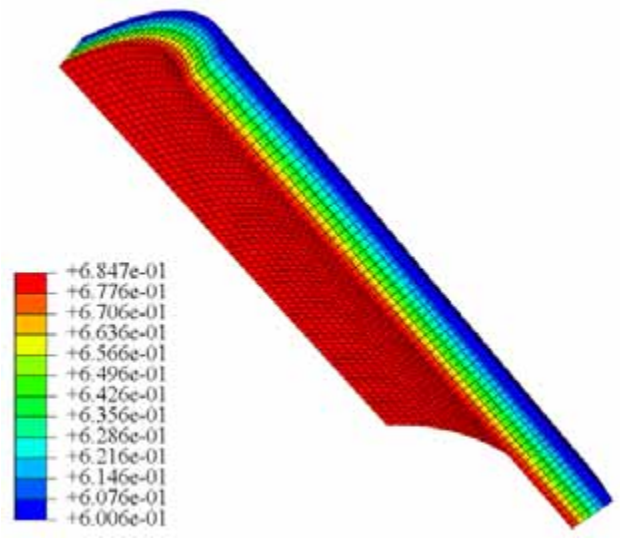

Figure 4-18: Contour plot of strain distribution in the BG2.8 model, at 120mmHg.

4.1.6.Martensite Fraction

The martensite fraction represented the percentage of martensite transformation undergone by the NITI wire mesh due to the induced stresses. The NITI wire mesh predicted 0% martensite fraction in the NIEX and NIEM models during the entire range of the applied pressure.

4.2.Finite Element Verification

The FE models underwent various verification tests as described in section 3.2. The following subsections highlight the outcomes of those verification tests.

4.2.1.Mesh Refinement Verification

The mesh density of the NIEX and PUEX models was altered, as illustrated in section 3.2.1, to evaluate the impact on the behaviour of the FE models. These models were compared to the models of coarser and finer meshes (i.e. NIEX-*coarse*, NIEX-*fine*, PUEX-*coarse* and PUEX-*fine*).

Model NIEX-*fine* and PUEX-*fine* terminated before completion of the simulation, particularly at a time increment equivalent to approximately 188mmHg.

Strain Energy

In Figure 4-19 and Figure 4-20 the strain energy was plotted versus the applied luminal pressure for the three versions of model NIEX and PUEX, respectively.

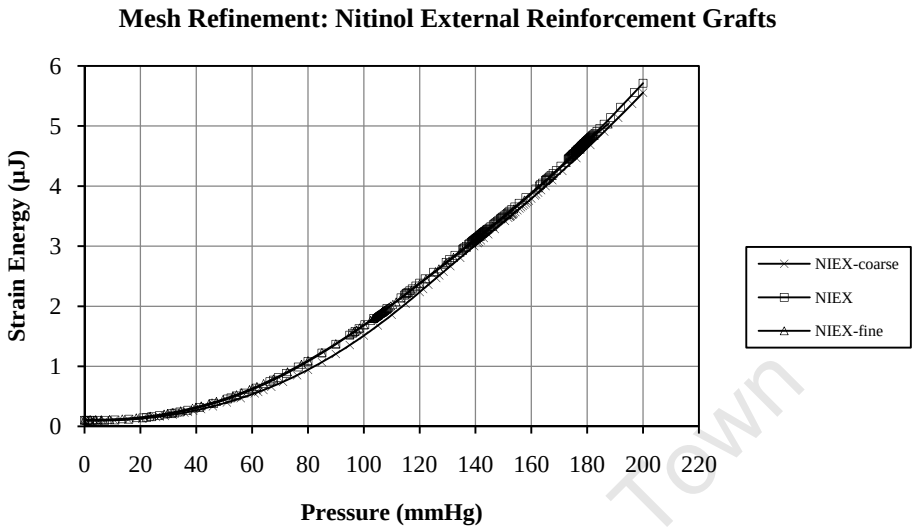

Figure 4-19: Strain energy versus luminal pressure for mesh-refined versions of the NIEX model.

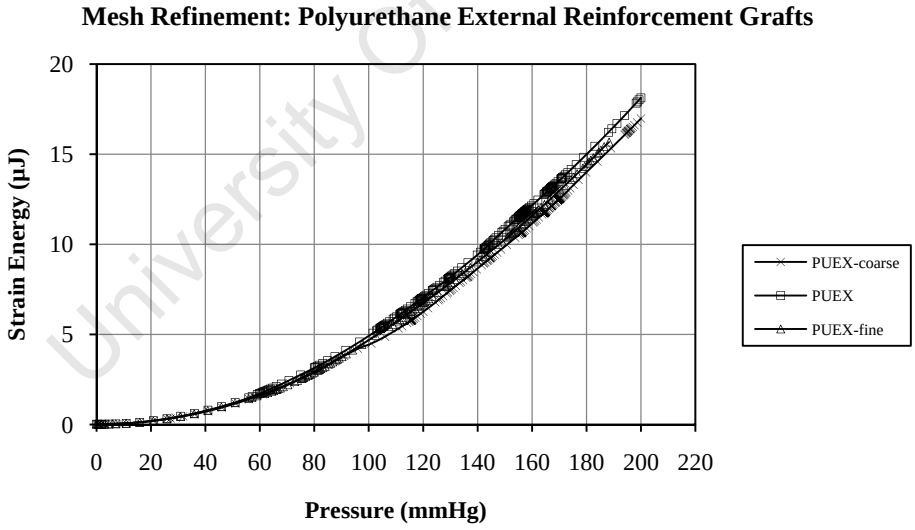

Figure 4-20: Strain energy versus luminal pressure for mesh-refined versions of the PUEX model.

The strain energy curves of all the three versions of model NIEX showed an exponential increase. The curves of the NIEX and NIEX-*fine* models were similar to each other and slightly higher than the NIEX-*coarse* model.

The three versions of the PUEX model showed closely correlating curves at lower pressure levels. Slightly before 100mmHg, the curve of the PUEX-*coarse* model exhibited a slight deflection. The other two models maintained their increase recording slightly higher levels of strain energy than the PUEX-*coarse* model.

Pressure-Diameter Relationship and Compliance

The pressure-diameter relationship was assessed for the different versions of the NIEX and PUEX models. The luminal pressure was plotted versus the increase in the inner diameter expressed as relative change to initial inner diameter for the different versions of the NIEX and PUEX models in Figure 4-21 and Figure 4-22 respectively.

The curves of the three NIEX versions slightly differed from each other. As they started to dilate, the NIEX and NIEX-*fine* models showed similar curves with slightly higher levels of increase in the inner diameter than the NIEX-*coarse* model. At higher pressure levels, the NIEX-*fine* model diverged from the NIEX model to match the NIEX-*coarse* model.

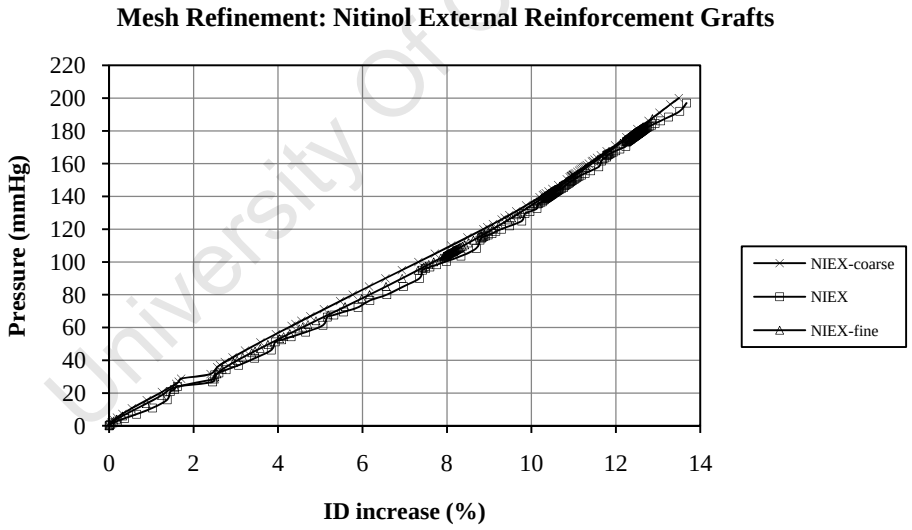

Figure 4-21: Radial deformation of mesh-refined versions of the NIEX model expressed as luminal pressure versus inner diameter increase.

The three PUEX versions showed similar curves up to approximately 50mmHg, after which slight differences were observed. Slightly before 100mmHg, the curve of the NIEX-*coarse* model exhibited a similar deflection to that seen with the strain energy curve. The other two models maintained their trends.

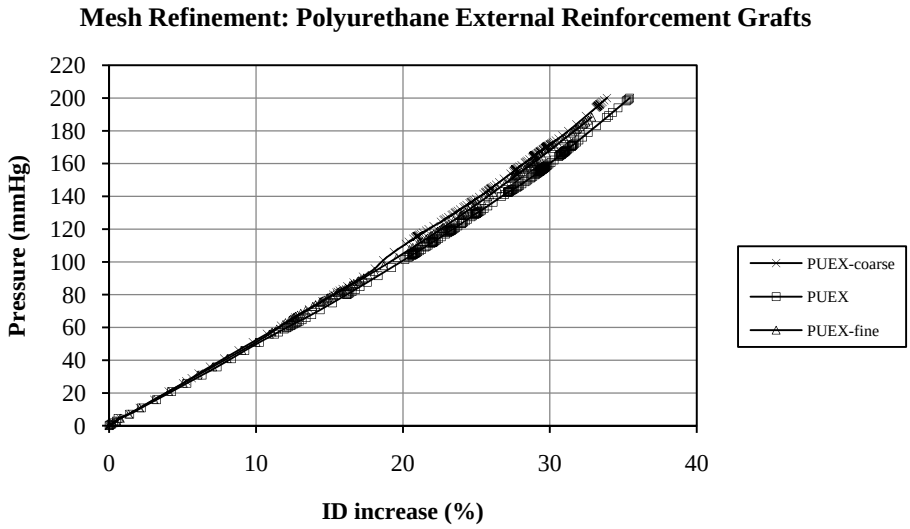

Figure 4-22: Radial deformation of mesh-refined versions of the PUEX model expressed as luminal pressure versus inner diameter increase.

The radial compliance of the different models was calculated between 80 and 120mmHg and summarized in Table 4-5.

The three models in each set showed close values. The difference in compliance found between the NIEX and NIEX-*fine* model was less than that between the NIEX and NIEX-*coarse* model. Similarly, a smaller difference was found between the PUEX and PUEX-*fine* model compared to the difference between PUEX and the PUEX-*coarse* model.

Table 4-5: Radial compliance for the mesh-refined models, calculated between 80 and 120mmHg.

Model	Compliance (%/100mmHg)
NIEX-coarse	7.31
NIEX	7.02
NIEX-fine	6.93
PUEX-coarse	14.10
PUEX	15.57
PUEX-fine	15.86

Maximum Principal Stress

Table 4-6 summarizes the maximum principal stress predicted by the different models at diastolic and systolic pressures. Close values of maximum stress were predicted among the versions of model NIEX and PUEX, both for the PPU tube and the wire mesh. Differences in stress were smaller between the standard and the fine models compared to differences between the standard and the coarse models.

Table 4-6: Maximum principal stress in components of the mesh-refined models, at 80 and120mmHg.

Model	Maximum Principal Stress (MPa)			
	80 mmHg		120 mmHg	
	PPU tube	Wire mesh	PPU tube	Wire mesh
NIEX-coarse	0.018	70.08	0.028	94.30
NIEX	0.020	73.68	0.031	97.0
NIEX-fine	0.020	77.75	0.031	96.69
PUEX-coarse	0.032	21.66	0.048	30.86
PUEX	0.036	18.98	0.055	28.08
PUEX-fine	0.035	19.0	0.053	21.29

Maximum Principal Strain

Table 4-7 summarizes the predicted maximum principal strain for the different models at diastolic and systolic pressures. Similar to the stress, the differences in the strain values, in the PPU tube and the wire mesh, were smaller between the standard and the fine models compared to those between the standard and the coarse models.

Table 4-7: Maximum principal strain in components of the mesh-refined models, at 80,120 and 200mmHg.

Model	Maximum Principal Strain (%)			
	80 mmHg		120 mmHg	
	PPU tube	Wire mesh	PPU tube	Wire mesh
NIEX-coarse	8.68	0.19	13.10	0.26
NIEX	8.94	0.20	12.77	0.27
NIEX-fine	8.99	0.21	12.71	0.26
PUEX-coarse	14.02	3.8	19.29	5.41
PUEX	15.63	3.33	21.87	4.93
PUEX-fine	14.95	3.33	21.29	5.0

4.2.2.Element Type Verification

The NIEX and PUEX models underwent element type verification by regenerating the FE mesh using 10-node quadratic tetrahedral elements, resulting in new versions; NIEX-TET and PUEX-TET, as introduced in section 3.2.2. The intended strategy of running NIEX-TET and PUEX-TET models and then generating models from them with a lower mesh density was inapplicable. Both models experienced numerical problems illustrated by the early termination of the simulation due to convergence errors. Several attempts were made to get a stable numerical behaviour of NIEX-TET and PUEX-TET by adjusting the contact and stabilisation parameters. After 27 attempts, convergence was still unachievable. The following shows the best obtained result.

Both of the newly developed models, NIEX-TET and PUEX-TET, failed to complete the simulation. Model NIEX-TET terminated at 97mmHg, while model PUEX-TET terminated at 102mmHg. The strain energy configuration and the pressure-diameter relationship of the different models were compared.

Strain Energy

The strain energy was plotted versus the luminal pressure for the NIEX and NIEX-TET, in Figure 4-23, and for the PUEX and PUEX-TET, in Figure 4-24.

The NIEX-TET had a similar trend to the NIEX model at low pressure levels. Shortly after exceeding 60mmHg, the NIEX-TET exhibited smaller increase of strain energy with

the increasing pressure and terminated at 97mmHg. The PUEX-TET exhibited similar trend to the PUEX model until it terminated at 102mmHg.

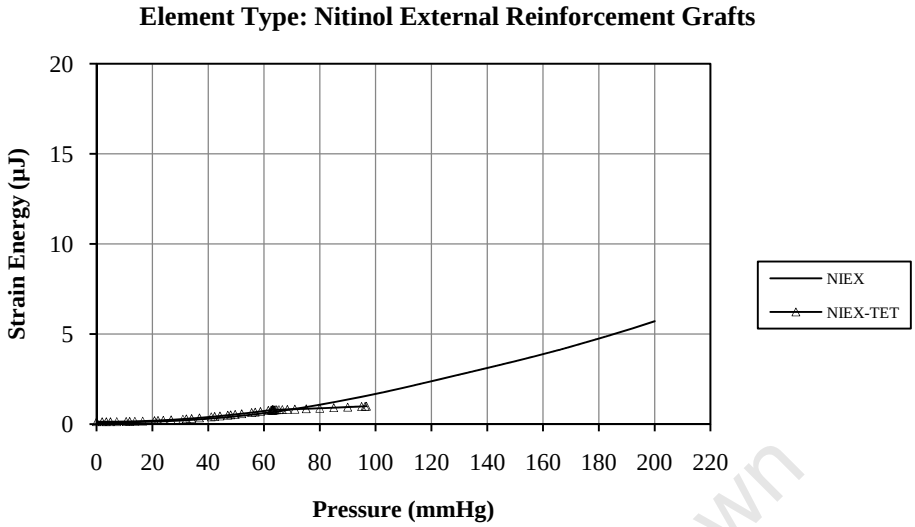

Figure 4-23: Strain energy versus luminal pressure for the NIEX model and its equivalent model with tetrahedral element.

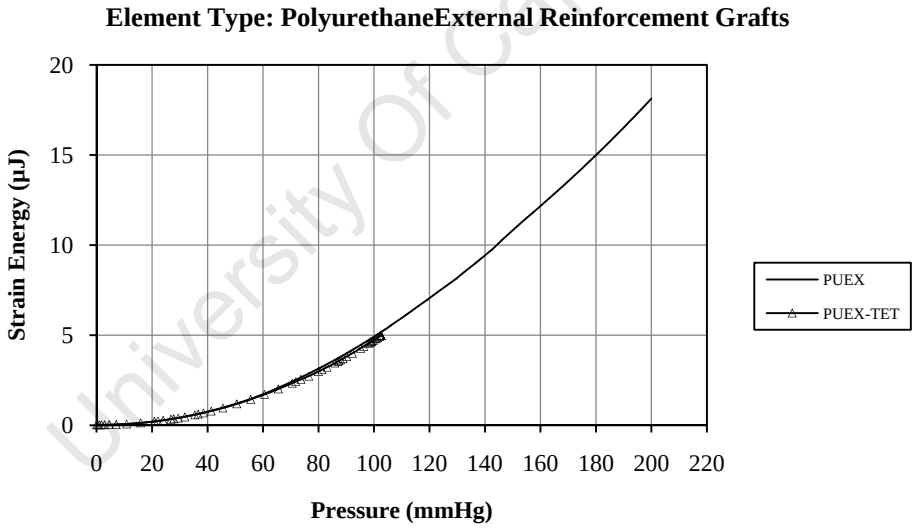

Figure 4-24: Strain energy versus luminal pressure for the PUEX model and its equivalent model with tetrahedral element.

Pressure-Diameter Relationship

The luminal pressure was plotted versus the increase in the inner diameter expressed as relative change to initial inner diameter for model NIEX and NIEX-TET, in Figure 4-25, and model PUEX and PUEX-TET, in Figure 4-26. The dilation of the NIEX-TET model followed that of model NIEX and deflected shortly after 60mmHg towards a smaller dilation with the increasing pressure before it terminated at 97mmHg. The PUEX-TET

model showed similar trend to PUEX model with a slightly lower dilation with increasing pressure, and terminated at 100mmHg.

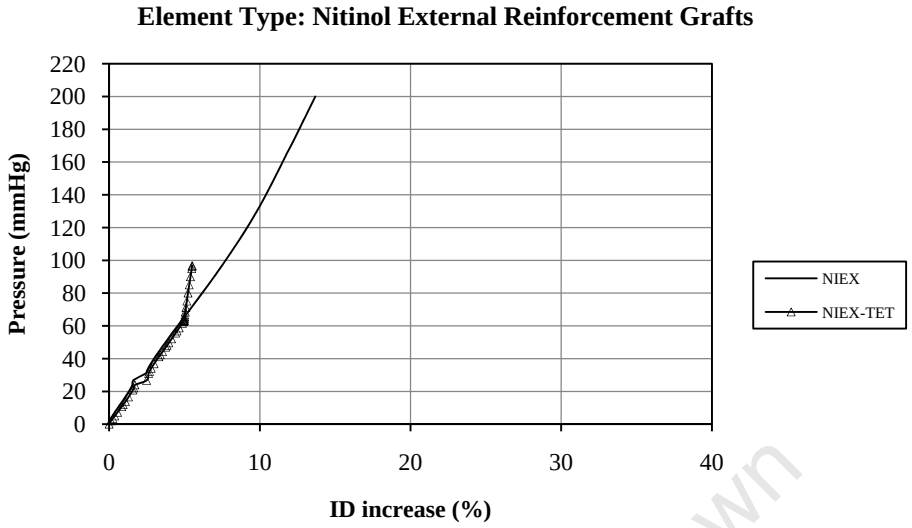

Figure 4-25: Radial deformation of the NIEX model and its equivalent model with tetrahedral element expressed as luminal pressure versus inner diameter increase.

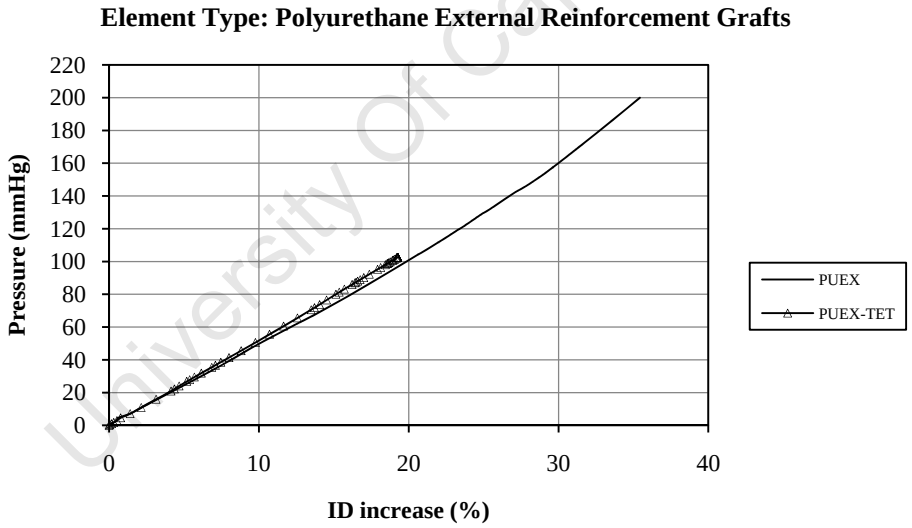

Figure 4-26: Radial deformation of the PUEX model and its equivalent model with tetrahedral element expressed as luminal pressure versus inner diameter increase.

4.2.3.Boundary Condition Verification

The NIEX-BCV model was developed from the NIEX by replacing the circumferential BC assigned to the PPU tube by a cyclic symmetry interaction as described in section 3.2.3. The two models were compared in terms of strain energy, compliance, and maximum stress and strain. The plots of the pressure-diameter relationship were not

presented as the information on the displacement for the NIEX-BCV model could not be obtained.

Strain Energy

In Figure 4-27, the strain energy was plotted versus the luminal pressure to compare the NIEX model to the NIEX-BCV model. Similarity between the two curves was seen for the whole range of pressure.

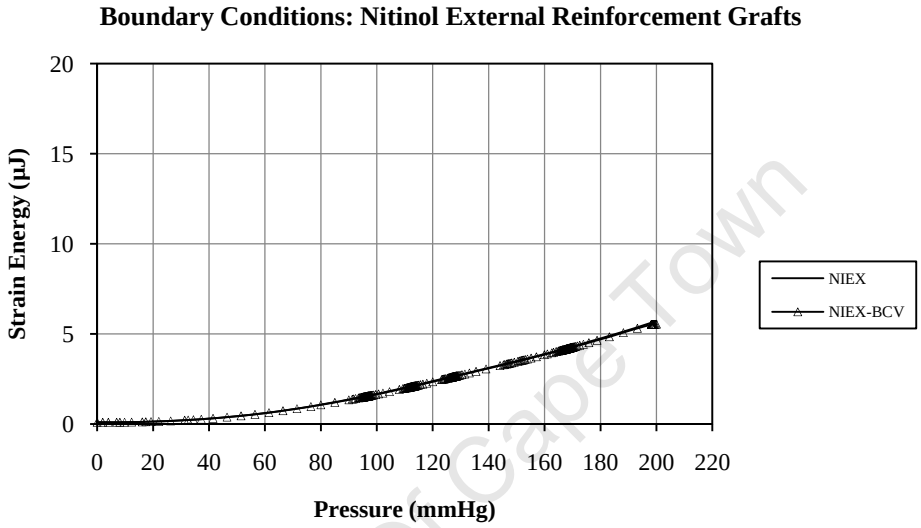

Figure 4-27: Strain energy versus luminal pressure for the NIEX model and its equivalent model with cyclic symmetry interaction.

Compliance

The radial compliance, Table 4-8, of model NIEX and NIEX-BCV was obtained based on the displacement information of the set of nodes predefined on both models (see Figure *3-14*). The calculated compliance values of the two models were found to be very close to each other.

Table 4-8: Radial compliance for the NIEX model and its equivalent model with cyclic symmetry interaction, calculated between 80 and 120mmHg.

Model	Compliance (%/100mmHg)
NIEX	6.98
NIEX-BCV	6.91

Maximum Principal Stress

The maximum stress predicted in both components (i.e. PPU tube and wire mesh) of the NIEX and NIEX-BCV models, at diastolic and systolic pressures, was compared in Table 4-9. The predicted values were found to be comparable for both structures of the models.

Table 4-9: Maximum principal stress in components of the NIEX model and its equivalent model with cyclic symmetry interaction, at 80 and 120mmHg.

Model	Maximum Principal Stress (MPa)			
	80 mmHg		120 mmHg	
	PPU tube	Wire mesh	PPU tube	Wire mesh
NIEX	0.020	73.68	0.031	97.0
NIEX-BCV	0.019	74.57	0.030	97.52

Maximum Principal Strain

In Table 4-10, the predicted maximum strain was compared in both components of the NIEX and NIEX-BCV models at diastolic and systolic pressures. The predicted values were found to be comparable for both structures of the models.

Table 4-10: Maximum principal strain in components of the NIEX model and its equivalent model with cyclic symmetry interaction, at 80 and 120mmHg.

Model	Maximum Principal Strain (%)			
	80 mmHg		120 mmHg	
	PPU tube	Wire mesh	PPU tube	Wire mesh
NIEX	8.94	0.20	12.77	0.27
NIEX-BCV	8.64	0.20	12.51	0.27

4.2.4.Contact Definition Verification

Two versions of model NIEX, namely NIEX-CV1 and NIEX-CV2, were compared to the standard version (i.e. model NIEX) to verify the contact definition as mentioned in section 3.2.4. The NIEX-CV1 model did not complete the simulation, terminating when the luminal pressure reached 104mmHg. The models were compared in terms of strain energy and pressure-diameter relationship.

Strain Energy

Figure 4-28 illustrates the strain energy versus the applied luminal pressure for model NIEX, NIEX-CV1 and NIEX-CV2. The models showed the same initial trend. Model NIEX-CV2 overcame the termination of model NIEX-CV1, but experienced a deflection towards a smaller increase in the strain energy with increasing pressure shortly after exceeding 170mmHg.

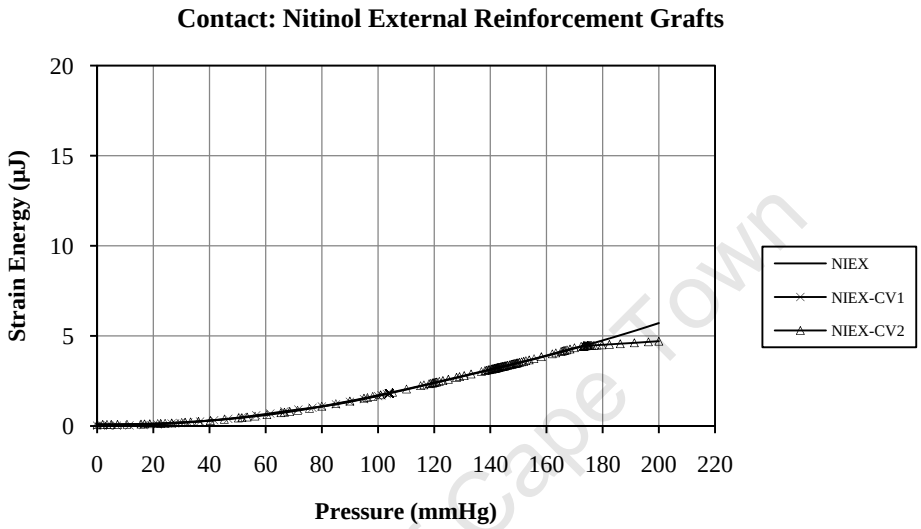

Figure 4-28: Strain energy versus luminal pressure for the NIEX model and its equivalent models with different contact definitions.

Pressure-Diameter Relationship

In Figure 4-29, the luminal pressure was plotted versus the change in the inner diameter expressed as relative change to initial inner diameter for model NIEX, NIEX-CV1 and NIEX-CV2. The NIEX-CV2 and NIEX models exhibited similar trend and lower increase in the inner diameter than version NIEX-CV1. The deflection of the curve of model NIEX-CV2 agreed with that observed for the strain energy curve with respect to the pressure.

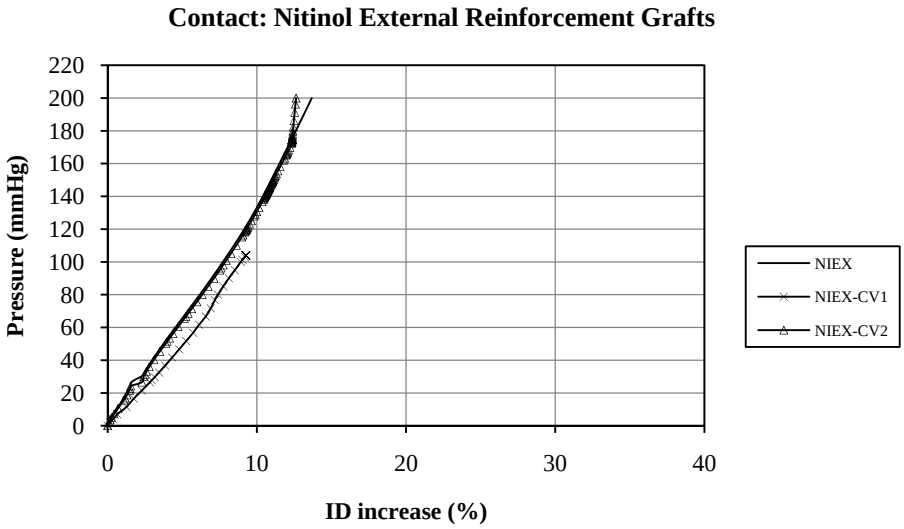

Figure 4-29: Radial deformation of the NIEX model and its equivalent models with different contact definitions expressed as luminal pressure versus inner diameter increase.

4.2.5.Friction Verification

The sensitivity of the models to the frictional tangential contact was assessed by comparing the NIEX and NIEM models to newly developed versions with frictionless contact, NIEX-FL and NIEM-FL, respectively, as described in section 3.2.5. The comparison included strain energy, pressure-diameter relationship, compliance, and maximum principal stress and strain. The NIEX-FL model terminated before the simulation completed, at a pressure of 186mmHg.

Strain Energy

The strain energy was plotted versus the luminal pressure for models NIEX and NIEX-FL, in Figure 4-30, and for NIEM and NIEM-FL, in Figure 4-31.

The NIEX-FL model exhibited a similar trend to the NIEX model but with higher strain energy values. The curve of model NIEX-FL diverged from that of model NIEX as the pressure increased. The strain energy curves of models NIEM and NIEM-FL were found to be identical.

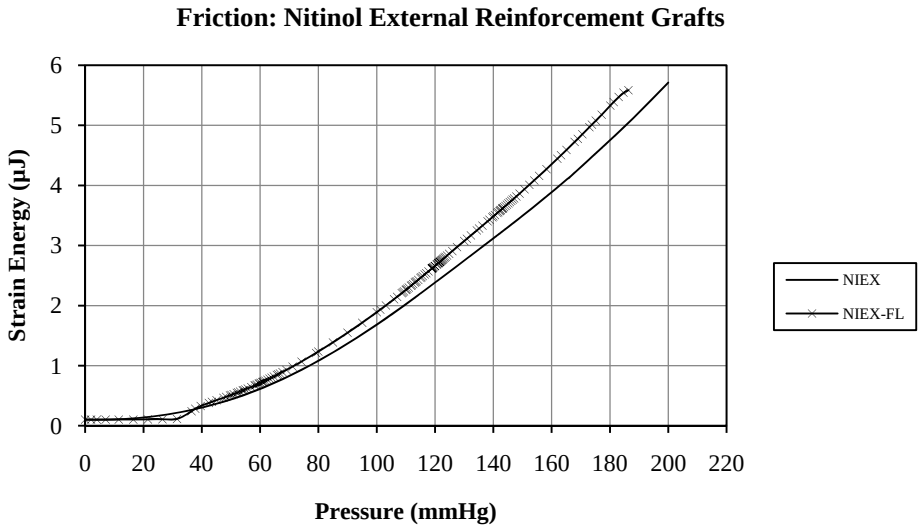

Figure 4-30: Strain energy versus luminal pressure for the NIEX model and its equivalent model with frictionless contact.

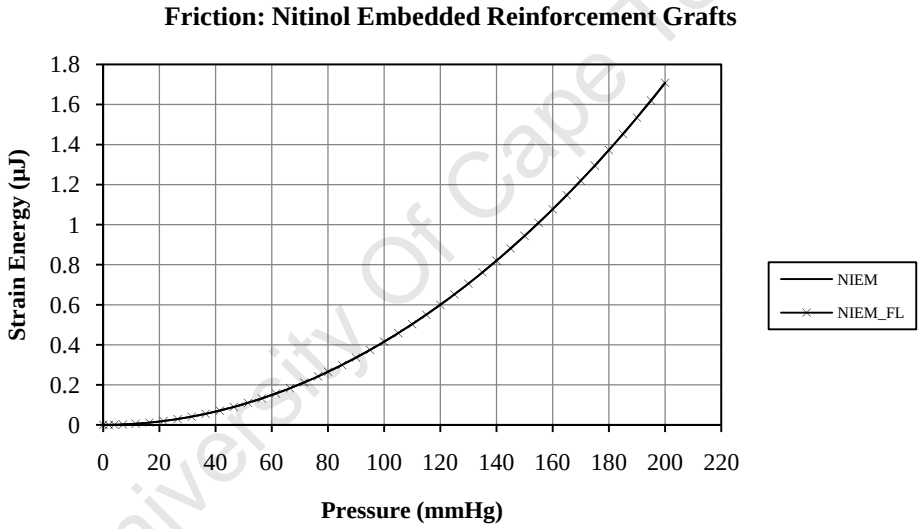

Figure 4-31: Strain energy versus luminal pressure for the NIEM model and its equivalent model with frictionless contact.

Pressure-Diameter Relationship and Compliance

The luminal pressure was plotted versus the increase in the diameter expressed as relative change to initial inner diameter for model NIEX and NIEX-FL, in Figure 4-32, and for model NIEM and NIEM-Fl, in Figure 4-33.

The NIEX-FL model exhibited a sigmoidal curve. It initially experienced smaller dilation compared to the NIEX model. As the pressure exceeds 30mmHg, model NIEX-FL experienced a sudden dilation with hardly increase in the pressure. As the pressure exceeded 40mmHG, the dilation slope reduced and continued with the increasing

pressure. The dilation of model NIEX-FL, as the pressure increasing beyond 40mmHg, was larger than that of the NIEX model although the trend of dilation was similar. On the other hand, identical dilation was observed for model NIEM and NIEM-FL.

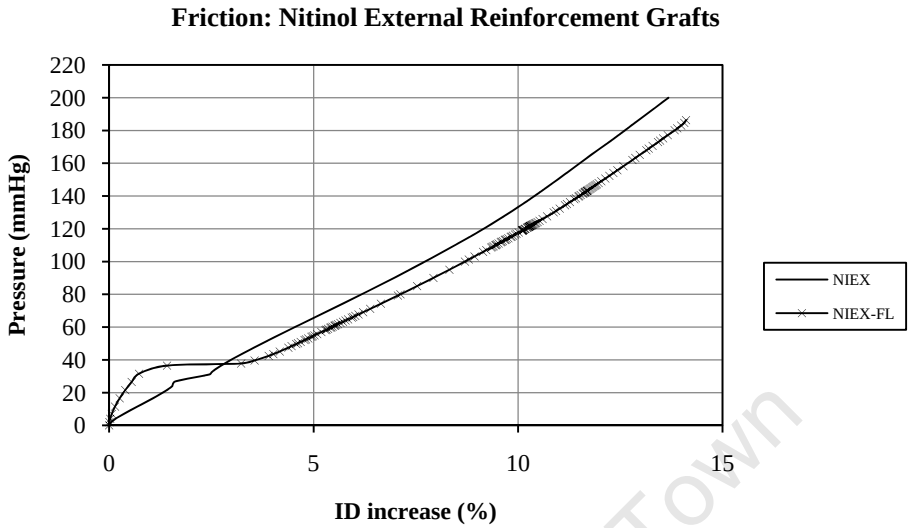

Figure 4-32: Radial deformation of the NIEX model and its equivalent model with frictionless contact expressed as luminal pressure versus inner diameter increase.

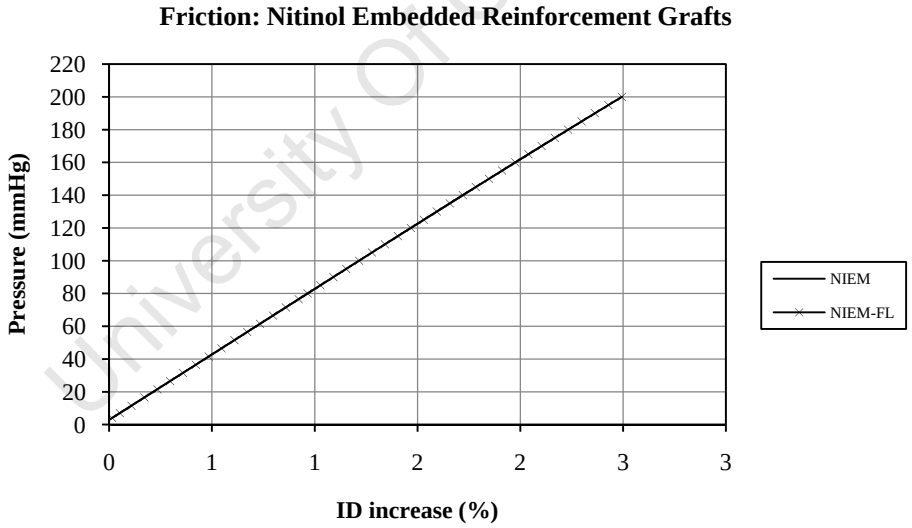

Figure 4-33: Radial deformation of the NIEM model and its equivalent model with frictionless contact expressed as luminal pressure versus inner diameter increase.

The radial compliance calculated for the different models is illustrated in Table 4-11. The NIEX-FL model predicted a slightly higher compliance than the NIEX model, while equal compliance values were observed for the NIEM and the NIEM-FL models.

Table 4-11: Radial compliance for the NIEX and NIEM models and their equivalent models with frictionless contact, calculated between 80 and 120mmHg.

Model	Compliance (%/100mmHg)
NIEX	7.02
NIEX-FL	7.13
NIEM	1.24
NIEM-FL	1.24

Maximum Principal Stress

Table 4-12 compares the maximum principal stress predicted in the components of the different models at 80 and 120mmHg. The NIEX-FL model predicted higher stress values than the NIEX model except for the wire mesh at 80mmHg. The NIEM and NIEM-FL models showed equal values in both PPU tube and wire mesh at both pressure values.

Table 4-12: Maximum principal stress in components of the NIEX and NIEM models and their equivalent models with frictionless contact, at 80 and 120mmHg.

Model	Maximum Principal Stress (MPa)			
	80 mmHg		120 mmHg	
	PPU tube	Wire mesh	PPU tube	Wire mesh
NIEX	0.020	73.68	0.031	97.0
NIEX-FL	0.023	72.65	0.034	105.6
NIEM	0.012	57.59	0.019	86.72
NIEM-FL	0.012	57.61	0.019	86.77

Maximum Principal Strain

Table 4-13 compares the maximum principal strain predicted in the components of the different models at 80 and 120mmHg. The NIEX-FL model predicted higher strain values than the NIEX model except for the wire mesh at 80mmHg. The NIEM and NIEM-FL models exhibited equal values except for the PPU tube at 120mmHg.

Table 4-13: Maximum principal strain components of the NIEX and NIEM models and their equivalent models with frictionless contact, at 80 and 120mmHg.

Model	Maximum Principal Stain (%)			
	80 mmHg		120 mmHg	
	PPU tube	Wire mesh	PPU tube	Wire mesh
NIEX	8.94	0.20	12.77	0.27
NIEX-FL	10.13	0.20	13.97	0.29
NIEM	5.72	0.09	7.46	0.14
NIEM-FL	5.72	0.09	8.46	0.14

5. Discussion

In this study, the FEM was used to investigate the mechanical design of multi-component tissue-regenerative vascular grafts. These grafts comprised a tubular PPU structure as a scaffold for tissue ingrowth and regeneration and a knitted wire mesh as structural reinforcement utilising NITI and solid PU, respectively. Six models were developed representing external and embedded reinforcement of the PPU tube, as introduced in section 3.1. The NIEX and PUEX models represented the external reinforced version of the bare graft model BG2.4, while the NIEM and PUEM models represented the embedded reinforcement version of the bare graft model BG2.8. The structural and mechanical behaviour of the grafts was predicted using the FE models when subjected to a luminal pressure ramping from 0 to 200mmHg. Additional analyses were performed to assess and verify the FE models, section 3.2. The predicted mechanics of the FE models as well as the outcomes of the verification tests were presented in Chapter 4. In this chapter, the different aspects of model development are presented for the standard FE models and those developed for verification purposes. Thereafter, the results of the verification and validation of the FE models are discussed followed by the comparison of the results of the various graft designs.

5.1. Development of the Finite Element Models

The geometry of the wire mesh was created circumferentially as a one-eighth circumferential section of the 3D eight-loops knitted tubular centreline structure. Longitudinally, the number of the loops in the 45º model had to be compromised. The more the incorporated loops in the model the better the representation would be, however, the more the computational expense would be expected. Three complete loops were decided to be included in the assembly with the two partial loops at the ends to correlate with the assembly used in the studies (van der Merwe 2007; van der Merwe et al. 2008). The wire mesh structure was not completely symmetric as the knitted pattern of the loops exhibited an overall helical orientation. However, the symmetric BC was later applied utilizing the repetitive pattern in both longitudinal and circumferential directions.

Modelling of the PPU tube at macroscopic level was assumed to be sufficient to serve the objectives of this research. The EX and EM geometries were developed by varying the inner diameter of the tube and preserving its wall thickness (see Figure 3-4). It was more

feasible to modify the tube structure than remodelling the whole wire mesh geometry with new inner diameter. Moreover, this approach was thought to give wider conception of design optimisation by providing grafts with different inner diameters. However, the different inner diameter of the EX and EM assemblies reduced the possible range of cross-comparison between the models of different reinforcement systems.

The study involved three material models; a hyperfoam material model for the PPU, a user-material for superelasticity of the SMA and a linear elastic material model for the solid PU. In previous studies (Yeoman 2004; Yeoman et al. 2009), hyperfoam material models were developed for PPU of three different pores sizes (90-160 ,106-125, and 125-150 μm). The material model of the largest pores (i.e. 125-150 μm) was chosen for this study. Without affecting the neo-vascularisation, it was found that increasing the pores size considerably reduces the inflammatory response (Bezuidenhout et al. 2002). The knitted NITI wire mesh showed considerable outcomes when utilized as supporting structure to vein grafts (Zilla et al. 2008; Human et al. 2009; Zilla et al. 2009). In this study, this structure was utilized for reinforcement of tissue-regenerating vascular grafts. In order to allow for comparison and assessment of the feasibility of using the same wire geometry with another material, a generic PU material was utilised in this study, which might provide suggestions for the optimisation of the graft mechanics.

The choice of the linear brick elements for the FE models was based on the poor performance observed by the tetrahedral elements in the verification tests, as will be discussed later. The PPU tube and the wire mesh were meshed separately and independently due to the large difference in their dimensions, e.g. the wall thickness of the PPU tube compared to the wire thickness of the reinforcing mesh. Although the same meshing technique, including element type and size, was applied for the EX and EM assemblies, the number of nodes and elements was different (Table 3-4 and Table 3-5). The EM models possessed more elements and nodes than the EX models. When using the embedded region constraint (Abaqus 2008), the volume of the embedded structure (i.e. the wire mesh) was subtracted from the volume of the host structure (i.e. the PPU tube) which reduced the total number of elements. Accordingly the number of elements in the EM models was expected to be less than that of the EX models. However, the PPU tube in the EM models had larger inner diameter than that in the EX models, while both had the same wall thickness. Therefore, the volume of the PPU tube was greater in the EM models, and so was the number of elements and nodes (Table 3-6).

The analyses were carried out in two subsequent steps. The first step was essential for establishment of contact between the various parts of the models. Since the contact pairs were based on surfaces and not nodes, the appropriate contact elements were generated automatically based on the predefined master-slave relationship and initial adjustments were performed to achieve the pressure-clearance settings (Abaqus 2008). A limitation of such contact establishment appeared to be the decreasing initial inner diameter of the PPU tube in the NIEX and PUEX models below the intended value of 2.4mm (section 4.1.2).

The numerical stability of the FE models was assessed using the smoothness (i.e. absence of discontinuity in slope) of the predicted strain energy curve when plotted versus the applied luminal pressure. Initially, the pronounced change in the slope of the strain energy curve was thought to be due to a physical condition such as excessive dilation. In further trials, changing the contact and stabilization settings had a considerable influence on the smoothness of the strain energy curve. Hence, any discontinuity in the slope of the strain energy curve was attributed to numerical instability of the models and treated with adjusting the contact and stabilization settings.

5.2.Verification and Validation of the Finite Element Models

Different versions of the original FE models were developed for the purpose of verifying the mesh density, the BC, the contact, and the friction. In the following sections, the outcomes of these verification tests will be discussed. In addition, the standard FE models will be compared to experimental compliance values obtained in other studies.

5.2.1.Mesh Refinement Verification

Different mesh densities were generated based on the number of elements across the thickness of the PPU tube and along the circumference of the wire cross section, respectively. Since the two components (i.e. the PPU tube and the wire mesh) in each model were meshed independently, the ideal way was to refine the mesh of both structures. However, refining the mesh of both structures at the same time to obtain several models of different mesh densities was computationally not feasible. Instead, the

mesh refinement was applied in such a way that each refinement step involved adjustment of mesh density of only one structure, as summarized in Table 5-1. For example, the NIEX was adjusted into the NIEX-*coarse* model by reducing the number of elements across the tube only (from 6 to 4) while preserving the elements on the wire cross section (at 10). The NIEX was refined into the NIEX-*fine* model by increasing the number of elements on the wire cross section only (from 10 to 14) while preserving the elements across the tube (at 6). Relative to the number of elements in the NIEX model, the overall number of elements was decreased by 69% and increased by 54% in the NIEX-*coarse* and NIEX-*fine* models, respectively (see Table 3-7). This approach allowed the generation of three mesh densities without exceedingly increase the computational expense. The failure of model NIEX-*fine* and PUEX-*fine* to complete the analysis, as mentioned in section 4.2.1, suggested that computational difficulties were expected with higher mesh densities.

Table 5-1: The number of elements defined across the PPU tube and along the circumference of the wire cross-section in three mesh refinement steps.

Model		NIEX-*coarse* PUEX-*coarse*	NIEX PUEX	NIEX-*fine* PUEX-*fine*
Number of Elements	PPU tube	4	6	6
	Wire	10	10	14

An agreement between model NIEX and NIEX-*fine* was observed for the curves of the strain energy and the pressure-diameter relationship, with slight difference to the NIEX-*coarse* model, (Figure 4-19 and Figure 4-21). These observations agreed with the 1% change in compliance between models NIEX and NIEX-*fine*, and 4% between NIEX and NIEX-*coarse*. Comparing the maximum stress and strain (Table 4-6 and Table 4-7) the similarities of values observed between model NIEX and NIEX-*fine* were more often than those seen between model NIEX and NIEX-*coarse*. The versions of the PU-reinforced models revealed a good agreement in the strain energy and pressure-diameter relationship plots (Figure 4-20 and Figure 4-22) between the PUEX-*coarse* and PUEX-*fine* models, except the deflection experienced by the PUEX-*coarse* model slightly before 100mmHg. The PUEX model initially agreed with the other two models but diverged from them as the pressure increased. However, the difference in compliance between the PUEX and PUEX-*fine* models (i.e. 2%) proposed a better agreement between these two models when compared to the compliance change between the PUEX and PUEX-*coarse* models (i.e. 9%). Similarly, the predicted stress

and strain values were comparable among the PUEX and PUEX-*fine* models. An overall convergence was seen on the predicted values of different output parameters as the mesh density increased from the medium to the fine one. Compromising between the computational expense and results accuracy, the middle mesh density was chosen as the standard mesh density for all the models in the study.

5.2.2.Element Type Verification

The element verification versions, NIEX-TET and PUEX-TET, were developed using 10-node quadratic tetrahedral elements. The results in section 4.2.2 represented the best among the 27 analyses performed to improve the outcome of these models. The good agreement between the models of tetrahedral and brick elements in the strain energy (Figure 4-23 and Figure 4-24), and radial deformation (Figure 4-25 and Figure 4-26) at low pressure values was not confirmed for higher pressure values. The models with tetrahedral elements terminated before completion. The models with tetrahedral elements exhibited a 27% lower number of elements compared to the brick element meshes, while the number of nodes was consistent between the different meshes. The early termination of models NIEX-TET and PUEXTET was due to convergence difficulties. These difficulties were attributed to contact problems. The tetrahedral elements were known of their poor contact behaviour. Thus it was recommended to avoided this type of element when dealing with contact problems (Muccini et al. 2000). Another possible explanation of the convergence difficulties might be the poor aspect ratio of the tetrahedral elements, particularly in the PPU tube. This issue of element aspect ratio could be further investigated by increasing the mesh density of the PPU tube; however, this was not applicable due to excessive computational cost. Accordingly, the decision was made to mesh all the models in this study using the 8-node brick elements.

5.2.3.Boundary Condition Verification

As discussed previously, symmetric BC were applied to the PPU tube and the wire mesh. The validity of symmetric BC on the wire mesh was based on the repetitive pattern of the wire loops geometry in both longitudinal and circumferential directions. To verify that the applied BC properly represented the symmetry conditions, the NIEX-BCV model was developed from model NIEX, section 3.2.3, by utilizing the cyclic symmetry interaction property (Abaqus 2008) for the PPU tube. The strain energy plots (Figure 4-27) revealed

a similar response for both models. Although the plots of the pressure-diameter relationship were not obtained, these were assumed to be similar for both models. This assumption was based on the correlation between the plots of the strain energy and radial deformation observed for most of the models. The small difference in compliance of 1% and close agreement of maximum stress and strain values between the two models supported this assumption. Thus, the agreement of the results of models NIEX-BCV and NIEX proved that the circumferential BC and the cyclic symmetry conditions were equivalent. However, the cyclic symmetry interaction could not replace the BC on the PPU tube of all models in the study for several reasons. Firstly, the cyclic symmetry interaction did not allow an automatic capturing of displacement information of the PPU tube. Plotting a graph of pressure-diameter relationship would need to manually capture the displacement value of each single node on the luminal surface of the tube at each time increment. Secondly, the cyclic symmetry interaction was physically and numerically not adequate in the EM models in which the helical-patterned wire mesh was embedded in the PPU tube.

5.2.4.Contact Definition Verification

The contact settings were frequently adjusted to achieve numerical stability of the models. An example was presented in section 3.2.4 for model NIEX during the numerical optimisation process. The NIEX-CV1 model was run with the initial contact settings and terminated before completion. Increasing the upper pressure value of the pressure-clearance relationship from initially 0.5MPa (in model NIEX-CV1) to 9MPa resulted in completion of model NIEX-. However, instability of the NIEX-CV2 model was observed at 170mmHg, as reflected by the strain energy and radial deformation plots (Figure 4-28 and Figure 4-29). This instability was treated by further increasing that contact pressure value to 12MPa (in model NIEX). The resulting strain energy curve was sufficiently smooth to consider the NIEX model as numerically stable. The strain energy plots of the three NIEX model versions seemed to have the same trend. The difference in the pressure-diameter relationship between models NIEX-CV1 and NIEX-CV2 suggested that varying the contact parameters had an impact on the predicted behaviour of the models. Therefore, optimisation of these parameters was considered for all the models in the study to ensure a reasonable accuracy of the numerical solutions.

5.2.5.Friction Verification

The NIEX-FL and NIEM-FL models, described in section 3.2.5, were the two versions of model NIEX and NIEM, respectively, developed using frictionless tangential contact. Comparing models NIEX and NIEX-FL (Figure 4-30), the higher strain energy levels predicted by model NIEX-FL at any one pressure agreed with the absence of friction, which was also confirmed by the higher values of the predicted radial deformation (Figure 4-32), compliance and maximum stress and strain. Although the difference in these values seemed to be small, the curves of the NIEX-FL diverged from those of the NIEX model as the pressure increased. This indicated that the presence of friction in the EX models might have a considerable effect on the model behaviour at higher pressure levels. On the other hand, the EM models exhibited no sensitivity to friction due to the relatively very limited movement of the embedded wire loops. Models NIEM and NIEM-FL had identical strain energy curves (Figure 4-31) and radial deformation curves (Figure 4-33) as well as equal compliance and maximum stress and strain values.

5.2.6.Material Model Verification

The PPU and NITI material models were developed and validated in previous studies (Yeoman 2004; van der Merwe 2007; van der Merwe et al. 2008; Yeoman et al. 2009) as described in section 3.1.2. The PU reinforcement was only introduced in this study for comparison purposes. Verification of the solid PU material model is recommended in future extension of this study.

The PPU material model was valid up to strains of 55% for uniaxial tension and 30% for compression (Yeoman 2004; Yeoman et al. 2009), as illustrated in Figure 5-1. The predicted strains of the PPU tubes in this study had to be examined to verify that they fall within these validation limits. The maximum predicted strain value in a PPU tube was 33% and was predicted by model PUEM at 200mmHg (Table 4-4). This value, and accordingly all the other predicted strain values, fell within the validation limit of the tensile strain. Examining the wall compression values (Table 4-2), all the predicted values were below the validation limit of compression at 80 and 120mmHg. However, the wall compression values predicted in the PPU tube of models NIEX and PUEX at 200mmHg (i.e. 37 and 36%) were above the validation limit, suggesting further investigations for these models at 200mmHg.

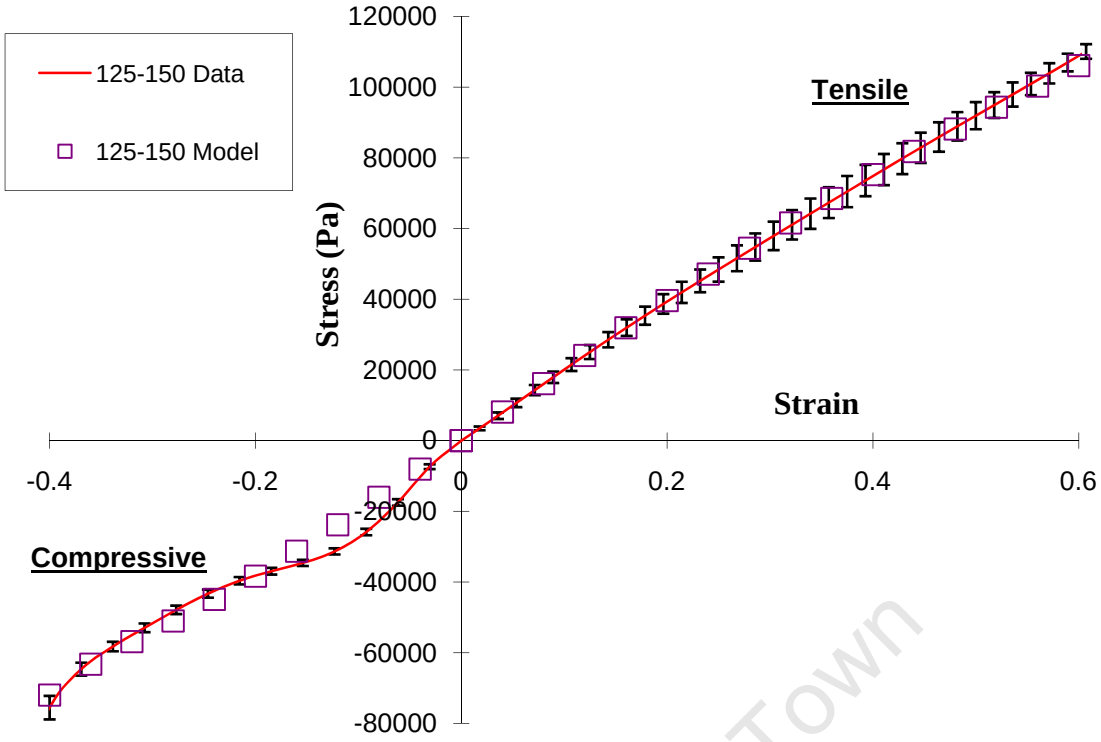

Figure 5-1: The stress vs. strain curves of the PPU graft (pores size= 125-150µ) comparing experimental tests data to numerical models (modified from (Yeoman 2004)).

5.2.7.Comparison to Compliance Values from Previous Studies

The developed FE models, comprising the EX and EM, were compared to physical data of equivalent prototypes to evaluate the accuracy of the models. The physical prototypes for the EX and EM grafts were not available in this study. Hence, the compliance data from previous studies obtained separately for the PPU tube (Yeoman et al. 2009) and the NITI wire mesh (van der Merwe et al. 2008; Franz 2009) was utilized. The PU wire mesh was not considered due to unavailability of experimental data of such structures.

The compliance predicted by models BG2.4 and BG2.8 was compared to the experimental radial compliance recorded by a BG prototype developed by Yeoman et al. (2009). The BG prototype had the same porosity used for the FE models although possessing different inner diameter and wall thickness. This was addressed by developing an additional model (BG4.0) which had the same inner diameter and wall thickness of the BG prototype. The comparison also included the compliance of a FE model of the graft also developed by Yeoman et al. (2009). Information of the prototype and the different models is summarized in Table 5-2.

Table 5-2: Comparison between the compliance values of the BG models and the BG prototype.

Samples	Inner Diameter [mm]	Wall Thickness [mm]	Compliance [%/100mmHg]	Nature of Data
BG2.4	2.4	0.3	65.05	Numerical
BG2.8	2.8	0.3	106.41	Numerical
BG4.0	4.0	0.7	31.17	Numerical
Graft Prototype*	4.0	0.7	16.4±4.6 (static) 15.5±1.3 (dynamic)	Experimental
Graft FE model*	4.0	0.7	33.9 (static) 31.5 (dynamic)	Numerical

* from (Yeoman et al. 2009).

The distensibility of an elastic tube can be expressed by the following equation (Ethier and Simmons 2007):

$$\beta = \frac{2\Delta\varepsilon}{\Delta P} = \frac{D}{Et} \tag{5.1}$$

where β is the distensibility, $\Delta\varepsilon$ is the change in circumferential strain, ΔP is the change in transmural pressure, D is the inner diameter, E is the elastic modulus of the material and t is the wall thickness of the tube. Eq (5.1) indicates that the distensibility is directly proportional to the inner diameter and inversely proportional to the wall thickness. Another equation (Levy and Tedgui 1999) showed that the distensibility of a vessel can be yielded if the diametric compliance is normalized to the vessel volume at a given transmural pressure:

$$\beta = \frac{C_D}{V} \tag{5.2}$$

From Eqs (5.1) and (5.2), the distensibility is directly proportional to the compliance, and both in turns are directly proportional to the inner diameter and inversely proportional to the wall thickness.

The BG2.4 and BG2.8 models had larger compliance values than the graft prototype and FE model of Yeoman et al. (2009). This indicated that the larger wall thickness of the grafts of Yeoman et al. (2009) was the main factor accounting for the reduction in the compliance, in spite of the larger inner diameter, compared to the BG2.4 and BG2.8. However, this indication was considered insufficient for evaluating the accuracy of models BG2.4 and BG2.8.

Model BG4.0 was developed with the same procedure and conditions used for models BG2.4 and BG2.8. The compliance predicted by model BG4.0 was slightly less than the that predicted by the FE model of Yeoman et al. (2009), but indicated acceptable agreement. This slight difference between the compliance values was attributed to the differences between the applied procedures and conditions in each study. In comparison to the compliance of the graft prototype, model BG4.0 and the FE model of Yeoman et al. (2009) were predicted considerably higher compliance values. Yeoman et al. (2009) attributed this to the difference in material/structural properties which was possibly associated with the preparation of the graft and the mechanical characterization samples used for material model development (Yeoman et al. 2009). Nevertheless, from these findings the numerical solutions predicted by models BG4.0, BG2.4 and BG2.8 were all considered over-estimated.

The compliance values predicted by models NIEX and NIEM were compared to the experimental compliance data obtained from prototypes of NITI wire mesh in previous studies at the Cardiovascular Research Unit (CVRU), Dynatek Delta and Medtronic MBC (Franz 2009). In addition, the comparison included the numerical compliance predicted by a FE model of NITI wire mesh developed by van der Merwe et al. (2008).

The CVRU experimental tests were carried out using an Instron machine with the specimens submersed in distilled water of 37ºc. Two metal rods were inserted into the wire mesh and displaced applying a circumferential tension. The tests of Dynatek Delta utilized a cyclic water-pressurized system to measure the volumetric compliance of the wire meshes combined with a luminal latex liner. The diametric compliance was calculated from the volumetric compliance with correction for the stiffening effect of the latex liner. The set up of the Medtronic MBC tests was similar to that of Dynatek Delta except that a) the compliance was determined from the outer diameter measured with laser micrometer and b) the latex was not corrected. The wire mesh prototypes developed in each of these experimental tests, as well as the mesh FE model of Merwe et al. (2008), had wire thickness of 0.05mm and inner diameter of 3.35mm. The wire mesh included in models NIEX and NIEM had the same wire thickness but an inner diameter of 3.0mm.

Information of the prototypes and the different models is summarized in Table 5-3. The NIEX and NIEM models included the PPU tube. The compliance values predicted by them were based on the change in the inner diameter (i.e. the inner surface) of the PPU

tube. For the NIEX graft model the compliance value predicted by the outer surface of the PPU tube was also included.

Table 5-3: Comparison between the compliance values of the NITI-reinforced models and experimental tests.

Samples	Inner Diameter [mm]	Compliance [%/100mmHg]	Nature of Data
NIEX Graft	2.4 (ID) 3.0 (OD)	7.02 (inner surface) 4.08 (outer surface)	Numerical
NIEM Graft	2.8	1.24	Numerical
CVRU Mesh [a]	3.35	5.12±0.8	Experimental
Dynatec Mesh [a]	3.35	4.55±0.6	Experimental
MBC Mesh [a]	3.35	4.15±1.9	Experimental
Mesh FE Model [b]	3.35	2.5	Numerical

[a] from (Franz 2009), [b] from (van der Merwe et al. 2008).

When comparing the two compliance values predicted by the NIEX model with the experimental values, an acceptable similarity was found between the compliance based on the outer surface and the experimental values of the wire meshes. In fact, the wire mesh in the NIEX model lied on the outer surface of the PPU tube. Therefore the change in the outer diameter of the PPU tube would result in a change in the inner diameter of the wire mesh. Thus the compliance of the wire mesh in the NIEX model could reasonably be represented by the compliance of the outer surface of the PPU tube (i.e. 4.08 %/100mmHg). The transmural pressure acting on the inner surface of the wire mesh was less than the actual pressure applied on the inner surface of the PPU tube due to pressure attenuation through the thickness of the tube. Therefore the actual compliance of the wire mesh at 80 and 120mmHg was in fact larger than 4.08 %/100mmHg and approaching the experimental compliance values. Recalling that the wire mesh prototypes and the mesh FE model of van der Merwe et al. (2008) had larger inner diameter than the wire mesh in the NIEX model, the wire mesh in model NIEX should predict smaller compliance value, based on Eqs. (5.1) and (5.2). Accordingly, the compliance of the wire mesh in the NIEX model was considered over-estimated encouraging further investigation.

It was difficult to determine the compliance of the wire mesh in the NIEM model. However, the predicted compliance of the NIEM model was considerably lower than that

of the NIEX model. In the NIEM the wire mesh was completely embedded in the wall of the PPU tube. This embedded position disallowed the crossings of the wire loops from sliding on each other reducing the overall distensibility of the wire mesh.

5.3.Comparison between the Finite Element Models

The NITI and solid PU were used as materials for the knitted wire mesh structure which was utilized to provide external and embedded reinforcement, respectively, for the PPU tube. The different numerical predictions, obtained by the standard models (i.e. NIEX, PUEX, NIEM, PUEM, BG2.4 and BG2.8), were presented in section 4.1. The results of these models will be compared and discussed based on the predicted strain energy, pressure-diameter relationship (i.e. radial deformation), compliance, wall compression, and maximum principal stress and strain.

The maximum stress and strain values predicted in the PPU tube of the six models indicated a recoverable elastic deformation of the PPU tube when compared to the stress-strain plots in Figure 5-1. The maximum predicted stress value (157.9MPa) in the NITI wire mesh was 33% of the stress associated with the start of austenite-martensite phase transformation in the NITI wire mesh, i.e. 483 MPa (van der Merwe et al. 2008), confirming the 0% martensite fraction predicted in the NITI wire meshes. The maximum predicted strain was uncritical considering a typical high-cycle recoverable strain of NITI of 2% (NN 2006). The stress and strain values predicted in the PU wire meshes were compared to tensile properties of generic PU materials (Grapski and Cooper 2001) which had elastic moduli, 534±37 and 581±54MPa, close to the one used for the definition of solid PU material model in this study (i.e. 570MPa). Although the predicted strain values in the PU wire mesh indicated a recoverable elastic deformation, the predicted stresses (39 and 45MPa) were found critical at pressure 200mmHg, indicating a possibility of plastic deformation.

5.3.1.Bare Graft Models

The BG2.4 and BG2.8 models represented the non-reinforced PPU tube. These models were included in the study to provide information for the evaluation of the reinforcement effects. The strain energy and radial deformation curves predicted by both models showed a common characteristic (Figure 4-3 and Figure 4-6). These curves exhibited

considerable change in the slope after 120mmHg. This was accompanied by numerical instability causing the termination of model BG2.4 and BG2.8 when approaching 150mmHg and 170mmHg, respectively. The numerical instability was attributed to the excessive dilation experienced by the models. The predicted values of radial dilation of 500-600% appeared to be unrealistic and might indicate structural failure. However, the prediction of structural failure could not be incorporated in the FE models.

The BG2.8 model predicted higher strain energy and greater deformation than BG2.4 at any given pressure. The BG2.8 model also predicted larger values of compliance, wall compression, maximum principal stress and maximum principal strain (Table 4-1 to Table 4-4) at any give pressure value. Since both models comprised the same material, the differences in predicted values were related to the different diameters. This could be demonstrated by Laplace's Law (Caro et al. 1979):

$$F = \frac{PD}{2} \tag{5.3}$$

where F is the circumferential force (tension), P is the transmural pressure and D is the inner dimeter. Other forms of Laplace's Law including the stress σ and strain ε are:

$$\sigma = \frac{F}{t} = \frac{PD}{2t} \tag{5.4}$$

$$\varepsilon = \frac{PD}{2Et} \tag{5.5}$$

where E is the elastic modulus of the material and t is the wall thickness of the tube. Based on Eqs. (5.3) to (5.5), with the material and applied pressure being the same in both models, the larger inner diameter of model BG2.8, compared to model BG2.4, resulted in larger circumferential tensile forces causing larger deformation and stresses. Since the circumferential tension was the predominant cause of wall contraction in the bare grafts (Yeoman et al. 2009), the larger inner diameter of model BG2.8 would also result in larger wall compression, at a given pressure, due to the larger induced circumferential tension. From Eqs (5.1) and (5.2), the larger compliance predicted for model BG2.8 was also related to its larger inner diameter compared to model BG2.4.

In spite of the different predicted values of stress and strain, the BG2.4 and BG2.8 predicted the same distribution of stress (Figure 4-9 and Figure 4-12) and strain (Figure 4-15 and Figure 4-18). Both models predicted a continuous increase in the stress and strain from the external to the internal surfaces of the PPU tube. Hearn (1996) stated that

the circumferential stress decreased through the wall thickness to the outer surface with the inverse square of the radius, while the axial stress was constant throughout the wall, and the radial stress was a maximum compressive (radial) stress on the inner surface and reduced to zero at the outer surface. The resultant stress and strain distribution predicted by models BG2.4 and BG2.8 were believed to result from a similar distribution of the circumferential and radial components of stress and strain. Earlier study concluded the existence of stress concentration at the vascular intima and the ventricular sub-endocardium, resulting in a much higher circumferential stress at the inner than the outer wall (Chuong and Fung 1983).

Generally, the predicted mechanical behaviour of BG2.4 and BG2.8 models revealed high distensibility and structural weakness. The compliance range of the small and medium arteries was reported to be 8.0±5.9%/100mmHg (Tai et al. 2000). The predicted compliance of the BG models, of 65.05 and 106.41%/100mmHg, excessively exceeded this physiological arterial value.

5.3.2.External Reinforcement Models

The NIEX and PUEX models represented the two versions of model BG2.4 when externally reinforced with NITI and PU wire meshes, respectively. The aim was to evaluate the mechanical behaviour of the grafts when externally reinforced by structures of the same geometry and different stiffness.

The NIEX model predicted lower strain energy and deformation levels, in the PPU tube and wire mesh, than the PUEX model (Figure 4-1 and Figure 4-4). This was attributed to the higher stiffness of the NITI wire mesh (E = 38,992MPa) relative to the PU wire mesh (E = 570MPa). The NIEX and PUEX models predicted a non-linear radial deformation. As the pressure increased both models gained stiffness. This non-linear behaviour of the grafts was governed by the individual deformation of the PPU tube and the wire mesh. When the pressure was applied, the PPU tube started to deform radially. This deformation increased as the pressure increased. As the PPU deformed, the crossings of the wire loops in the mesh began to tighten. Thereafter, the wire mesh deformed with relatively less distensibility resisting further deformation of the PPU tube and increasing the stiffness of the graft. The non-linear deformation behaviour of blood vessels under luminal pressure (Holzapfel et al. 2000) was explained in a similar way in which the

elastin in the media deformed initially and then the wavy bundles of relatively stiffer collagen got tightened controlling the mechanics of the vessel at higher pressures. A similar deformation was exhibited by a small-diameter PU vascular graft when reinforced with weft-knitted tubular fabric (Xu et al. 2010).

The PUEX model predicted higher compliance than the NIEX model (Table 4-1) due to the lower stiffness of the PU wire mesh compared to the NITI wire mesh. The wall compression values predicted by models NIEX and PUEX were found to be similar (Table 4-2).

Comparing the maximum principal stress and strain predicted in model NIEX and PUEX (Table 4-3 and Table 4-4), the NITI wire mesh predicted larger values of stress and lower values of strain than the PU wire mesh. This was governed by the larger elastic modulus of the NITI material compared to the solid PU which was directly proportional to the stress and inversely proportional to the strain. The PPU tube predicted smaller values of stress and strain in the NIEX model compared to the PUEX model, due to the smaller dilation associated with the relatively stiffer NITI wire mesh.

5.3.3.Embedded Reinforcement Models

The NIEM and PUEM models represented the embedded reinforced versions of model BG2.8 using the NITI and PU wire meshes, respectively. The EM models were developed to assess the mechanical behaviour of the grafts when the reinforcing structures are embedded in the wall of the PPU tube.

The NIEM model predicted lower levels of strain energy and radial deformation than the PUEM model (Figure 4-2 and Figure 4-5). This was based on the higher stiffness of the NITI wire mesh (E = 38,992MPa) relative to the PU wire mesh (E = 570MPa). Unlike the EX models, the NIEM and PUEM models predicted a linear radial deformation. As described previously, the non-linear deformation of the EX models was due to the tightening of the wire loops whose stiffness affected the deformation at higher pressures. In the EM models, the wire mesh was completely embedded in the PPU tube and the wire loops were no longer allowed to slide over each others. This linear deformation of the EM models was largely due to the composite effect of the PPU and wire mesh materials.

The PUEM model predicted higher compliance than the NIEM model (Table 4-1) due to the relatively lower stiffness of the PU wire mesh compared to the NITI wire mesh. A negligible difference was observed between the wall compression predicted by model NIEM and PUEM (Table 4-2).

Comparing the maximum principal stress and strain predicted in models NIEM and PUEM (Table 4-3 and Table 4-4), the NITI wire mesh predicted larger values of stress and lower values of strain than the PU wire mesh, due to the relatively larger elastic modulus of the NITI material. The PPU tube predicted smaller values of stress and strain in the NIEM model compared to the PUEM model, due to the smaller dilation associated with the relatively stiffer NITI wire mesh.

5.3.4.Cross-Comparison of Models

The overall strength and mechanical behaviour of the graft was considerably improved by the external reinforcement when comparing the EX models to the BG2.4. The external reinforcement prevented the excessive dilation exhibited by the bare graft. The compliance of the EX models approached the desired arterial compliance range (i.e. 8.0±5.9%/100mmHg). As a result of the reduced dilation, the stress and strain values predicted in the PPU tube were generally smaller in the EX models when compared to the BG2.4 model. However, an increase in the wall compression was observed in the EX models, when compared to the BG2.4 model. In the non-reinforced model, transverse contraction of the wall due to radial dilation and circumferential stretch was the major factor of wall thinning whereas compression of the wall due to the luminal pressure was secondary (Yeoman et al. 2009). With the wire mesh externally reinforcing the PPU tube in the EX models, radial dilation, circumferential stretch and the associated transverse contraction of the wall was limited. Compression of the wall due to the luminally applied pressure was the predominant cause of wall thinning.

The composite mechanical strength of the graft due to the embedded reinforcement, in the EM models, was improved when compared to the mechanical behaviour predicted by the bare graft model BG2.8. The excessive dilation exhibited by the BG2.8 was rectified, reducing the radial compliance nearly to the physiological range (i.e. 8.0±5.9%/100mmHg). The reduced dilation of the EM models caused a decrease in stress and strain values predicted in the PPU tube compared to the BG2.8 model. Unlike

the EX models, the wall compression predicted by the EM models were slightly smaller than the values predicted by the BG2.8 model. The embedded wire mesh reduced both of the contributing factors; the pressure- and tension-induced wall compression.

The EM models predicted a higher stiffness and caused larger reduction, 94% and 99%, in the compliance of the BG models compared to the EX models (i.e.76% and 89%), resulting in smaller compliance values for the EM models. Based on Eqs. (5.1) to (5.5), and due to the larger inner diameter of the EM models compared to the EX models, one would expect that the radial deformation and compliance predicted by the EM models would be greater than that predicted by the corresponding (i.e. with the same wire mesh material) EX models. The predictions of the FE models, however, revealed that the radial deformation and compliance predicted by an EM model was much less than that of the corresponding EX model. The higher stiffness of the EM models compared to the EX models was attributed to the embedding of the wire mesh disallowing the sliding of the wire loops on each others. These findings might have importance in clinical applications. For example, during the implantation operation of a graft externally reinforced with wire mesh, fibrin glue, or other adhesives, is used to attach the graft to the wire mesh to maintain an open lumen during the operation (Mikucki and Greisler 1999). This usually involves coating of the stent graft with the fibrin glue providing a fibrin layer enclosing the graft and mesh. This new composite form may change the mechanical behaviour of the stent graft affecting its compliance.

5.3.5.Tissue Engineering Relevance

Wall compression is a very important factor when considering the tissue-regenerating characteristic of the PPU graft. Wall compression will reduce the pore window of the graft which is essential for the transmural ingrowth of cells, tissue and capillaries (Yeoman et al. 2009). The average diameter of capillaries ranges from 8 to 10μm and the diameter of a functional arteriole (including endothelium and smooth muscle) is approximately 30μm (Fung 1993; Gamble et al. 1993).

The maximum wall compression predicted among the different models was 37.24% at 200mmHg. The PPU scaffold used in this study featured a minimum pore window diameter of approximately 65μm (Yeoman et al. 2009). Under the 37.24% wall compression, the minimum pore window diameter would be reduced to 41μm. This value

suggested that the tissue-regenerating characteristic of all grafts, from the ingrowth perspective, would not be affected since the scaffold would permit the cellular ingrowth.

However, in the EM grafts, the local wall compression in the PPU portion located between the wire mesh and the luminal surface, as illustrated in Figure 5-2, was not captured in this study. Further investigations to assess the capability of this portion to permit tissue ingrowth were encouraged.

Figure 5-2: Cross-sectional view in the EM graft model highlighting the portion of PPU tube (shaded) that lies between the embedded wire mesh and the inner surface of the graft.

5.4.Limitations

Various limitations were encountered in the previous sections. This section is a summary of those limitations.

The difference in the inner diameter between the EX and EM geometries was caused from the approach applied to embed the wire mesh in the PPU tube. This difference limited the possible range of cross-comparison between the different models.

The PU reinforcement was introduced in this study for initial comparison purposes which motivated the use of a simple linear elastic material model. The high deformation exhibited by the PU-reinforced models in this study strongly encourages utilisation of a non-linear constitutive model for the PU wire mesh in future studies.

A symmetric boundary condition was applied to the wire mesh based on the repetitive pattern of the knitted wire loops in both longitudinal and circumferential directions. This approach ignored the helical orientations of the loops which, in turns, might degrade the accuracy of the applied boundary condition.

The numerical analysis incorporated a first step in which the contact between the different surfaces in a model was established. This step caused variation in the inner

diameter of the EX models at the beginning of the actual analysis step (i.e. pressure loading). This might have influenced the displacement-related data predicted by those models.

The limited computational feasibility disallowed an optimal mesh refinement assessment. Refining the mesh density of both the PPU tube and the wire mesh structures simultaneously was not feasible, instead, one structure at a time was refined.

The data predicted by developed models were compared to experimental data of individual prototypes of the wire mesh and the PPU tube separately. Unavailability of physical prototypes of the assembled modelled grafts might have not provided the accurate means of comparison.

6. Conclusions and Recommendations

6.1. Conclusions

The objective of this study was to computationally model a multi-component, small-diameter, non-degradable synthetic graft composed of ingrowth permissible porous polyurethane foam graft and reinforced with knitted wire mesh structure to assist in technology and prototype development. The primary goal was to achieve the mechanical designs towards the long term structural integrity of the graft and the mimicking of arterial mechanics.

The finite element analyses of six models were successfully accomplished using the commercial software Abaqus CAE 6.8-2. The numerical stability and consistency of the models were verified through a number of verification tests. Numerical results were validated using experimental and numerical data of previous studies reported in literature.

This study concluded the structural and mechanical behaviour of the reinforced grafts. The mechanical and structural properties of the individual components of the graft and the way these components are assembled were found to be the determinant of the overall mechanical behaviour of the graft. Embedding the reinforcing structure in the porous polyurethane tube can increase its strength remarkably more than just externally supporting it. The compliance predicted by the different models was found to be near the desired physiological range, indicating that the compliance matching is attainable through the presented reinforcement systems. Structural parameters, such as the wall thickness of the porous polyurethane tube, and the wire thickness of the reinforcing structure can effectively be controlled to achieve the desired mechanical performance.

In general, the developed models helped exploring the mechanical behaviour of the reinforced tissue-regenerating vascular grafts. The outcomes of this study provided preliminary conceptions for structural optimisation towards improved mechanical performance of such devices. The implemented modelling approach can be used in the development of tissue-regenerating vascular graft.

6.2.Recommendations

The porosity is an important factor regarding the tissue-regenerating function of the developed grafts. Representing the microscopic structure of the porous polyurethane tube in the future can provide more realistic models to investigate the cellular ingrowth. In addition, modelling the biodegradability of the porous scaffolds can be a beneficial extension since this type of material offer a great potential for tissue-regenerating vascular prosthetics.

Due to the geometry of the wire mesh, bulging of the porous polyurethane tube was observed. The bulged luminal surfaces may cause an unwanted disturbed blood flow. Therefore a future extension of this study may utilize computational fluid dynamics in the investigation of the pressurized graft models to evaluate the effects of these uneven surfaces on the blood flow and the luminal wall shear stress.

This study examined the graft models under static pressure loading. Hence, a dynamic analysis simulating physiological arterial pressure profiles can provide additional information for the design and evaluation of the graft models.

Various areas of extensions were proposed during working in this study. These can be summarized as follows:

- Characterization of the solid polyurethane material and development of a non-linear constitutive model for the solid polyurethane wire mesh.
- Compare the predictions of the finite element models to experimental data of equivalent prototypes.
- Exploring the reasons of stress and strain reduction observed in the reinforced porous polyurethane tube compared to the non-reinforced one.
- Investigation of the wall compression of the embedded-reinforced grafts, considering the portion located between the wire mesh and the luminal surface of the porous polyurethane tube.
- Investigation of the composite material properties resulted from the embedding the wire mesh in the porous polyurethane tube.

References

Abaqus (2008). Analysis User's Manual. Providence, RI, USA, V 6.8-2. Dassault Systèmes.

Auricchio, F. and R. L. Taylor (1997). "Shape-memory alloys: modelling and numerical simulations of the finite-strain superelastic behavior." Computer Methods in Applied Mechanics and Engineering **143**(1-2): 175-194.

Auricchio, F. and R. L. Taylor (1997). "Shape-memory alloys: Modelling and numerical simulations of the finite-strain superelastic behaviour." Computer Methods in Applied Mechanics and Engineering **143**: 175-194.

Auricchio, F., R. L. Taylor and J. Lubliner (1997). "Shape-memory alloys: Macromodelling and numerical simulations of the superelastic behaviour." Computer Methods in Applied Mechanics and Engineering **146**: 281-312.

Baird, R. N., I. G. Kidson, G. J. L'Italien and W. M. Abbott (1977). "Dynamic compliance of arterial grafts." Am J Physiol **233**(5): H568-72.

Ballyk, P. D., C. Walsh, J. Butany and M. Ojha (1997). "Compliance mismatch may promote graft-artery intimal hyperplasia by altering suture-line stresses." Journal of Biomechanics **31**(3): 229-237.

Ballyk, P. D., C. Walsh, J. Butany and M. Ojha (1998). "Compliance mismatch may promote graft-artery intimal hyperplasia by altering suture-line stresses." J Biomech **31**(3): 229-37.

Belz, G. G. (1995). "Elastic properties and Windkessel function of the human aorta." Cardiovasc Drugs Ther **9**(1): 73-83.

Berthier, B., R. Bouzerar and C. Legallais (2002). "Blood flow patterns in an anatomically realistic coronary vessel: influence of three different reconstruction methods." Journal of Biomechanics **35**(10): 1347-1356.

Bezuidenhout, D. (2001). Porous Polymeric Superstructures as In-Growth Scaffolds for Tissue-Engineered Vascular Prosthesis. Cape Town, Stellenbosch University. **PhD**.

Bezuidenhout, D., N. Davies and P. Zilla (2002). "Effect of well defined dodecahedral porosity on inflammation and angiogenesis." Asaio J **48**(5): 465-71.

Bezuidenhout, D., N. Davies and P. Zilla (2002). "Effect of Well Defined Dodecahedral Porosity on Inflammation and Angiogenesis." ASAIO JOURNAL - HAGERSTOWN- **48**: 465-471.

Bos, W. T. G. J., I. F. J. Tielliu, C. J. Zeebregts, T. R. Prins, J. J. A. M. van den Dungen and E. L. G. Verhoeven (2008). "Results of Endovascular Abdominal Aortic Aneurysm Repair with the Zenith stent-graft." European Journal of Vascular and Endovascular Surgery **36**(6): 653-660.

Brinson, C., I. Schmidt and R. Lammering (2004). "Stress-induced transformation behaviour of a polycrystalline NiTi shape memory alloy: micro and macro-mechanical investigations via in situ optical microscopy." Journal of the Mechanics and Physics of Solids **52**: 1549-1571.

Butler, D. L., S. A. Goldstein and F. Guilak (2000). "Functional Tissue Engineering: The Role of Biomechanics." Journal of Biomechanical Engineering **122**(6): 570-575.

Byrne, D. P., D. Lacroix, J. A. Planell, D. J. Kelly and P. J. Prendergast (2007). "Simulation of tissue differentiation in a scaffold as a function of porosity, Young's modulus and dissolution rate: Application of mechanobiological models in tissue engineering." Biomaterials **28**(36): 5544-5554.

Campbell, G. R. and J. H. Campbell (2007). "Development of Tissue Engineered Vascular Grafts." Current Pharmaceutical Biotechnology **8**(1): 43-50.

Caro, C. G., T. J. Pedley, R. C. Schroter and W. A. Seed (1979). The Mechanics of the Circulation, Oxford University Press.

Chandran, K. B., D. Gao, G. Han, H. Baraniewski and J. D. Corson (1992). "Finite-element analysis of arterial anastomoses with vein, Dacron and PTFE grafts." Med Biol Eng Comput **30**(4): 413-8.

Cheremisinoff, N. P. (1991). Handbook of Ceramics and Composites: Mechanical properties and specialty applications, CRC Press.

Chung, K. W. (2005). Gross anatomy, Lippincott Williams & Wilkins.

Chuong, C. J. and Y. C. Fung (1983). "3-DIMENSIONAL STRESS-DISTRIBUTION IN ARTERIES." BIOMECHANICAL ENGINEERING-TRANSACTIONS OF THE ASME **105**(3): 268-274.

Crowley, L. V. (2009). An Introduction to Human Disease: Pathology and Pathophysiology Correlations, Jones & Bartlett Publishers.

David Chua, S. N., B. J. MacDonald and M. S. J. Hashmi (2004). "Finite element simulation of slotted tube (stent) with the presence of plaque and artery by balloon expansion." Journal of Materials Processing Technology **155-156**: 1772-1779.

Davies, N., S. Dobner, D. Bezuidenhout, C. Schmidt, M. Beck, A. H. Zisch and P. Zilla (2008). "The dosage dependence of VEGF stimulation on scaffold neovascularisation." Biomaterials **29**(26): 3531-3538.

Dobrin, P., F. Littooy, J. Golan, B. Blakeman and J. Fareed (1988). "Mechanical and histologic changes in canine vein grafts." J Surg Res **44**(3): 259-65.

Dollie, A. (2007). CFD Analysis of an Artificial Blood Vessel with Helical Inner Surface. Department of Mechanical Engineering. Cape Town, University of Cape Town**:** 61.

Dorland, W. A. N. (2000). Dorland's illustrated medical dictionary, Saunders.

El Zahab, Z., E. Divo and A. Kassab (2009). "Minimisation of the wall shear stress gradients in bypass grafts anastomoses using meshless CFD and genetic algorithms optimisation." Computer Methods in Biomechanics and Biomedical Engineering.

Eroschenko, V. P. and M. S. H. d. Fiore (2008). Di Fiore's atlas of histology with functional correlations, Lippincott Williams & Wilkins.

Etave, F., G. Finet, M. Boivin, J.-C. Boyer, G. Rioufol and G. Thollet (2001). "Mechanical properties of coronary stents determined by using finite element analysis." Journal of Biomechanics **34**(8): 1065-1075.

Ethier, C. R. and C. A. Simmons (2007). Introductory Biomechanics: From Cells to Organisms. Cambridge, Cambridge University Press.

Franz, T. (2009). Personal Communications. Cardiovascular Research Unit, University of Cape Town.

Fuchs, J. C., J. S. Mitchener, 3rd and P. O. Hagen (1978). "Postoperative changes in autologous vein grafts." Ann Surg **188**(1): 1-15.

Fung, Y.-c. (1993). Biomechanics: mechanical properties of living tissues, Springer.

Gall, K., J. Tyber, V. Brice, C. P. Frick, H. J. Maier and N. Morgan (2005). "Tensile deformation of NiTi wires." J Biomed Mater Res A **75**(4): 810-23.

Gamble, J. R., L. J. Matthias, G. Meyer, P. Kaur, G. Russ, R. Faull, M. C. Berndt and M. A. Vadas (1993). "Regulation of in vitro capillary tube formation by anti-integrin antibodies." J. Cell Biol. **121**(4): 931-943.

Gay, M., L. Zhang and W. K. Liu (2006). "Stent modeling using immersed finite element method." Computer Methods in Applied Mechanics and Engineering **195**(33-36): 4358-4370.

Gong, X. Y. and A. R. Pelton (2002). ABAQUS Analysis on Nitinol Medical Applications. ABAQUS Users' Conference, Newport, Rhode Island.

Gorman, S. P., D. S. Jones, M. C. Bonner, M. Akay and P. F. Keane (1997). "Mechanical performance of polyurethane ureteral stents in vitro and ex vivo." Biomaterials **18**(20): 1379-1383.

Grapski, J. A. and S. L. Cooper (2001). "Synthesis and characterization of non-leaching biocidal polyurethanes." Biomaterials **22**(16): 2239-2246.

Gundiah, N., M. B. Ratcliffe and L. A. Pruitt (2009). "The biomechanics of arterial elastin." Journal of the Mechanical Behavior of Biomedical Materials **2**(3): 288-296.

Haimovici, H. (1984). History of vascular surgery. Vascular surgery. Principles and techniques. H. Haimovici. Norwark, Connecticut, Appleton-Century-Crofts**:** 3-18.

Ham, A. W. and D. H. Cormack (1979). Histology, Lippincott.

Hayashi, K., K. Takamizawa, T. Saito, K. Kira, K. Hiramatsu and K. Kondo (1989). "Elastic properties and strength of a novel small-diameter, compliant polyurethane vascular graft." Journal of biomedical materials research **23**(A2): 229-44.

Hearn, E. J. (1996). Mechanics of Materials. Oxford, Butterworth-Heinemann.

Hess, F., C. Jerusalem and B. Braun (1983). "The endothelialization process of a fibrous polyurethane microvascular prosthesis after implantation in the abdominal aorta of the rat. A scanning electron microscopic study." The Journal of cardiovascular surgery **24**(5).

Holzapfel, G. A., R. Eberlein, P. Wriggers and H. W. Weizsäcker (1996). "Large strain analysis of soft biological membranes: Formulation and finite element analysis." Computer Methods in Applied Mechanics and Engineering **132**(1-2): 45-61.

Holzapfel, G. A., T. C. Gasser and R. W. Ogden (2000). "A New Constitutive Framework for Arterial Wall Mechanics and a Comparative Study of Material Models." Journal of Elasticity **61**(1-3): 1-48.

How, T. V., R. Guidoin and S. K. Young (1992). "Engineering design of vascular prostheses." Proceedings of the Institution of Mechanical Engineers. Part H, Journal of engineering in medicine **206**(2): 61-71.

Human, P., T. Franz, J. Scherman, L. Moodley and P. Zilla (2009). "Dimensional analysis of human saphenous vein grafts: Implications for external mesh support." The Journal of Thoracic and Cardiovascular Surgery **137**(5): 1101-1108.

Jaecques, S. V. N., H. Van Oosterwyck, L. Muraru, T. Van Cleynenbreugel, E. De Smet, M. Wevers, I. Naert and J. Vander Sloten (2004). "Individualised, micro CT-based finite element modelling as a tool for biomechanical analysis related to tissue engineering of bone." Biomaterials **25**(9): 1683-1696.

Kannan, R. Y., H. J. Salacinski, P. E. Butler, G. Hamilton and A. M. Seifalian (2005). "Current status of prosthetic bypass grafts: a review." J Biomed Mater Res B Appl Biomater **74**(1): 570-81.

Kim, Y.-H., J.-E. Kim, Y. Ito, A. Shih, B. Brott and A. Anayiotos (2008). "Hemodynamic Analysis of a Compliant Femoral Artery Bifurcation Model using a Fluid Structure Interaction Framework." Annals of Biomedical Engineering **36**(11): 1753-1763.

King, M., P. Blais, R. Guidoin, E. Prowse, M. Marcois, C. Gosselin and H. Noel (1981). Polyethylene terephthalate (Dacron) vascular prostheses - material and fabric construction aspects. Biocompatibility of Clinical Implant Materials. **II:** 177-207.

Kirk, C. S., M. Horrocks, M. A. R and C. J. B (2002). "Modelling and simulation of vascular tissue engineering using the finite volume method." European Cells and Materials **4**(2): 141.

Kleinstreuer, C., Z. Li, C. A. Basciano, S. Seelecke and M. A. Farber (2008). "Computational mechanics of Nitinol stent grafts." Journal of Biomechanics **41**(11): 2370-2378.

Klinkert, P., P. N. Post, P. J. Breslau and J. H. van Bockel (2004). "Saphenous Vein Versus PTFE for Above-Knee Femoropopliteal Bypass. A Review of the Literature." European Journal of Vascular and Endovascular Surgery **27**(4): 357-362.

Lamba, N. M. K., K. A. Woodhouse, S. L. Cooper and M. D. Lelah (1998). Polyurethanes in biomedical applications, CRC Press.

Levy, B. and A. Tedgui, Eds. (1999). Biology of the arterial wall. Dordrecht, Kluwer.

Lyman, D. J., F. J. Fazzio, H. Voorhees, G. Robinson and D. Albo, Jr. (1978). "Compliance as a factor effecting the patency of a copolyurethane vascular graft." J Biomed Mater Res **12**(3): 337-45.

Lyman, D. J., F. J. Fazzio, H. Voorhees, G. Robinson and J. D. Albo (1978). "Compliance as a factor effecting the patency of a copolyurethane vascular graft." Journal of biomedical materials research **12**(3): 337-345.

MacKellar, I. (1998). The mechanical design aspects of a small diameter vascular prosthesis, University of Cape Town. **Master's thesis**.

Magee, T. R., P. G. Niblett and W. B. Campbell (1992). "Reinforced vascular grafts: a comparative study." Eur J Vasc Surg **6**(1): 21-25.

Mansfield, P. B., A. R. Wechezak and L. R. Sauvage (1975). "Preventing Thrombus on Artificial Vascular Surfaces: True Endothelial Cell Linings." ASAIO Journal **21**: 264-272.

Maton, A. (1997). Human Biology and Health, Prentice Hall.

Meissner, S. (2004). On Constitutive Modeling of Shape Memory Alloys Within the Finite Element Method. Munich, Technichal University Munich**:** 83.

Mikucki, S. A. and H. P. Greisler (1999). "Novel Uses of Fibrin Glue in Vascular Surgery." Perspectives in Vascular Surgery and Endovascular Therapy **11**(2): 41-57.

Min, H. K., Y. T. Lee, W. S. Kim, J. H. Yang, K. Sung, T. G. Jun and P. W. Park (2009). "Complete revascularization using a patent left internal thoracic artery and variable arterial grafts in multivessel coronary reoperation." The heart surgery forum **12**(5): 244-9.

Mooney, D. J., D. F. Baldwin, N. P. Suh, J. P. Vacanti and R. Langer (1996). "Novel approach to fabricate porous sponges of poly(-lactic-co-glycolic acid) without the use of organic solvents." Biomaterials **17**(14): 1417-1422.

Mooney, M. (1940). "A theory for large elastic deformation." Journal of Applied Physics **11**: 582-597.

Moore, K. L. and A. M. R. Agur (2007). Essential clinical anatomy, Lippincott Williams & Wilkins.

Moritz, A., F. Grabenwoger, A. Windisch, R. Horvath, U. Windberger, U. Losert and E. Wolner (1990). "A method for constricting large veins for use in arterial vascular reconstruction." Artif Organs **14**(5): 394-8.

Moritz, A., F. Raderer, H. Magometschnigg, W. Trubel, R. Ullrich, G. Laufer and M. Staudacher (1992). "The use of mesh-tube-constricted dilated or varicose veins as arterial bypass conduit." Thorac Cardiovasc Surg **40**(6): 356-60.

Mortier, P. (2010). Computer Modelling of Coronary Bifurcation Stenting. Belgium, Ghent University. **PhD**.

Muccini, R., M. Baleani and M. Viceconti (2000). "Selection of the best element type in the finite element analysis of hip prostheses." Journal of Medical Engineering & Technology **24**(4): 145-148.

Nagahama, H., Y. Fukushima, T. Hayase, M. Yoshioka and T. Onitsuka (2005). "Reinforcement of saphenous vein graft with ePTFE graft for auxillocoronary bypass grafting." The Annals of Thoracic Surgery **79**: 700-701.

Nerem, R. M. and A. Sambanis (1995). "Tissue Engineering: From Biology to Biological Substitutes." Tissue Engineering **1**(1): 3-13.

Nielsen, L. E. and R. F. Landel (1994). Mechanical properties of polymers and composites, CRC Press.

NN. (2006). "Info sheet No. 4." Selected properties of NiTi, from http://www.memory-metalle.de/html/03_knowhow/PDF/MM_04_properties_e.pdf.

O'Rourke, M. (1995). "Mechanical Principles in Arterial Disease." Hypertension **26**(1): 2-9.

O'Rourke, M. F. and J. Hashimoto (2006). "The arterial system; its influence on the heart and circulation." Artery Research **1**(Supplement 1): S7-S14.

Ogden, R. W. (1984). Non-Linear Elastic Deformations. NY, John Wiley and Sons.

Oshima, M., R. Torii, T. Kobayashi, N. Taniguchi and K. Takagi (2001). "Finite element simulation of blood flow in the cerebral artery." Computer Methods in Applied Mechanics and Engineering **191**(6-7): 661-671.

Papaharilaou, Y., J. A. Ekaterinaris, E. Manousaki and A. N. Katsamouris (2007). "A decoupled fluid structure approach for estimating wall stress in abdominal aortic aneurysms." Journal of Biomechanics **40**(2): 367-377.

Pitman, M. W. (2007). An investigation of flow structure interactions on a finite compliant surface using computational methods. Mechanical Engineering, Curtin University of Technology. **PhD:** 185.

Prendergast, P. J. and P. E. McHugh, Eds. (2004). Topics in Bio-Mechanical Engineering. Dublin, Trinity Centre for Bioengineering & the National Centre for Biomedical Engineering Science.

Rebelo, N., **N. Walker** and **H. Foadian** (2001). Simulation of implantable nitinol stents. Proceedings of the 2001 ABAQUS Users conference.

Rivlin, R. S. (1949). "Large Elastic Deformations of Isotropic Materials. VI. Further Results in the Theory of Torsion, Shear and Flexure." Philosophical Transactions of the Royal Society of London. Series A, Mathematical and Physical Sciences **242**(845): 173-195.

Ryhanen, J. (1999). Biocompatibility Evaluation of Nickel-Titanium Shape Memory Metal Alloy. Oulu, Finland, Oulu University**:** 117.

Sauvage, L. R., K. E. Berger, P. B. Mansfield, S. J. Wood, J. C. Smith and J. B. Overton (1974). "Future directions in the development of arterial prostheses for small and medium caliber arteries." The Surgical clinics of North America **54**(1): 213-28.

Schmitz, H. J., R. Erbel, J. Meyer and R. von Essen (1996). "Influence of vessel dilatation on restenosis after successful percutaneous transluminal coronary angioplasty." American Heart Journal **131**(5): 884-891.

Shaw, J. A. and S. Kyriakides (1995). "Thermomechanical aspects of NiTi." Journal of the Mechanics and Physics of Solids **43**: 1243-1281.

Siegenthaler, M. P., E. Weigang, K. Brehm, W. Euringer, T. Baumann, M. Uhl, S. Raghu and F. Beyersdorf (2008). "Endovascular treatment for thoracoabdominal aneurysms: outcomes and results." European Journal of Cardio-Thoracic Surgery **34**(4): 810-819.

Stylianopoulos, T., C. A. Bashur, A. S. Goldstein, S. A. Guelcher and V. H. Barocas (2008). "Computational predictions of the tensile properties of electrospun fibre meshes: Effect of fibre diameter and fibre orientation." Journal of the Mechanical Behavior of Biomedical Materials **1**(4): 326-335.

Sun, Q., D. Wan, J. Liu, Y. Liu, M. Zhu, H. Hong, Y. Sun and Q. Wang (2009). "Influence of antegrade pulmonary blood flow on the hemodynamic performance of bidirectional cavopulmonary anastomosis: A numerical study." Medical Engineering & Physics **31**(2): 227-233.

Sun, W. and P. Lal (2002). "Recent development on computer aided tissue engineering -- a review." Computer Methods and Programs in Biomedicine **67**(2): 85-103.

Tai, N. R., H. J. Salacinski, A. Edwards, G. Hamilton and A. M. Seifalian (2000). "Compliance properties of conduits used in vascular reconstruction." Br J Surg **87**(11): 1516-24.

Tanabe, T., Y. Kubo, M. Hashimoto, T. Takahashi, K. Yasuda and S. Sugie (1980). "Wall reinforcement with highly porous Dacron mesh in aortic surgery." Ann Surg **191**(4): 452-5.

Taylor, C. A., T. J. R. Hughes and C. K. Zarins (1998). "Finite element modeling of blood flow in arteries." Computer Methods in Applied Mechanics and Engineering **158**(1-2): 155-196.

Taylor, C. A., T. J. R. Hughes and C. K. Zarins (1998). "Finite Element Modeling of Three-Dimensional Pulsatile Flow in the Abdominal Aorta: Relevance to Atherosclerosis." Annals of Biomedical Engineering **26**(6): 975-987.

Thiriet, M. (2007). Biology and Mechanics of Blood Flows. Part I: Biology. New York, Springer.

Tiwari, A., K. S. Cheng, H. Salacinski, G. Hamilton and A. M. Seifalian (2003). "Improving the patency of vascular bypass grafts: the role of suture materials and surgical techniques on reducing anastomotic compliance mismatch." Eur J Vasc Endovasc Surg **25**(4): 287-95.

Treloar, L. R. G. (1958). The Physics of Rubber Elasticity. Oxford, Clarendon Press.

Uchida, N., H. Kambic, H. Emoto, J. F. Chen, S. Hsu, S. Murabayshi, H. Harasaki and Y. Nose (1993). "Compliance effects on small diameter polyurethane graft patency." J Biomed Mater Res **27**(10): 1269-79.

Usyk, T. P. and A. D. McCulloch (2003). Computational methods for soft tissue biomechanics. Biomechanics of Soft Tissue in Cardiovascular Systems. G. A. Holzapfel and R. W. Ogden. Wien, Springer**:** 273-342.

Vacanti, J. P. and R. Langer (1999). "Tissue engineering: the design and fabrication of living replacement devices for surgical reconstruction and transplantation." Lancet **354**(9176): SI 32.

Valencia, A. and F. Solis (2006). "Blood flow dynamics and arterial wall interaction in a saccular aneurysm model of the basilar artery." Computers & Structures **84**(21): 1326-1337.

van der Merwe, H. (2007). Development of a Numerical Tool for the Optimisation of Vascular Prosthesis towards Physiological Compliance. Cardiovascular Research Unit. Cape Town, University of Cape Town. **Master:** 146.

van der Merwe, H., B. Daya Reddy, P. Zilla, D. Bezuidenhout and T. Franz (2008). "A computational study of knitted Nitinol meshes for their prospective use as external vein reinforcement." Journal of Biomechanics **41**(6): 1302-1309.

Voorhees, A. B., Jr., A. Jaretzki, 3rd and A. H. Blakemore (1952). "The use of tubes constructed from vinyon "N" cloth in bridging arterial defects." Annals Of Surgery **135**(3): 332-336.

Walke, W., Z. Paszenda and J. Filipiak (2005). "Experimental and numerical biomechanical analysis of vascular stent." Journal of Materials Processing Technology **164-165**: 1263-1268.

Wang, W.-Q., D.-K. Liang, D.-Z. Yang and M. Qi (2006). "Analysis of the transient expansion behavior and design optimization of coronary stents by finite element method." Journal of Biomechanics **39**(1): 21-32.

Wayne, J. S. (2004). Finite Element Analysis. Encyclopedia of Biomaterials and Biomedical Engineering. G. E. Wnek and G. L. Bowlin, Dekker**:** 621-629.

Welch, T., R. Eberhart and C.-J. Chuong (2008). "Characterizing the Expansive Deformation of a Bioresorbable Polymer Fiber Stent." Annals of Biomedical Engineering **36**(5): 742-751.

Wesolowski, S. (1978). Foundations of modern vascular grafts. Vascular Grafts. P. Sawyer and M. Kaplitt. New York, Appleton Century Croft.

Whitcher, F. D. (1997). "Simulation of in vivo loading conditions of nitinol vascular stent structures." Computers & Structures **64**(5-6): 1005-1011.

White, R. A. (1989). Atherosclerosis and arteriosclerosis: human pathology and experimental animal methods and models, CRC Press.

Xu, W., F. Zhou, C. Ouyang, W. Ye, M. Yao and B. Xu (2010). "Mechanical properties of small-diameter polyurethane vascular grafts reinforced by weft-knitted tubular fabric." Journal of Biomedical Materials Research Part A **92A**(1): 1-8.

Yeoman, M. S. (2004). The design and optimisation of fabric reinforced porous prosthetic grafts using finite element methods and genetic algorithms. Cardiovascular Research Unit. Cape Town, University of Cape Town**:** 258.

Yeoman, M. S. (2004). The design and optimisation of fabric reinforced porous prosthetic grafts using finite element methods and genetic algorithms. Cardiovascular Research Unit. Cape Town, University of Cape Town. **PhD:** 258.

Yeoman, M. S., B. D. Reddy, H. Bowles, P. Zilla, D. Bezuidenhout and T. Franz (2009). "The Use of Finite Element Methods and Genetic Algorithms in Search of an Optimal Fabric Reinforced Porous Graft System." Annals of Biomedical Engineering **37**(11): 2266-2287.

Yeoman, M. S., B. D. Reddy, H. C. Bowles, P. Zilla, D. Bezuidenhout and T. Franz (2009). "The use of finite element methods and genetic algorithms in search of an optimal fabric reinforced porous graft system." Ann Biomed Eng **37**(11): 2266-87.

Zidi, M. and M. Cheref (2003). "Mechanical analysis of a prototype of small diameter vascular prosthesis: numerical simulations." Computers in Biology and Medicine **33**(1): 65-75.

Zilla, P., D. Bezuidenhout and P. Human (2007). "Prosthetic vascular grafts: Wrong models, wrong questions and no healing." Biomaterials **28**(34): 5009-5027.

Zilla, P., P. Human, M. Wolf, W. Lichtenberg, N. Rafiee, D. Bezuidenhout, N. Samodien, C. Schmidt and T. Franz (2008). "Constrictive external nitinol meshes inhibit vein graft intimal hyperplasia in nonhuman primates." The Journal of Thoracic and Cardiovascular Surgery **136**(3): 717-725.

Zilla, P., M. Wolf, N. Rafiee, L. Moodley, D. Bezuidenhout, M. Black, P. Human and T. Franz (2009). "Utilization of shape memory in external vein-graft meshes allows extreme diameter constriction for suppressing intimal hyperplasia: A non-human primate study." Journal of vascular surgery. **49**(6): 1532.

Zilla, P. P. and H. P. Greisler (1999). Tissue engineering of vascular prosthetic grafts. Austin, Texas, R.G. Landes Company.

A. Appendix A: Displacement-Based Results

A.1. Standard Models

Table A-1: Displacement-based results of the standard models.

Parameters		Units	BG2.8		NIEM		PUEM		BG2.4		NIEX		PUEX	
			Internal Surface	External Surface	Internal Surface	External Surface	Internal Surface	External Surface	Internal Surface	External Surface	Internal Surface	External Surface	Internal Surface	External Surface
Initial Radius		mm	1.4195	1.7195	1.4195	1.7195	1.4195	1.7195	1.2	1.5	1.2	1.5	1.2	1.5
80 mmHg (Diastol)														
Displacement	Graft	mm	0.575069	0.5614637	0.014208	0.007684	0.08502	0.07688	0.389838	0.37766	0.049103	0.037518	0.183409	0.169696
	Wire mesh											0.00361		0.128873
Radius	Graft	mm	1.994569	2.2809637	1.433708	1.727184	1.50452	1.79638	1.589838	1.87766	1.249103	1.537518	1.383409	1.669696
	Wire mesh											1.50361		1.628873
Wall Compression	max	%	4.54		3.65		3.95		4.06		13.90		14.92	
	min	%	4.53		0.03		0.97		4.06		-0.93		3.01	
Max Sress	Graft	MPa	0.08087		0.01222		0.03727		0.06552		0.0201		0.03644	
	Wire mesh	MPa			57.59		16.76				73.68		18.98	
Max Strain	Graft	%	33.41%		5.72%		16.15%		27.53%		8.94%		15.63%	
	Wire mesh	%			0.09%		2.94%				0.20%		3.33%	
Martensite Fraction (NITI wire mesh)		%			0						0			
120 mmHg (Systol)														
Displacement	Graft	mm	1.42404	1.3941812	0.021337	0.011424	0.122985	0.110457	0.803509	0.78014	0.084178	0.062601	0.269584	0.246245
	Wire mesh											0.005688		0.185379
Radius	Graft	mm	2.84354	3.1136812	1.440837	1.730924	1.542485	1.829957	2.003509	2.28014	1.284178	1.562601	1.469584	1.746245
	Wire mesh											1.505688		1.685379
Wall Compression	max	%	9.96		5.60		6.07		7.79		24.21		23.44	
	min	%	9.95		0.13		1.46		7.79		3.15		4.81	
Max Sress	Graft	MPa	0.1864		0.01887		0.05455		0.1317		0.03066		0.05486	
	Wire mesh	MPa			86.72		24.67				97		28.08	
Max Strain	Graft	%	68.47%		7.46%		22.40%		50.28%		12.77%		21.87%	
	Wire mesh	%			0.14%		4.33%				0.27%		4.93%	
Martensite Fraction (NITI wire mesh)		%			0						0			
200 mmHg														
Displacement		mm			0.035916	0.018805	0.194571	0.172375			0.137318	0.096471	0.412691	0.366379
Radius		mm			1.455416	1.738305	1.614071	1.891875			1.337318	1.596471	1.612691	1.866379
Wall Compression	max	%			9.86		11.00				37.24		36.32	
	min	%			0.50		2.46				6.12		8.74	
Max Sress	Graft	MPa			0.03409		0.09105				0.04647		0.09267	
	Wire mesh	MPa			145.6		39.45				157.9		45.12	
Max Strain	Graft	%			13.83%		32.54%				17.25%		31.17%	
	Wire mesh	%			0.24%		6.92%				0.43%		7.92%	
Martensite Fraction (NITI wire mesh)		%			0						0			
Compliance	Graft	%/100mmHg	106.41	91.27	1.24	0.54	6.31	4.67	65.05	53.59	7.02	4.08	15.57	11.46

A.2. Mesh Refinement Models

Table A-2: Displacement-based results of the mesh refinement models.

Parameters		Units	NIEX-coarse		NIEX		NIEX-fine		PUEX-coarse		PUEX		PUEX-fine	
			Internal Surface	External Surface	Internal Surface	External Surface	Internal Surface	External Surface	Internal Surface	External Surface	Internal Surface	External Surface	Internal Surface	External Surface
Initial Radius		mm	1.2	1.5	1.2	1.5	1.2	1.5	1.2	1.5	1.2	1.5	1.2	1.5
80 mmHg (Diastol)														
Displacement	Graft	mm	0.043722	0.0332171	0.049103	0.037518	0.049976	0.038162	0.170727	0.157095	0.183409	0.169696	0.170802	0.157068
	Wire mesh			0.0043363		0.00361		0.003914		0.116238		0.128873		0.11506
Radius	Graft	mm	1.243722	1.5332171	1.249103	1.537518	1.249976	1.538162	1.370727	1.657095	1.383409	1.669696	1.370802	1.657068
	Wire mesh			1.5043363		1.50361		1.503914		1.616238		1.628873		1.61506
Wall Compression	max	%	10.71		13.90		14.52		14.33		14.92		15.22	
	min	%	-1.23		-0.93		-0.58		2.81		3.01		2.85	
Max Sress	Graft	MPa	0.01823		0.0201		0.02022		0.0319		0.03644		0.03484	
	Wire mesh	MPa	70.08		73.68		77.75		21.66		18.98		19	
Max Strain	Graft	%	8.68%		8.94%		8.99%		14.02%		15.63%		14.95%	
	Wire mesh	%	0.19%		0.20%		0.21%		3.80%		3.33%		3.33%	
Martensite Fraction (NITI wire mesh)		%	0		0		0							
120 mmHg (Systol)														
Displacement	Graft	mm	0.080096	0.0594862	0.084178	0.062601	0.084554	0.062818	0.248028	0.225358	0.269584	0.246245	0.257751	0.234364
	Wire mesh			0.0108952		0.005688		0.008905		0.167416		0.185379		0.170639
Radius	Graft	mm	1.280096	1.5594862	1.284178	1.562601	1.284554	1.562818	1.448028	1.725358	1.469584	1.746245	1.457751	1.734364
	Wire mesh			1.5108952		1.505688		1.508905		1.667416		1.685379		1.670639
Wall Compression	max	%	22.12		24.21		24.26		22.77		23.44		23.79	
	min	%	2.80		3.15		3.20		4.57		4.81		4.75	
Max Sress	Graft	MPa	0.02762		0.03066		0.03051		0.04762		0.05486		0.05333	
	Wire mesh	MPa	94.3		97		96.69		30.86		28.08		28.47	
Max Strain	Graft	%	13.10%		12.77%		12.71%		19.29%		21.87%		21.29%	
	Wire mesh	%	0.26%		0.27%		0.26%		5.41%		4.93%		5.00%	
Martensite Fraction (NITI wire mesh)		%	0		0		0							
200 mmHg														
Displacement		mm	0.134546	0.0941437	0.137318	0.096471			0.392305	0.346855	0.412691	0.366379		
Radius		mm	1.334546	1.5941437	1.337318	1.596471			1.592305	1.846855	1.612691	1.866379		
Wall Compression	max	%	38.41		37.24				38.96		36.32			
	min	%	5.58		6.12				8.54		8.74			
Max Sress	Graft	MPa	0.04866		0.04647				0.0872		0.09267			
	Wire mesh	MPa	162.3		157.9				50.78		45.12			
Max Strain	Graft	%	19.63%		17.25%				29.17%		31.17%			
	Wire mesh	%	0.44%		0.43%				8.91%		7.92%			
Martensite Fraction (NITI wire mesh)		%	0		0									
Compliance	Graft	%/100mmHg	7.31	4.28	7.02	4.08	6.92	4.01	14.10	10.30	15.57	11.46	15.86	11.66

A.3. Boundary Condition Verification

Table A-3: Displacement-based results of the boundary conditions verification models.

Parameters		Units	NIEX (points approach)		NIEX-BCV	
			Internal Surface	External Surface	Internal Surface	External Surface
Initial Radius		**mm**	**1.2**	**1.5**	**1.2**	**1.5**
80 mmHg (Diastol)						
Displacement	**Graft**	**mm**	0.051847	0.0409074	0.05114	0.039916
	Wire mesh			/		/
Radius	**Graft**	**mm**	1.251847	1.5409074	1.25114	1.539916
	Wire mesh			1.5		1.5
Wall Compression	**max**	**%**	/		/	
	min	**%**	/		/	
Max Sress	**Graft**	**MPa**	0.0201		0.01949	
	Wire mesh	**MPa**	73.68		74.57	
Max Strain	**Graft**	**%**	8.94%		8.64%	
	Wire mesh	**%**	0.20%		0.20%	
Martensite Fraction (NITI wire mesh)		**%**	0		0	
120 mmHg (Systol)						
Displacement	**Graft**	**mm**	0.086779	0.0632395	0.085733	0.062529
	Wire mesh			/		/
Radius	**Graft**	**mm**	1.286779	1.5632395	1.285733	1.562529
	Wire mesh			1.5		1.5
Wall Compression	**max**	**%**	/		/	
	min	**%**	/		/	
Max Sress	**Graft**	**MPa**	0.03066		0.03023	
	Wire mesh	**MPa**	97		97.52	
Max Strain	**Graft**	**%**	12.77%		12.51%	
	Wire mesh	**%**	0.27%		0.27%	
Martensite Fraction (NITI wire mesh)		**%**	0		0	
Displacement		**mm**	0.140679	0.0952381	0.137825	0.093433
Radius		**mm**	1.340679	1.5952381	1.337825	1.593433
Wall Compression	**max**	**%**	/		/	
	min	**%**	/		/	
Max Sress	**Graft**	**MPa**	0.04647		0.05039	
	Wire mesh	**MPa**	157.9		154	
Max Strain	**Graft**	**%**	17.25%		17.99%	
	Wire mesh	**%**	0.43%		0.42%	
Martensite Fraction (NITI wire mesh)		**%**	0		0	
Compliance	**Graft**	**%/100mmHg**	6.98	3.62	6.91	3.67

A.4. Friction Verification

Table A-4: Displacement-based results of the friction verification models.

Parameters		Units	NIEX-FL		NIEM-FL	
			Internal Surface	External Surface	Internal Surface	External Surface
Initial Radius		**mm**	**1.2**	**1.5**	**1.4195**	**1.7195**
80 mmHg (Diastol)						
Displacement	**Graft**	**mm**	0.058277	0.0452218	0.014208	0.007684
	Wire mesh			0.0011138		
Radius	**Graft**	**mm**	1.258277	1.5452218	1.433708	1.727184
	Wire mesh			1.5011138		
Wall Compression	**max**	**%**	17.43		3.65	
	min	**%**	1.52		0.03	
Max Sress	**Graft**	**MPa**	0.02307		0.01222	
	Wire mesh	**MPa**	72.65		57.61	
Max Strain	**Graft**	**%**	10.13%		5.72%	
	Wire mesh	**%**	0.20%		0.09%	
Martensite Fraction (NITI wire mesh)		**%**	0		0	
120 mmHg (Systol)						
Displacement	**Graft**	**mm**	0.094177	0.0716333	0.021337	0.011424
	Wire mesh			0.0061921		
Radius	**Graft**	**mm**	1.294177	1.5716333	1.440837	1.730924
	Wire mesh			1.5061921		
Wall Compression	**max**	**%**	25.78		5.60	
	min	**%**	2.91		0.13	
Max Sress	**Graft**	**MPa**	0.03395		0.01887	
	Wire mesh	**MPa**	105.6		86.77	
Max Strain	**Graft**	**%**	13.97%		8.46%	
	Wire mesh	**%**	0.29%		0.14%	
Martensite Fraction (NITI wire mesh)		**%**	0		0	
			186.3 mmHg		**200 mmHg**	
Displacement		**mm**	0.140313	0.1024238	0.035917	0.018806
Radius		**mm**	1.340313	1.6024238	1.455417	1.738306
Wall Compression	**max**	**%**	37.86		9.86	
	min	**%**	5.29		0.50	
Max Sress	**Graft**	**MPa**	0.04759		0.03409	
	Wire mesh	**MPa**	174.1		145.7	
Max Strain	**Graft**	**%**	18.00%		13.83%	
	Wire mesh	**%**	0.47%		0.24%	
Martensite Fraction (NITI wire mesh)		**%**	0		0	
Compliance	**Graft**	**%/100mmHg**	7.13	4.27	1.24	0.54